



NASA Orbital Debris Engineering Model (ORDEM) 3.1

Model Process

Orbital Debris Program Office

*Alyssa Manis
HX5 – Jacobs JETS Contract*

*Mark Matney
NASA Johnson Space Center*

*Andrew Vavrin
GeoControl Systems – Jacobs JETS Contract*

*John Seago
ERC – Jacobs JETS Contract*

*Drake Gates
Jacobs – Jacobs JETS Contract*

*Phillip Anz-Meador
Jacobs – Jacobs JETS Contract*

*Timothy Kennedy
NASA Johnson Space Center*

*Heather Cowardin
NASA Johnson Space Center*

*Yu-lin Xu
University of Texas at El Paso – Jacobs JETS Contract*

NASA STI Program Report Series

The NASA STI Program collects, organizes, provides for archiving, and disseminates NASA's STI. The NASA STI program provides access to the NTRS Registered and its public interface, the NASA Technical Reports Server, thus providing one of the largest collections of aeronautical and space science STI in the world. Results are published in both non-NASA channels and by NASA in the NASA STI Report Series, which includes the following report types:

- **TECHNICAL PUBLICATION.** Reports of completed research or a major significant phase of research that present the results of NASA Programs and include extensive data or theoretical analysis. Includes compilations of significant scientific and technical data and information deemed to be of continuing reference value. NASA counterpart of peer-reviewed formal professional papers but has less stringent limitations on manuscript length and extent of graphic presentations.
- **TECHNICAL MEMORANDUM.** Scientific and technical findings that are preliminary or of specialized interest, e.g., quick release reports, working papers, and bibliographies that contain minimal annotation. Does not contain extensive analysis.
- **CONTRACTOR REPORT.** Scientific and technical findings by NASA-sponsored contractors and grantees.
- **CONFERENCE PUBLICATION.** Collected papers from scientific and technical conferences, symposia, seminars, or other meetings sponsored or co-sponsored by NASA.
- **SPECIAL PUBLICATION.** Scientific, technical, or historical information from NASA programs, projects, and missions, often concerned with subjects having substantial public interest.
- **TECHNICAL TRANSLATION.** English-language translations of foreign scientific and technical material pertinent to NASA's mission.

Specialized services also include organizing and publishing research results, distributing specialized research announcements and feeds, providing information desk and personal search support, and enabling data exchange services.

For more information about the NASA STI program, see the following:

- Access the NASA STI program home page at <http://www.sti.nasa.gov>
- Help desk contact information:
<https://www.sti.nasa.gov/sti-contact-form/>
and select the "General" help request type.



NASA Orbital Debris Engineering Model (ORDEM) 3.1 Model Process

Orbital Debris Program Office

*Alyssa Manis
HX5 – Jacobs JETS Contract*

*Mark Matney
NASA Johnson Space Center*

*Andrew Vavrin
GeoControl Systems – Jacobs JETS Contract*

*John Seago
ERC – Jacobs JETS Contract*

*Drake Gates
Jacobs – Jacobs JETS Contract*

*Phillip Anz-Meador
Jacobs – Jacobs JETS Contract*

*Timothy Kennedy
NASA Johnson Space Center*

*Heather Cowardin
NASA Johnson Space Center*

*Yu-lin Xu
University of Texas at El Paso – Jacobs JETS Contract*

National Aeronautics and Space Administration

Lyndon B. Johnson Space Center
Houston, Texas 77058

March 2022

ACKNOWLEDGEMENTS

The authors would like to thank Ms. Debra Shoots for her technical editing of this document and her expertise and guidance on NASA STI standards. Additionally, the authors would like to thank the entire team in the NASA Orbital Debris Program Office that contributed to processing, analysis, and quality control of the radar, optical, and *in situ* data that was used to build the model populations as described in this document. Finally, the authors would like to thank all persons and organizations that contributed to collecting and providing the data to the NASA Orbital Debris Program Office.

Available from:

NASA STI Program
Mail Stop 148
NASA Langley Research Center
Hampton, VA 23681-2199

National Technical Information Service
5285 Port Royal Road
Springfield, VA 22161

This report is also available in electronic form at <http://www.sti.nasa.gov/> and <http://ntrs.nasa.gov>

REVISION AND HISTORY PAGE

REV.	DESCRIPTION	PUB. DATE
1.0	Initial Release	March 2022

This Page Intentionally Left Blank

TABLE OF CONTENTS

1.0	Introduction	1
1.1	Purpose and Scope	1
1.2	ORDEM 3.1 – An Engineering Model	1
1.2.1	Requirements for an Engineering Model	1
1.2.2	Limitations of an Engineering Model	1
1.2.3	Historical Overview	2
1.3	ORDEM 3.1 Program Philosophy	3
1.3.1	Orbit Spatial Densities	3
1.3.2	Orbit Distributions	4
1.3.3	GEO Populations	11
1.3.4	Igloo Elements	15
1.3.5	Debris Sizes	16
1.3.6	Material Densities	17
2.0	Supporting Models: LEGEND	17
3.0	Data Analysis and population builds	18
3.1	Radar-Based Populations	20
3.1.1	Reference Population	20
3.1.2	Supporting Data	22
3.1.3	HUSIR Data Cleaning and Analysis	22
3.1.4	Scaling LEGEND Model Populations	26
3.1.4.1	Special Populations in LEO	26
3.1.4.1.1	Custom Breakups	26
3.1.4.1.2	Major Collisions: FY-1C, Iridium 33, and Cosmos 2251	29
3.1.4.1.3	SNAPSHOT/Transit	34
3.1.4.1.4	NaK	35
3.1.4.2	Bayesian Approach Applied to ORDEM Populations	38
3.1.4.3	Final Scaling of Radar-Based Populations	40
3.2	<i>In situ</i> -Based Populations	41
3.2.1	Reference Population	43
3.2.2	Supporting Data	44
3.2.2.1	STS Window Craters	44
3.2.2.2	STS Radiator Perforations	46
3.2.3	MARK files	48
3.2.4	Feature to Impactor Sizes	49
3.2.5	Fitting Procedure	51
3.3	Optical-Based Populations	57
3.3.1	Reference Population	57
3.3.2	Supporting Data	58
3.3.3	Fragmentation Debris Identification	63
3.3.4	Assigning Orbital Elements	65
3.3.5	Extending Population to 10 cm	68
4.0	Calculation of flux uncertainties	70
4.1	Errors and Propagation of Uncertainties	71
4.1.1	Composite Fluxes	73
4.1.2	Uncertainty, Proportionality Constant	75
4.2	Radar-Scaled LEGEND Population	76
4.3	Degradation Population	77
4.4	GEO Population	77
4.5	Upper and Lower Sigma Bounds for Flux vs. Size	79

5.0	ORDEM Interpolation approach	79
5.1	Background	79
5.2	Scope of the ORDEM 3.1 Interpolation	82
5.3	ORDEM Interpolation General Conditions	83
5.4	PCHIP Implementation in ORDEM 3.1	83
5.5	PCHIP Implementation Verification	87
6.0	References	88
A	PCHIP Implementation Verification Test Cases	92

FIGURES

Figure 1-1. A 2010 catalog distribution of non-GEO orbiting objects in inclination and perigee altitude, with the tick marks showing the ORDEM binning resolution. For clarity, only the perigee altitudes corresponding to the bins 1–57 (100–2000 km with 33.33 km bin spacing) are shown in this figure.....	5
Figure 1-2. A 2010 catalog distribution of non-GEO orbiting objects in inclination and perigee altitude, with the tick marks showing the ORDEM binning resolution. For clarity, only the perigee altitudes corresponding to the bins 58–137 (2000–10000 km with 100 km bin spacing) are shown in this figure.....	6
Figure 1-3. A 2010 catalog distribution of non-GEO orbiting objects in inclination and perigee altitude, with the tick marks showing the ORDEM binning resolution. For clarity, only the perigee altitudes corresponding to the bins 138–287 (10000–40000 km with 200 km bin spacing) are shown in this figure.....	7
Figure 1-4. A 2010 catalog distribution of non-GEO orbiting objects in inclination and square root of eccentricity, with the tick marks showing the ORDEM binning resolution. Note that objects in ORDEM are binned according to their eccentricity, but the y-axis here is $\text{Sqrt}(\text{eccentricity})$ to show how the eccentricity bins are uniform in $\text{Sqrt}(\text{eccentricity})$ space.....	8
Figure 1-5. A 2010 catalog distribution of non-GEO orbiting objects in perigee altitude and square root of eccentricity, with the tick marks showing the ORDEM binning resolution. Note that objects in ORDEM are binned according to eccentricity, but the x-axis here is $\text{Sqrt}(\text{eccentricity})$ to show how the eccentricity bins are uniform in $\text{Sqrt}(\text{eccentricity})$ space. For clarity, only the perigee altitudes corresponding to the bins 1–57 (100–2000 km with 33.33 km bin spacing) are shown in this figure.....	9
Figure 1-6. A 2010 catalog distribution of non-GEO orbiting objects in perigee altitude and square root of eccentricity, with the tick marks showing the ORDEM binning resolution. Note that objects in ORDEM are binned according to eccentricity, but the x-axis here is $\text{Sqrt}(\text{eccentricity})$ to show how the eccentricity bins are uniform in $\text{Sqrt}(\text{eccentricity})$ space. For clarity, only the perigee altitudes corresponding to the bins 58–137 (2000–10000 km with 100 km bin spacing) are shown in this figure.....	10
Figure 1-7. A 2010 catalog distribution of non-GEO orbiting objects in perigee altitude and square root of eccentricity, with the tick marks showing the ORDEM binning resolution. Note that objects in ORDEM are binned according to eccentricity, but the x-axis here is $\text{Sqrt}(\text{eccentricity})$ to show how the eccentricity bins are uniform in $\text{Sqrt}(\text{eccentricity})$ space. For clarity, only the perigee altitudes corresponding to the bins 138–287 (10000–40000 km with 200 km bin spacing) are shown in this figure.....	11
Figure 1-8. A 2010 catalog distribution of GEO objects in mean motion and square root of eccentricity, with the tick marks showing the ORDEM binning resolution. The figure inset shows a zoomed-in region of GEO objects with a mean motion between 0.95 to 1.05 revs/day, which are binned with 0.001 revs/day-bin spacing. Note that objects in ORDEM are binned according to their eccentricity, but the y-axis here is $\text{Sqrt}(\text{eccentricity})$ to show how the eccentricity bins are uniform in $\text{Sqrt}(\text{eccentricity})$ space.....	12
Figure 1-9. A 2010 catalog distribution of GEO objects in inclination and square root of eccentricity, with the tick marks showing the ORDEM binning resolution. The figure inset shows a zoomed-in region of GEO objects with inclination less than 1°; GEO objects in ORDEM with an inclination between 0.0° to 0.2° are stored in bin 1, and objects with an inclination between 0.2° and 1.0° are stored in bin 2.....	13
Figure 1-10. A 2010 catalog distribution of GEO objects in mean motion and inclination. The x-axis shows mean motion with tick mark spacing of 0.01 revs/day for clarity; however, GEO objects in ORDEM with a mean motion between 0.95 to 1.05 revs/day are binned with 0.001 revs/day-bin spacing (see Figure 1-8). The y-axis (inclination) shows inclination with gridline spacing of 1° for clarity; however, GEO objects in ORDEM with an inclination between 0.0° to 0.2° are stored in bin 1, and objects with an inclination between 0.2° and 1.0° are stored in bin 2 (see Figure 1-9).	14

Figure 1-11. A 2010 catalog distribution of GEO objects in mean motion and right ascension of the ascending node. The x-axis shows mean motion with tick mark spacing of 0.01 revs/day for clarity; however, GEO objects in ORDEM with a mean motion between 0.95 to 1.05 revs/day are binned with 0.001 revs/day-bin spacing (see Figure 1-8).	15
Figure 1-12. Conceptual relation between one igloo element (elevation, azimuth, relative velocity) and its orbit distribution (perigee, eccentricity)	16
Figure 1-13. Illustration of body and projected measurement on complex shape (Hill, 2008).	17
Figure 3-1. Measurement coverage for small debris from sources available for NASA models.	19
Figure 3-2. Relative density percentages for spacecraft plastic, aluminum, and steel fragments derived from the SOCIT4 data, as a function of debris size.....	21
Figure 3-3. SOCIT4 MD and HD relative number percentages as a function of debris size. MD here includes aluminum, and HD includes steel and copper.....	21
Figure 3-4. Radar data cleaning and analysis process – starting with data collected by the radars at MIT/LL through the delivery of final detection lists summarizing yearly OD observations.	23
Figure 3-5. Range-Doppler Image for an OD detection (left) and a more obvious example of RFI (right).....	23
Figure 3-6. Identification of spurious Doppler, or range-rate, as a function of day of year. Large spreads in Doppler and increased detection rates over short time windows are another indication of RFI.	24
Figure 3-7. Comparison between NaK data collected on DOY 150–160 of FY17, representing a nominal NaK count distribution, and that collected over DOY 250–260, representing a data collection containing additional uncorrected bias. A vertical line at -35 dBsm, the distribution peak for HUSIR, is shown for reference.....	25
Figure 3-8. Altitude vs. inclination plot of the 2013–2015 HUSIR radar data. The data have a natural separation and were subsequently broken into five inclination bands. The modeled LEGEND population was then compared to the radar data by inclination band and individual breakup events in each band were adjusted to better match the available radar data.	27
Figure 3-9. The detection rate of > 1 cm objects in the 68°–80° inclination band for the HUSIR data and the three breakups in this inclination band after custom scale factors were applied. This inclination band also includes the Cosmos 2251 debris, which dominates the debris population at lower altitudes and is shown for reference.	28
Figure 3-10. Empirical model enhancements to the modeled A/m ratio of fragments as a function of characteristic length for the three major breakup clouds (FY-1C ASAT, Iridium 33, and Cosmos 2251).....	30
Figure 3-11. Comparison of the inclination distribution for the FY-1C ASAT breakup cloud between the SSN catalog (based on the earliest-available TLE for each debris object), the NASA SSBM, and the adjusted breakup model.	31
Figure 3-12. Comparison of the detection rate vs. altitude, to a limiting size of 1 cm, for the FY-1C ASAT breakup cloud between ORDEM 3.0 and ORDEM 3.1, and to the HUSIR 75E 2013–2015 data within the inclination band corresponding to the FY-1C ASAT cloud.....	32
Figure 3-13. Comparison of the detection rate vs. altitude, to a limiting size of 1 cm, for the Iridium 33 breakup cloud between ORDEM 3.0 and ORDEM 3.1, and to the HUSIR 75E 2013–2015 data within the inclination band corresponding to the Iridium 33 cloud.....	33
Figure 3-14. Comparison of the detection rate vs. altitude, to a limiting size of 1 cm, for the Cosmos 2251 breakup cloud between ORDEM 3.0 and ORDEM 3.1, and to the HUSIR 75E 2013–2015 data within the inclination band corresponding to the Cosmos 2251 cloud.	34
Figure 3-15. NaK distribution predicted for 2014 by assuming production only at time of core jettison, compared to the NaK detections from the 2014 HUSIR 75E data.	36
Figure 3-16. The black curve shows the theoretical RCS value for a given conducting sphere diameter (given the HUSIR 3 cm wavelength). The red dashed line is for an RCS of -43 dBsm, corresponding to a sphere 6.42 mm in diameter. For HUSIR detections of objects with RCS values above about -43 dBsm, there is an ambiguity in determining the size of the object for a given RCS. Counting the number of detections with RCS above -43 dBsm gives a good estimate of the total number of spheres larger than 6.42 mm in diameter.	37

Figure 3-17. Comparison of the surface area flux vs. altitude for a limiting size of 1 cm and larger between the initial unscaled ORDEM 3.1 population, final ORDEM 3.1 population after all radar-based scalings were applied, and measurements from the HUSIR 75E 2013–2015 composite dataset.....	41
Figure 3-18. Comparison of the surface area flux vs. altitude for a limiting size of 5.6 mm and larger between the initial unscaled ORDEM 3.1 population, final ORDEM 3.1 population after all radar-based scalings were applied, and measurements from the HUSIR 75E 2013–2015 composite dataset.....	41
Figure 3-19. Example of chipped paint on coated surfaces aboard the ISS. Note the liberation of a significant amount of the coating, revealing the substrate material, between December 1998 (left) and May 2000 (right).	42
Figure 3-20. High-speed imagery of a spherical particle impacting a Whipple shield test article. Clearly visible are the upwards ejecta and downwards spallation clouds, the latter impacting the target plate.....	42
Figure 3-21. Crew module windows location. Note that windows 9 and 10 (aft-facing cargo bay windows) were not used for building ORDEM 3.1 populations.	44
Figure 3-22. Shuttle Impact Database distribution of MM, OD, and unknown impacts on STS windows identified by SEM-EDX analysis. Annotations indicate the absolute number and corresponding percentage of identified constituents out of the total of 1986 identified impacts.....	45
Figure 3-23. Identified OD impactors for STS window craters by material category. The “D” prefix in the legend for each material type refers to the identification of the impactor as debris vs. the other possible classifications of MM or unknown. Annotations indicate absolute number (out of 323 OD) and percentage of that total.....	45
Figure 3-24. Payload bay door radiator diagram.	46
Figure 3-25. Shuttle Impact Database distribution of MM, OD, and unknown impact features on STS radiators identified by SEM-EDX analysis. Annotations indicate the absolute number and corresponding percentage of identified constituents out of the total of 640 identified features.	47
Figure 3-26. Shuttle Impact Database distribution by source (MM, OD, and unknown) for STS radiator perforations. Annotations indicate absolute number (out of 81 total) and percentage of that total.....	47
Figure 3-27. STS radiator OD perforations by material type. The “D” prefix in the legend for each material type refers to the identification of the impactor as debris vs. the other possible classifications of MM or unknown. Note that AI is not present as AI traces cannot be distinguished from the radiator’s AI substrate. Annotations indicate absolute number (out of 39 OD) and percentage of that total.....	48
Figure 3-28. Window and radiator identifiers for Table 3-9. Note that the window identifiers here are not associated to those presented in Figure 3-21, but are identifiers corresponding to the MARK files.	49
Figure 3-29. General process for comparing modeled fluxes on a surface with the distribution of feature sizes on that surface, used to scale the reference ORDEM 3.1 degradation population to match the STS impact record. Double arrows indicate where comparisons between the model and data were made.	51
Figure 3-30. Small particle (\leq ~3 mm) estimation methodology.	52
Figure 3-31. Comparison of cumulative number of radiator perforations vs. facesheet perforation diameter for ORDEM 3.1 predictions and STS HD impact data from low altitude missions. Statistical tests indicate that these data are within the 95% confidence limit of being sampled from this distribution. Note that if the rightmost point did not exist, this fit would be substantially improved (well within 90% confidence limits).	54
Figure 3-32. Comparison of cumulative number of radiator perforations vs. facesheet perforation diameter for ORDEM 3.1 predictions and HD STS impact data from high altitude missions. Statistical tests indicate that these data are within the 95% confidence limit of being sampled from this distribution.....	55
Figure 3-33. Comparison of cumulative number of radiator perforations vs. facesheet perforation diameter for ORDEM 3.1 predictions and HD STS impact data from all missions. Statistical tests	

indicate that these data are well within the 90% confidence limit of being sampled from this distribution.	56
Figure 3-34. Comparison of cumulative number of radiator perforations vs. facesheet perforation diameter for ORDEM 3.1 predictions and MD STS impact data from all missions. Statistical tests indicate that these data are well within the 90% confidence limit of being sampled from this distribution.	57
Figure 3-35. Probability of detection, overlaid with actual detections, in [$\text{INC} \cdot \cos(\text{RAAN})$, $\text{INC} \cdot \sin(\text{RAAN})$] Cartesian space, for the 2004–2006 MODEST observation period. CTs are represented by solid diamonds and UCTs are represented by open diamonds.	60
Figure 3-36. Probability of detection, overlaid with actual detections, in [$\text{INC} \cdot \cos(\text{RAAN})$, $\text{INC} \cdot \sin(\text{RAAN})$] Cartesian space, for the 2007–2009 MODEST observation period. CTs are represented by solid diamonds and UCTs are represented by open diamonds.	61
Figure 3-37. Absolute magnitude distribution of the MODEST 2004–2006 and 2007–2009 datasets. The slope of the NASA SSBM power law for explosions, scaled to the MODEST distributions, is overlaid for reference.	62
Figure 3-38. MODEST 2004–2009 UCTs and CT debris, propagated to the common epoch of 0h UT on 1 January 2007 and projected in [$\text{INC} \cdot \cos(\text{RAAN})$, $\text{INC} \cdot \sin(\text{RAAN})$] Cartesian space, overlaid with the debris ring limits calculated based on the angle between the orbit plane and that of the stable Laplace plane. General regions of fragments associated with the four GEO breakups that occurred prior to the MODEST campaigns are indicated for reference. Objects seen outside the ring were excluded from the model as probable non-GEO objects imitating GEO behavior over the short-time arc of observations.	65
Figure 3-39. Mean motion as a function of the angle between the orbit plane and the stable Laplace plane for the modeled Ekran 2, 4, and 9 and Titan 3C (1968-081E) breakup clouds, propagated to the common epoch of 0h UT on 1 January 2007.	66
Figure 3-40. Eccentricity as a function of mean motion for the modeled Ekran 2, 4, and 9 and Titan 3C (1968-081E) breakup clouds, propagated to the common epoch of 0h UT on 1 January 2007.	67
Figure 3-41. Eccentricity as a function of mean motion from 100 generic modeled breakups in GEO with an initial mean motion of 0.99 rev/day.	68
Figure 3-42. Binned differential size distribution for the UCTs and CT debris from the 2004–2009 composite MODEST dataset, propagated to the common epoch of 0h UT on 1 January 2007 and limited from 30 cm to 1.25 m in size. The distribution from the power law curve fit is shown extended down to 10 cm.	69
Figure 4-1. Example of correlated fluxes across yaw and velocity bins from a particular orbit family. The same orbit family of debris contributes to flux from different directions and velocities.	70
Figure 4-2. Uncertainties for the ORDEM 3.1 GEO populations based on variations in instrumental magnitude and assumed albedo for converting magnitude to size. The total population uncertainty assumed for the GEO populations is given by the dashed black curves.	78
Figure 5-1. PCHIP implementation for a challenging, simulated LD data set, indicated by 11 half-decadal reference points in $\log_{10}(\text{size})$ space. Five hundred interpolated points provide a smoothly interpolated curve over this data set.	81
Figure 5-2. PCHIP interpolation of ORDEM subpopulations, with critical diameters required to penetrate an aluminum Whipple bumper indicated. Interpolation is required to assess the subpopulation flux at the computed critical diameters. Critical diameters vary according to mass density of the debris projectile. The intact population, used to represent the satellite catalog, terminates at 10 cm while the LD population (as in Figure 5-1) terminates at 1 mm. See text for specifics of the target orbit for this example.	82
Figure 5-3. An example of interpolation with (ORDEM 3.0) and without (ORDEM 3.1) the steering function imposed on the last significant half-decade in size for the HD component of a typical ISS orbit in 2015.	84
Figure 5-4. An example ORDEM 3.1 interpolation of the fluxes from the five density families for a typical ISS orbit in 2020 (the NaK family omitted due to zero flux at ISS altitudes).	85
Figure 5-5. Interpolator package flow chart.	86

TABLES

Table 1-1 Feature comparison of ORDEM2000, ORDEM 3.0, and ORDEM 3.1	3
Table 1-2. Non-GEO population binning in ORDEM.	4
Table 1-3. GEO population binning in ORDEM.	12
Table 3-1. Data sources used for building the ORDEM 3.1 populations, with applicable size limits and years of coverage. Years covered by comparable datasets used for building ORDEM 3.0 populations are also shown for comparison.	19
Table 3-2. LEO Special Debris Populations.....	26
Table 3-3. Ten breakups selected by inclination band that received a custom scaling factor.....	27
Table 3-4. Overall number and delta-velocity scalings for the three major breakup clouds (ASAT, Iridium 33, and Cosmos 2251).	29
Table 3-5. Anomalous event dates for the SNAPSHOT and Transit satellites.....	34
Table 3-6. Model ratio of the NaK population at the ORDEM fiducial sizes to the empirical size distribution at 6.42 mm, as scaled to the total number of objects counted with size 6.42 mm.	38
Table 3-7. Weighted-average model parameters estimated in the initial iteration of the Bayesian scheme from HUSIR 75E data of CY2013–15 for the special SNAPSHOT and Transit clouds.	39
Table 3-8. Final scale factors applied to radar-based populations in ORDEM 3.1	40
Table 3-9. Numerical designation, description, and surface area for each radiator and window. Identifiers correspond to the surfaces shown in Figure 3-28. Crew module window numbers listed correspond to those shown in Figure 3-21.	49
Table 3-10. Confirmed breakup events in GEO as of the time of ORDEM 3.1 development.....	58
Table 3-11. Completeness in circular mean motion and composite weights calculated for the 2004–2006 and 2007–2009 MODEST datasets.	63
Table 3-12. Curve fits for mean motion (<i>MM</i>) as a function of orbit angle (β) for the modeled Ekran 2, 4, and 9 and Titan 3C (1968-081E) breakup clouds.	66
Table 3-13. Curve fits for eccentricity (<i>ECC</i>) as a function of mean motion (<i>MM</i>) for the modeled Ekran 2, 4, and 9 and Titan 3C (1968-081E) breakup clouds.	67
Table 3-14. Curve fits for eccentricity (<i>ECC</i>) as a function of mean motion (<i>MM</i>) from 100 generic modeled GEO breakups with an initial mean motion of 0.99 rev/day.	68
Table 5-1. Differentiating features of the PCHIP interpolation routine in ORDEM 3.1 as compared to ORDEM 3.0	83
Table 5-2. ORDEM 3.1 PCHIP interpolation test case examples. Herein, “element” refers to the IGLOOFLUX_SC.OUT file’s element number (corresponding to a specific azimuth-elevation-relative velocity bin) while “density family” refers to the specific ensemble of 11 flux values chosen for the test for the densities LD, MD, HD, and IN (Intact/cataloged objects > 10 cm size).	87
Table 5-3. The interpolated flux for all density families, element 3706. The NK (NaK) family has been omitted since there was no flux at the ISS altitude. Both the LD and IN flux are constant within this decade (and for this case, with a non-zero modeled LD flux). Bold text indicates the three reference points in this decade: the decade boundaries and the half-decade point.....	88

Table A-1. The interpolated flux for element 3706. For this test case, the complete set of interpolated fluxes, 101 points covering sizes from 10 μm to 1 m, are shown for each density family (LD, MD, HD, and IN) to provide a complete reference test case. Note that the NK (NaK) density family is not shown since there is no flux at the ISS altitude. Bold text indicates the 11 reference points in this size range.....	92
Table A-2. The interpolated flux for element 6871. For this test case, a subset of interpolated fluxes is shown, covering sizes from 316 μm to 3.16 cm for the LD family. Bold text indicates the five reference points in this size range.....	94
Table A-3. The interpolated flux for element 6481. For this test case, a subset of interpolated fluxes is shown, covering sizes from 10 μm to 316 μm for the HD family. Bold text indicates the four reference points in this size range.....	95
Table A-4. The interpolated flux for element 970. For this test case, a subset of interpolated fluxes is shown, covering sizes from 10 μm to 100 μm for the HD family. Bold text indicates the three reference points in this size range.....	96

1.0 INTRODUCTION

1.1 Purpose and Scope

The NASA Orbital Debris Engineering Model (ORDEM) 3.1 – Model Process document accompanies the delivery of the latest ORDEM 3.1 model (Vavrin, *et al.*, 2019) and covers details of the mathematical, statistical, and physical basis of the model populations, as built based on existing supporting models and datasets. This ORDEM 3.1 Model Process document, along with the related ORDEM 3.1 V&V document (Kennedy, *et al.*, 2022) – which discusses activities used to verify that the model was built correctly and validate the model against independent, real world sources of data are intended to inform credibility assessments, risk analyses, uncertainty characterizations, and other applications derived from use of the model by the ORDEM 3.1 user community.

1.2 ORDEM 3.1 – An Engineering Model

ORDEM 3.1 supersedes the previous NASA Orbital Debris Program Office (ODPO) model – ORDEM 3.0 (Stansbery, *et al.*, 2014). The availability of new sensor and *in situ* data, the re-analysis of existing data, and the development of new analytical techniques has enabled the construction of this more comprehensive and sophisticated model.

1.2.1 Requirements for an Engineering Model

The primary requirement for any engineering model is to provide the user with efficient and accurate results. The two main types of ORDEM users are spacecraft designers/operators and debris researchers. A third user group includes mission planners and analysts using the ODPO Debris Assessment Software (DAS) package, which implements ORDEM populations in calculations for spacecraft damage probability.

The requirements of each user group differ somewhat, though they share many common requirements. To facilitate implementation of cost-effective shielding, spacecraft designers require detailed estimates of the particle flux as a function of local azimuth/elevation, debris size, and relative velocity. Because of the evolving temporal behavior of the debris environment, the satellite's launch date and planned on-orbit lifetime are also important.

When an observer is planning a debris observation campaign, predicted fluxes are used to ensure that the experiment planning and design can accommodate the quantity and rate of data collection. Ultimately, measurements will be compared to the model predictions and will be the final figure of merit for the model's veracity. Predicted fluxes will depend upon the inclination and altitude distribution of resident space objects visible from the ground-based sensor location. Additionally, an observer must consider whether the sensor is fixed in its orientation or is steerable in azimuth and elevation.

Thus, any such engineering model must include, at a minimum, an accurate assessment of the orbital debris (OD) environment as a function of altitude, latitude, and debris size. ORDEM is consistent with this requirement. It is based on debris populations with various altitude, inclination, and size distributions. The model provides a complete description of the environment, including debris flux onto spacecraft surfaces or the debris detection rate observed by a ground-based sensor.

1.2.2 Limitations of an Engineering Model

Some studies are beyond the scope of the ORDEM series of models. ORDEM is designed to provide yearly estimates of the debris environment. For example, the models cannot reliably evaluate the short-term collision risk between fragments from recent breakup events and an orbiting satellite. Such an assessment requires highly accurate orbital positioning and propagation – a task that the NASA ODPO Satellite Breakup Risk-Assessment Model (SBRAM) accomplishes (Gates and Matney, 2020). Studies of the long-term effect of various mitigation measures on the debris environment must rely on a debris

evolutionary model. The NASA ODPO's LEO-to-GEO ENvironment Debris (LEGEND) model (Liou, *et al.*, 2004) is applicable for examining the consequences of such phenomena. Additionally, the application of telescope/radar debris assessments is limited to ground-based (specifically, pencil-beam type) sensors.

1.2.3 Historical Overview

The first OD engineering model was developed for the U.S. Space Station Program Office in 1984. Later models were assembled for the Strategic Defense Initiative Organization, for various low Earth orbit (LEO) spacecraft programs (Kessler, 1989), and for the Space Station Program Office (Kessler, 1991). Each of these portrayed the environment as curve fits to describe the distributions of large objects (larger than approximately 10 cm, as cataloged by the U.S. Space Surveillance Network [SSN]) and small objects (as recorded by the inspection of surfaces exposed to and returned from space). Both periodic (solar cycle) and secular (launch traffic and fragmentation growth rate) effects were included explicitly. A significant requirement of these models was that they be easily executed by a programmable calculator or be capable of manual implementation within a reasonable time.

The need to better define the debris environment eventually outgrew this latter requirement. ORDEM96, (Kessler, 1996) was the first model that required a personal computer for effective implementation. ORDEM96 pioneered the use of debris population ensembles characterized by altitude, eccentricity, inclination, and size. ORDEM2000 (Liou, *et al.*, 2002) adopted a similar approach, but it replaced the final remnants of curve fitting, as used by all previous NASA debris engineering models, with a finite element model to represent the debris environment. ORDEM 3.0 (released in 2013) represented a significant upgrade in terms of model features and capabilities. It extended the model to the geosynchronous orbit (GEO) region (up to 40,000 km), which enabled analysis of more varied orbits – such as geosynchronous transfer orbits (GTO) and other highly-elliptical orbits – and ground sensor orientations. Additional upgrades included the expansion of observation program datasets in underrepresented regions and the addition of uncertainties on the reported OD fluxes. Most significantly, ORDEM 3.0 included a distribution in material density of OD fluxes, including specific populations for low-, medium-, and high-density fragments, intact, and sodium-potassium (NaK) droplets. Details of the material density breakdown are discussed in Section 1.3.6. The current version of the model, ORDEM 3.1, includes the same capabilities as ORDEM 3.0, but updates the model populations using the most recent and highest-fidelity datasets from radar, *in situ*, and optical sources. These sources and their use for building the ORDEM 3.1 populations are discussed in Section 3.0. Table 1-1 compares the features of ORDEM2000, ORDEM 3.0, and ORDEM 3.1.

Note that the altitude range with a minimum debris size requires some further explanation. While GTO objects are not as well observed as those in LEO; nevertheless, direct observations of a portion of the GTO populations are sampled with radar and returned surfaces that cover the entire size range from 10 μ m to 1 m. ORDEM, therefore, models fluxes for debris greater than 10 μ m with non-GEO (LEO and GTO) orbits. For GEO, observations are limited to ground-based telescopes. These telescopes have a larger minimum size visible in GEO than ground-based sensors used to observe LEO debris. Therefore, ORDEM provides GEO debris fluxes for 10 cm and larger only. Any fluxes below the 10 cm threshold reported for GEO altitudes are solely due to GTO objects.

Debris engineering models are not limited to the NASA models. For example, the European Space Agency (ESA) Meteoroid and Space Debris Terrestrial Environment Reference (MASTER) (Sdunnus, 2001) series of models performs similar functions, as does the Russian Federation Space Debris Prediction and Analysis (SDPA) model (Usovsk, *et al.*, 2017). MASTER-2005, MASTER-2009, and MASTER-8 (Oswald, *et al.*, 2006, Flegel, *et al.*, 2011, and Horstmann, *et al.*, 2020) are similar to the latest in the ORDEM series of models (ORDEM2000, ORDEM 3.0, and ORDEM 3.1, respectively).

Table 1-1 Feature comparison of ORDEM2000, ORDEM 3.0, and ORDEM 3.1

Parameter	ORDEM2000	ORDEM 3.0	ORDEM 3.1
Spacecraft & Telescope/Radar analysis modes	Yes	Yes	Yes
Time range	1991 to 2030	2010 to 2035	2016 to 2050
Altitude range with minimum debris size	200 to 2000 km ($>10 \mu\text{m}$) (LEO)	100 to 40,000 km ($>10 \mu\text{m}$) (non-GEO) 34,000 to 40,000 km ($>10 \text{ cm}$) (GEO)	100 to 40,000 km ($>10 \mu\text{m}$) (non-GEO) 34,000 to 40,000 km ($>10 \text{ cm}$) (GEO)
Orbit types of debris populations	Circular (radial velocity ignored)	Circular to highly elliptical	Circular to highly elliptical
Model population breakdown by type & material density	No	Intacts Low-density (1.4 g/cc) fragments Medium-density (2.8 g/cc) fragments & microdebris High-density (7.9 g/cc) fragments & microdebris NaK coolant droplets (0.9 g/cc)	Intacts Low-density (1.4 g/cc) fragments Medium-density (2.8 g/cc) fragments & microdebris High-density (7.9 g/cc) fragments & microdebris NaK coolant droplets (0.9 g/cc)
Model cumulative size thresholds (<i>fiducial points</i>)	10 μm , 100 μm , 1 mm, 1 cm, 10 cm, 1 m	10 μm , 31.6 μm , 100 μm , 316 μm , 1 mm, 3.16 mm, 1 cm, 3.16 cm, 10 cm, 31.6 cm, 1 m	10 μm , 31.6 μm , 100 μm , 316 μm , 1 mm, 3.16 mm, 1 cm, 3.16 cm, 10 cm, 31.6 cm, 1 m
Flux uncertainties	No	Yes	Yes
Total population file size	13.5 MB	1.25 GB	4 GB

1.3 ORDEM 3.1 Program Philosophy

The core capability of the ORDEM program is to compute fluxes. Flux in this context is the directional rate (per unit time) that debris from a particular population and of a given size and larger would strike a hypothetical spherical spacecraft with unit cross-sectional area ($\pi r^2 = 1 \text{ m}^2$) or cross through a ground-based sensor's field of view with unit cross-sectional area (1 m^2). For spacecraft, the direction is important in computing the projected area of a spacecraft element. ORDEM also breaks down the flux by relative velocity (in the frame of the spacecraft) and material density, which is important for damage assessments. Therefore, the flux is a function of year, size, material type, and for spacecraft, elevation/azimuth in the local spacecraft frame, and velocity in the local spacecraft frame. For ground-based telescope/radar sensors, the flux is also a function of range relative to the sensor location and geometry. This range corresponds to a specific altitude, which can in turn correspond to a different latitude because of the sensor latitude and boresight azimuth and elevation.

In ORDEM, the spacecraft flux is integrated over the entire orbit, calculating the fraction of time the spacecraft spends at different points in its orbit. This requires that the spatial density and velocity vector of each population sub-component be computed. Such a task is computationally-intensive, hence the sometimes long computation times in ORDEM 3.0 and 3.1.

1.3.1 Orbit Spatial Densities

The spatial density for the LEO debris populations is computed using a modified version of the Kessler density function (Kessler, 1978). The spatial density is computed using the assumption that the argument of perigee and ascending node of a particular orbit are distributed randomly. For the vast majority of debris in LEO, this is an accurate assumption. However, there are orbit families where this is not strictly true, such as the Sun-synchronous, *Molniya*, and “fresh” breakup families of objects.

The Sun-synchronous family is a large retrograde grouping of debris and intact objects that have an ascending node fixed relative to the Sun. While active satellites maintain the ascending node, debris (especially from energetic breakups) from this family quickly (in a period of months) evolve until their orbits are thoroughly randomized in ascending node. Similarly, objects in polar orbits have very slow precession of the ascending nodes, but the parent bodies do not typically have preferred ascending nodes, so the debris typically do not have preferred planes. In both cases, the debris orbits can be approximated to be randomly distributed in ascending node.

The *Molniya* family is a group of Russian satellites that are launched into elliptical orbits with perigees fixed in the southern hemisphere. Breakup debris from these orbits tend to have sufficient delta-velocity to lose “perigee lock” and have their arguments of perigee precess to the point where they can be considered to be randomized.

The third family, which does not necessarily exhibit random distributions in argument of perigee and ascending node, is from “fresh” breakups. Typically, the initial orbits of these debris are distributed in specific bands of ascending node and argument of perigee, depending on the location of the breakup. These orbit nodes also typically evolve to be randomized in a short time, so these populations should be sufficiently randomized over the relatively long 1-year time scale on which ORDEM models fluxes.

One problem with the Kessler density is that it can have infinite density at apogee, perigee, and the northernmost and southernmost points in an orbit. Kessler used an approximation to deal with this effect, but issues remained. In ORDEM, the problem with the infinite values is handled by modeling debris using orbit distributions instead of discrete orbits. The corresponding spatial density of a distribution of orbits no longer has any infinite densities, though one must be careful with the numerical integration.

1.3.2 Orbit Distributions

The orbit distributions in ORDEM were chosen to map out the distributions in orbit parameters naturally. Kepler elements are not unique, and a number of different ways are available for unambiguously defining an orbit. For most objects, the natural mapping uses units of inclination, perigee altitude, and eccentricity. Here, these are termed “non-GEO” objects, and encompass LEO and highly-elliptical (e.g., GTO) orbits. The parameter binning is also important, depending on how the orbiting objects are expected to be distributed. The spacing of the eccentricity bins is especially challenging, since the binning scheme needs to have a higher resolution near zero eccentricity, where the distribution in altitude is sensitive to the eccentricity, but also allow for a more granular spacing at higher eccentricities. To satisfy this criterion, the eccentricity bin spacings are proportional to the square root of the eccentricity. There is a total of 74 eccentricity bins, 240 inclination bins (spacing 0.75°), and 287 perigee altitude bins with varying resolution, with the LEO (up to 2000 km altitude) bins being 33.333 km wide.

All of the binning choices were initially compromises between memory storage and resolution during the development of ORDEM 3.0. Table 1-2 summarizes the bin ranges for the non-GEO populations, and Figure 1-1 through Figure 1-7 show examples of how the cataloged populations are distributed.

Table 1-2. Non-GEO population binning in ORDEM.

Parameter	Bin Number and Range of Bins	Bin Spacing
Eccentricity	74 (0.0 – 1.0)	0.013333 in $\text{Sqrt}(\text{Eccentricity})$, with smallest two bins merged
Inclination	240 (0° – 180°)	0.75°
Perigee Altitude	1-57 (100 – 2000 km) 58-137 (2000 – 10000 km) 138-287 (10000 – 40000 km)	33.3333 km 100 km 200 km

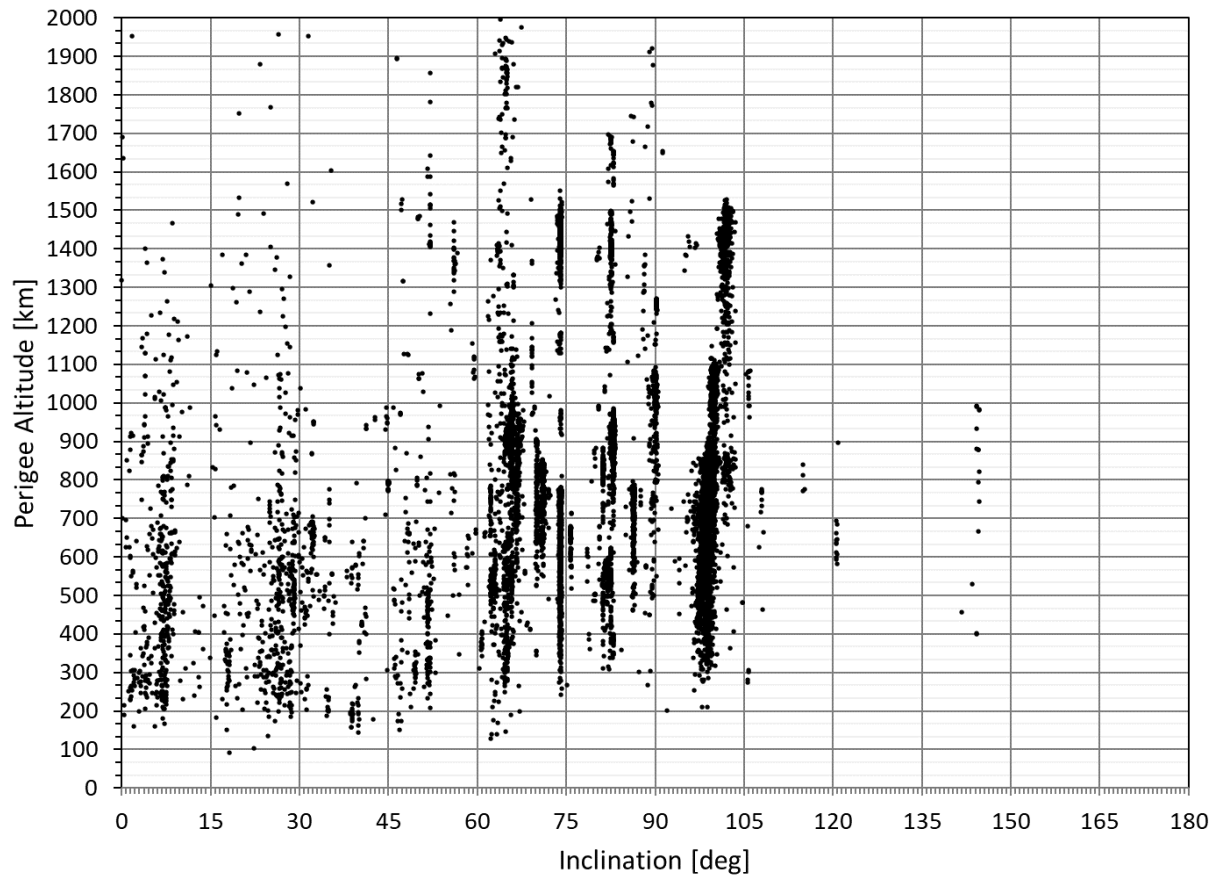


Figure 1-1. A 2010 catalog distribution of non-GEO orbiting objects in inclination and perigee altitude, with the tick marks showing the ORDEM binning resolution. For clarity, only the perigee altitudes corresponding to the bins 1–57 (100–2000 km with 33.33 km bin spacing) are shown in this figure.

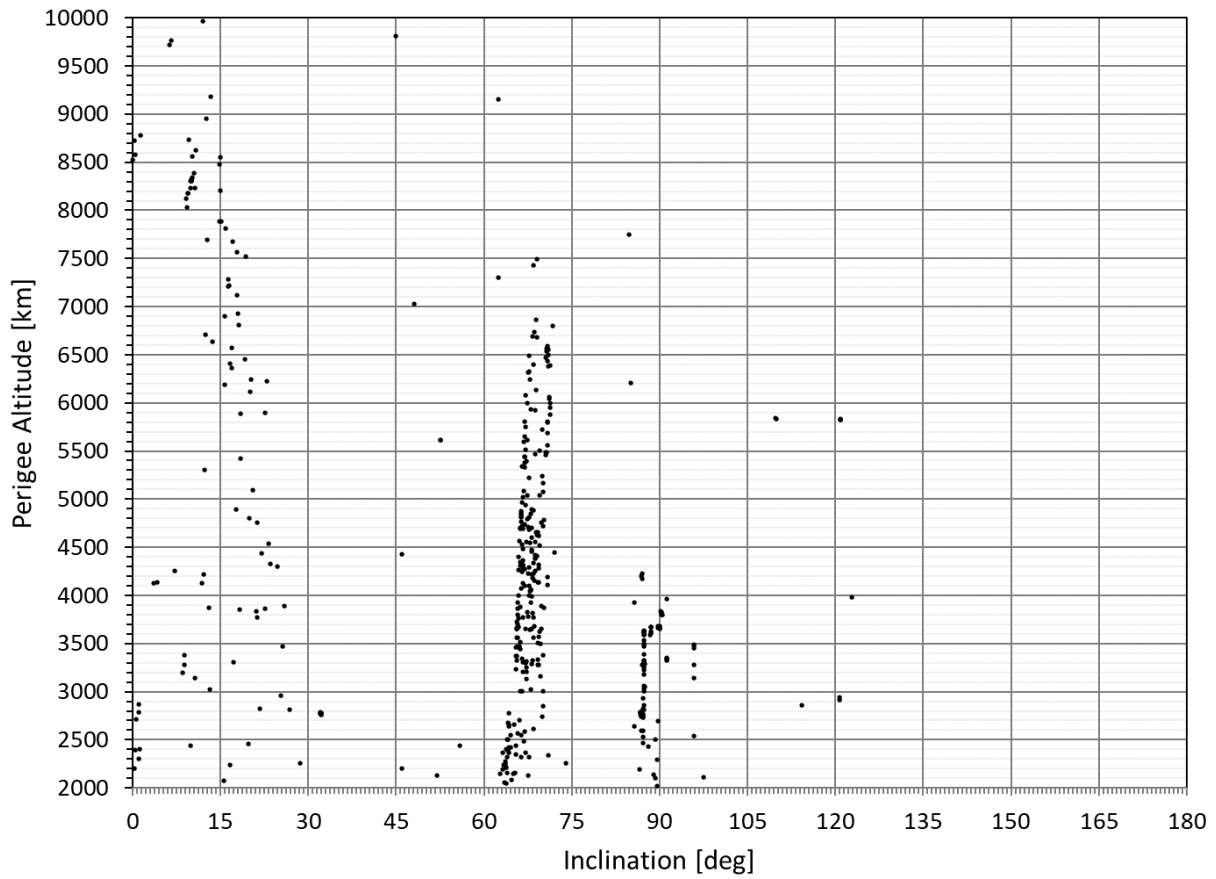


Figure 1-2. A 2010 catalog distribution of non-GEO orbiting objects in inclination and perigee altitude, with the tick marks showing the ORDEM binning resolution. For clarity, only the perigee altitudes corresponding to the bins 58–137 (2000–10000 km with 100 km bin spacing) are shown in this figure.

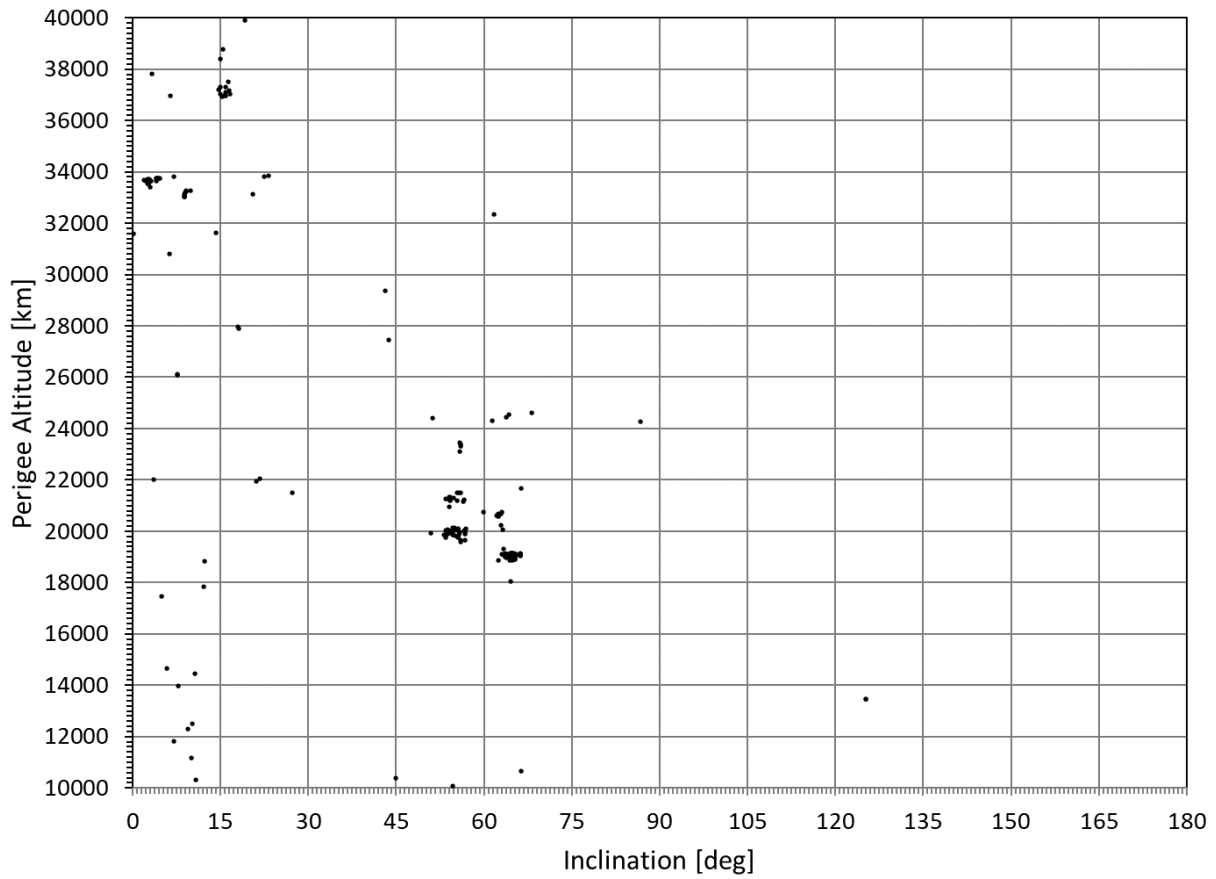


Figure 1-3. A 2010 catalog distribution of non-GEO orbiting objects in inclination and perigee altitude, with the tick marks showing the ORDEM binning resolution.
 For clarity, only the perigee altitudes corresponding to the bins 138–287 (10000–40000 km with 200 km bin spacing) are shown in this figure.

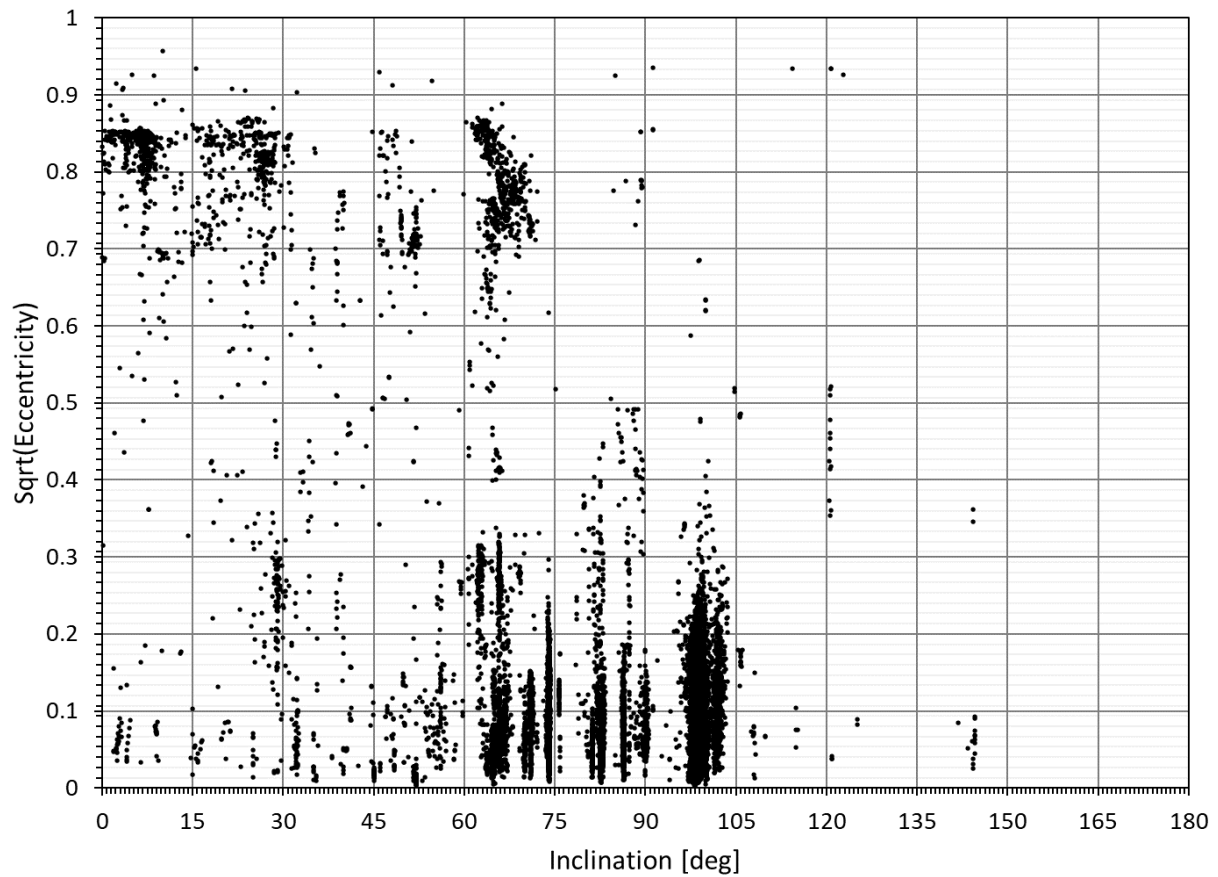


Figure 1-4. A 2010 catalog distribution of non-GEO orbiting objects in inclination and square root of eccentricity, with the tick marks showing the ORDEM binning resolution. Note that objects in ORDEM are binned according to their eccentricity, but the y-axis here is $\text{Sqrt}(\text{eccentricity})$ to show how the eccentricity bins are uniform in $\text{Sqrt}(\text{eccentricity})$ space.

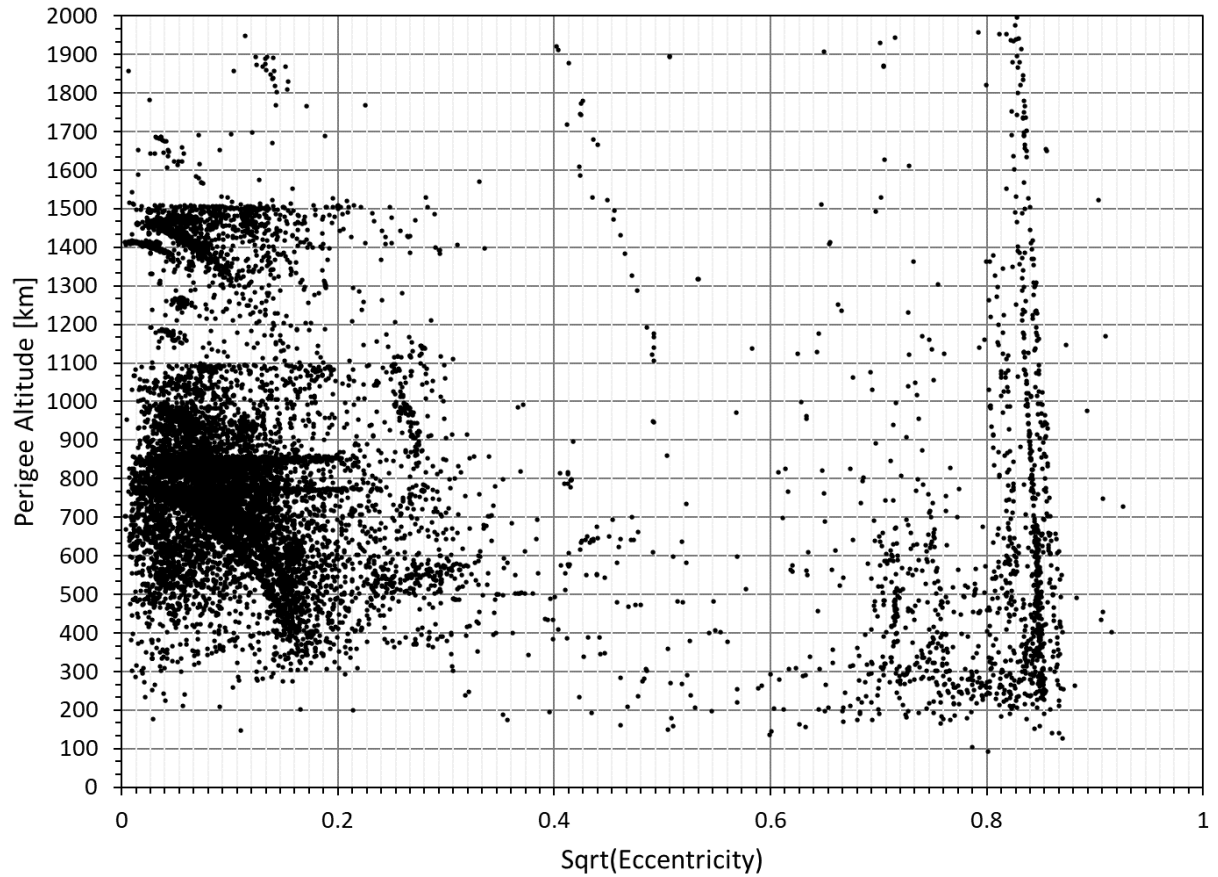


Figure 1-5. A 2010 catalog distribution of non-GEO orbiting objects in perigee altitude and square root of eccentricity, with the tick marks showing the ORDEM binning resolution. Note that objects in ORDEM are binned according to eccentricity, but the x-axis here is $\text{Sqrt}(\text{eccentricity})$ to show how the eccentricity bins are uniform in $\text{Sqrt}(\text{eccentricity})$ space. For clarity, only the perigee altitudes corresponding to the bins 1–57 (100–2000 km with 33.33 km bin spacing) are shown in this figure.

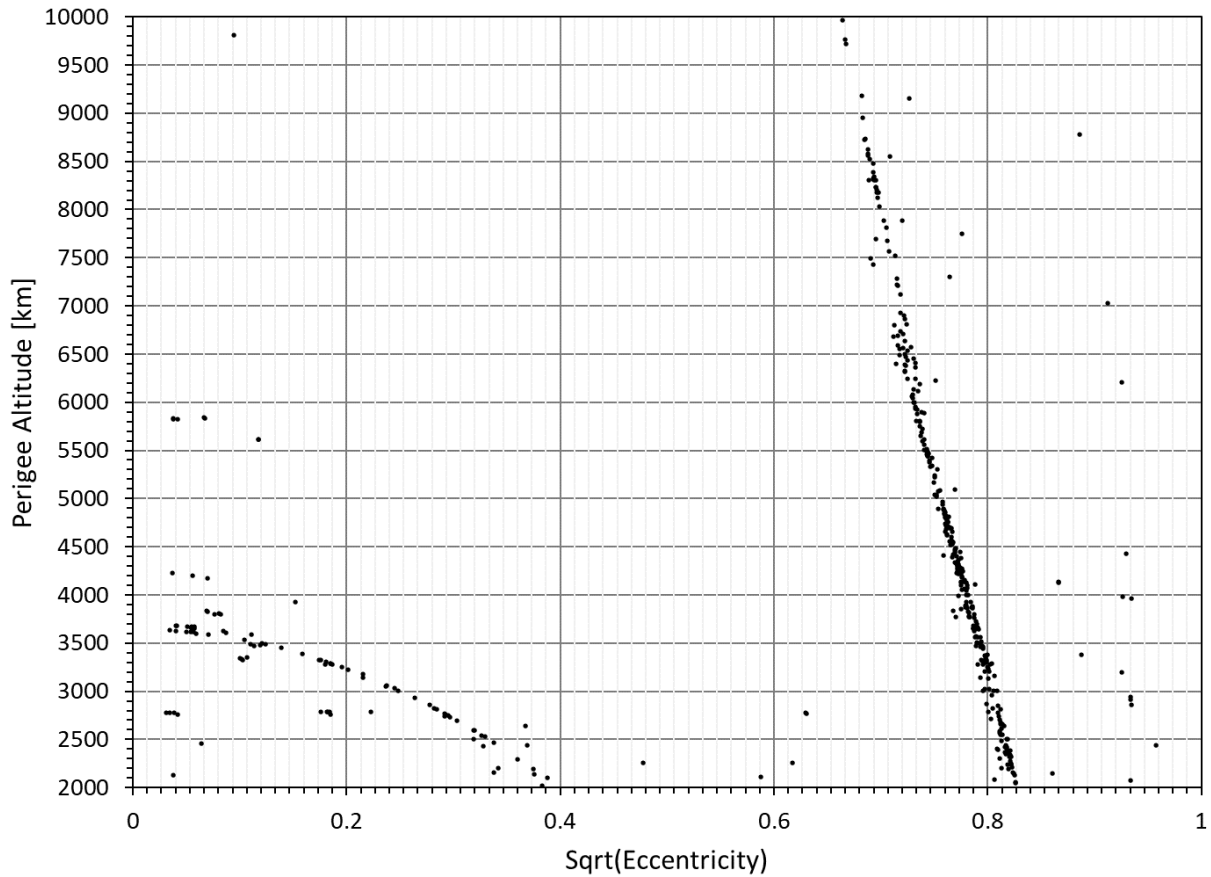


Figure 1-6. A 2010 catalog distribution of non-GEO orbiting objects in perigee altitude and square root of eccentricity, with the tick marks showing the ORDEM binning resolution. Note that objects in ORDEM are binned according to eccentricity, but the x-axis here is $\text{Sqrt}(\text{eccentricity})$ to show how the eccentricity bins are uniform in $\text{Sqrt}(\text{eccentricity})$ space. For clarity, only the perigee altitudes corresponding to the bins 58–137 (2000–10000 km with 100 km bin spacing) are shown in this figure.

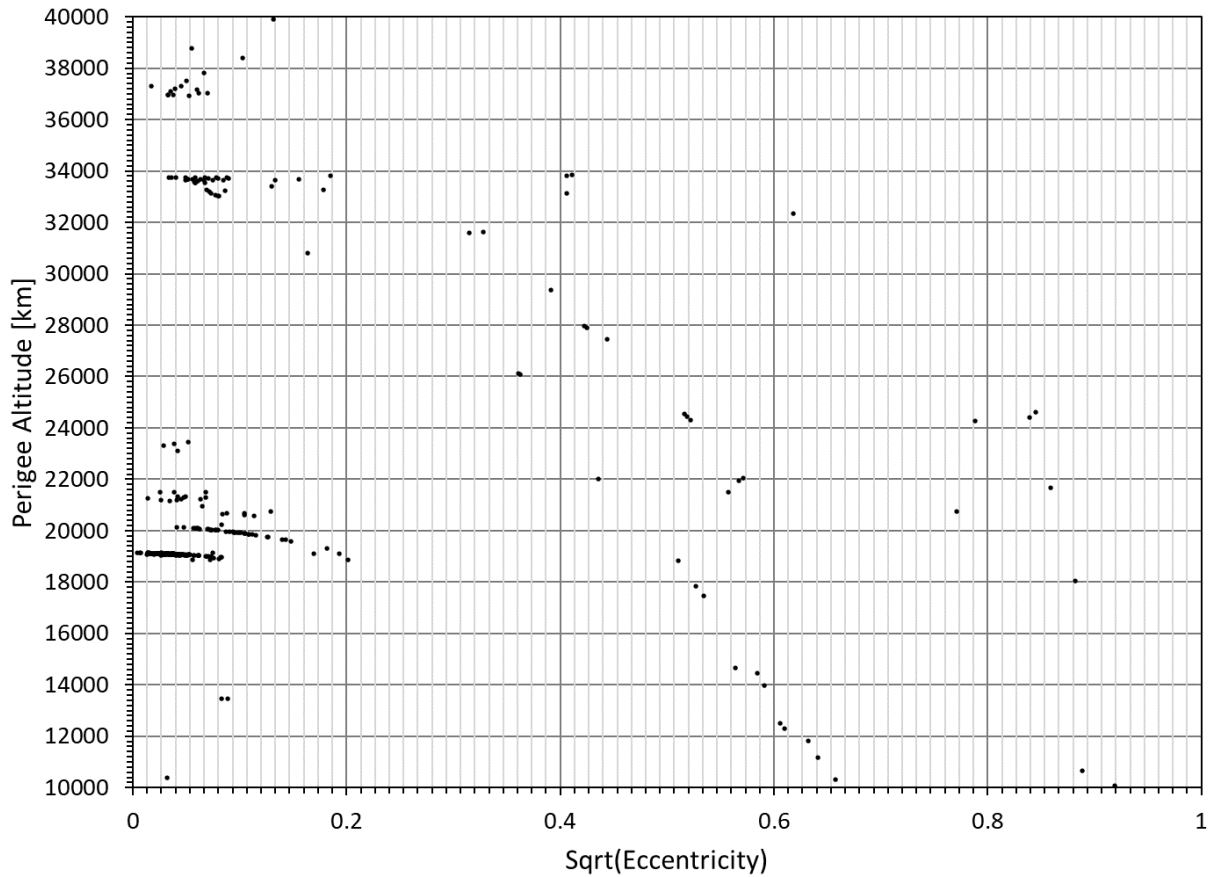


Figure 1-7. A 2010 catalog distribution of non-GEO orbiting objects in perigee altitude and square root of eccentricity, with the tick marks showing the ORDEM binning resolution. Note that objects in ORDEM are binned according to eccentricity, but the x-axis here is $\text{Sqrt(Eccentricity)}$ to show how the eccentricity bins are uniform in $\text{Sqrt(eccentricity)}$ space. For clarity, only the perigee altitudes corresponding to the bins 138–287 (10000–40000 km with 200 km bin spacing) are shown in this figure.

1.3.3 GEO Populations

Binning the GEO population in ORDEM is more difficult than for the non-GEO populations because the natural relationship between ascending node and inclination needs to be taken into account. Argument of perigee is treated as random, however. Instead of using the perigee altitude, the GEO population is binned in mean motion to better reflect the behavior of objects in this orbit regime. Table 1-3 summarizes the bin ranges for the GEO populations, and Figure 1-8 through Figure 1-11 show examples of how the catalogued populations are distributed.

Table 1-3. GEO population binning in ORDEM.

Parameter	Bin Number and Range of Bins	Bin Spacing
Eccentricity	25 (0.0 – 0.25)	0.02 in $\text{Sqrt}(\text{Eccentricity})$
Inclination	1 (0° – 0.2°) 2 (0.2° – 1°) 3–26 (1° – 25°)	0.2° 0.8° 1°
Mean Motion	1–45 (0.5 – 0.95 revs/day) 46–145 (0.95 – 1.05 revs/day) 146–220 (1.05 – 1.8 revs/day)	0.01 revs/day 0.001 revs/day 0.01 revs/day
Right Ascension of the Ascending Node	1–72 (0° – 360°)	5°

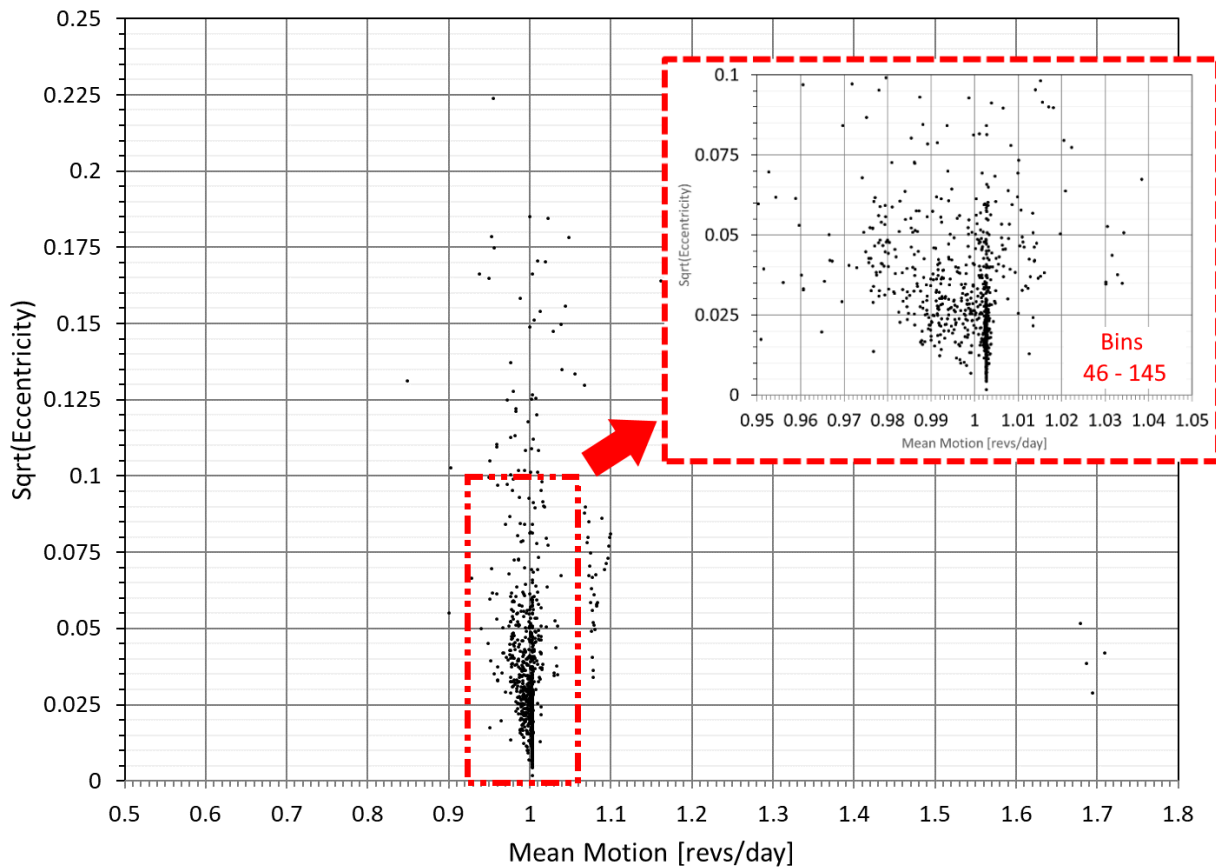


Figure 1-8. A 2010 catalog distribution of GEO objects in mean motion and square root of eccentricity, with the tick marks showing the ORDEM binning resolution. The figure inset shows a zoomed-in region of GEO objects with a mean motion between 0.95 to 1.05 revs/day, which are binned with 0.001 revs/day-bin spacing. Note that objects in ORDEM are binned according to their eccentricity, but the y-axis here is $\text{Sqrt}(\text{eccentricity})$ to show how the eccentricity bins are uniform in $\text{Sqrt}(\text{eccentricity})$ space.

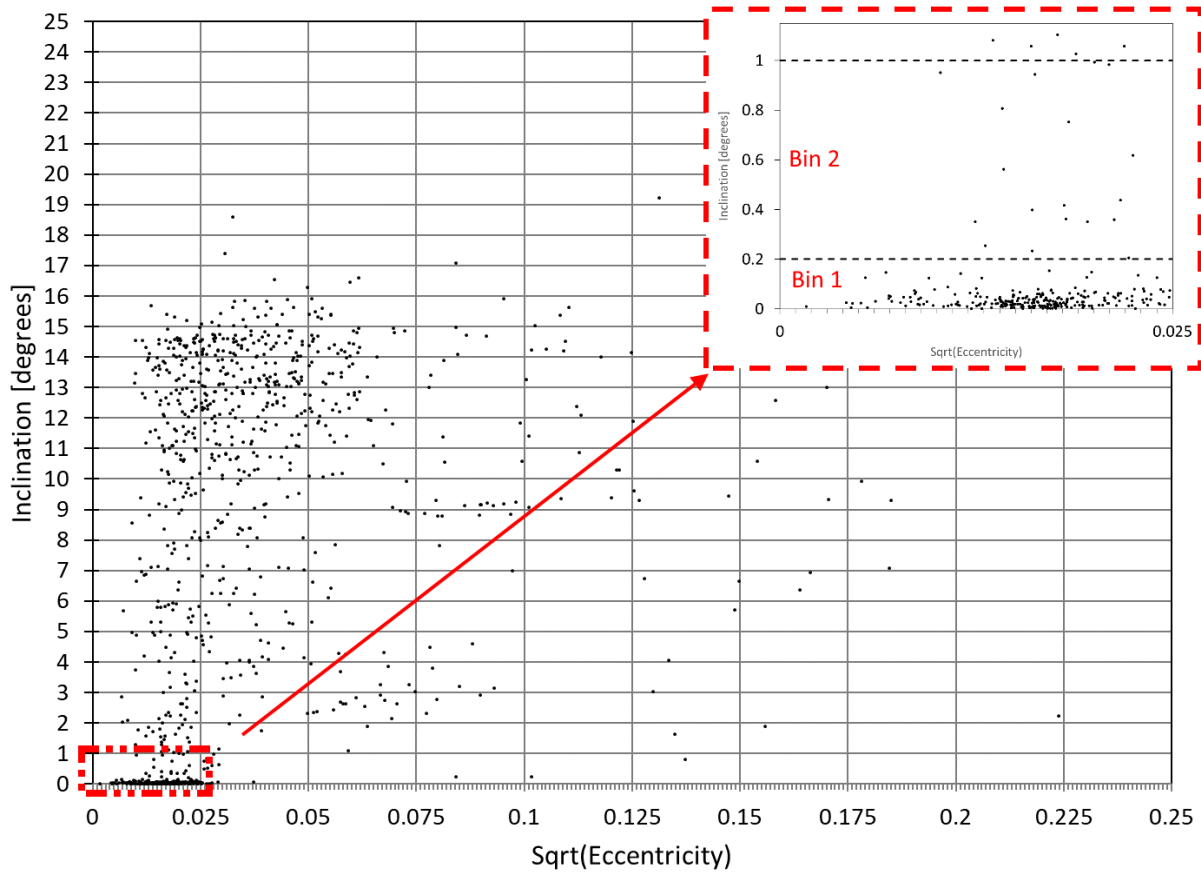


Figure 1-9. A 2010 catalog distribution of GEO objects in inclination and square root of eccentricity, with the tick marks showing the ORDEM binning resolution. The figure inset shows a zoomed-in region of GEO objects with inclination less than 1°; GEO objects in ORDEM with an inclination between 0.0° to 0.2° are stored in bin 1, and objects with an inclination between 0.2° and 1.0° are stored in bin 2.

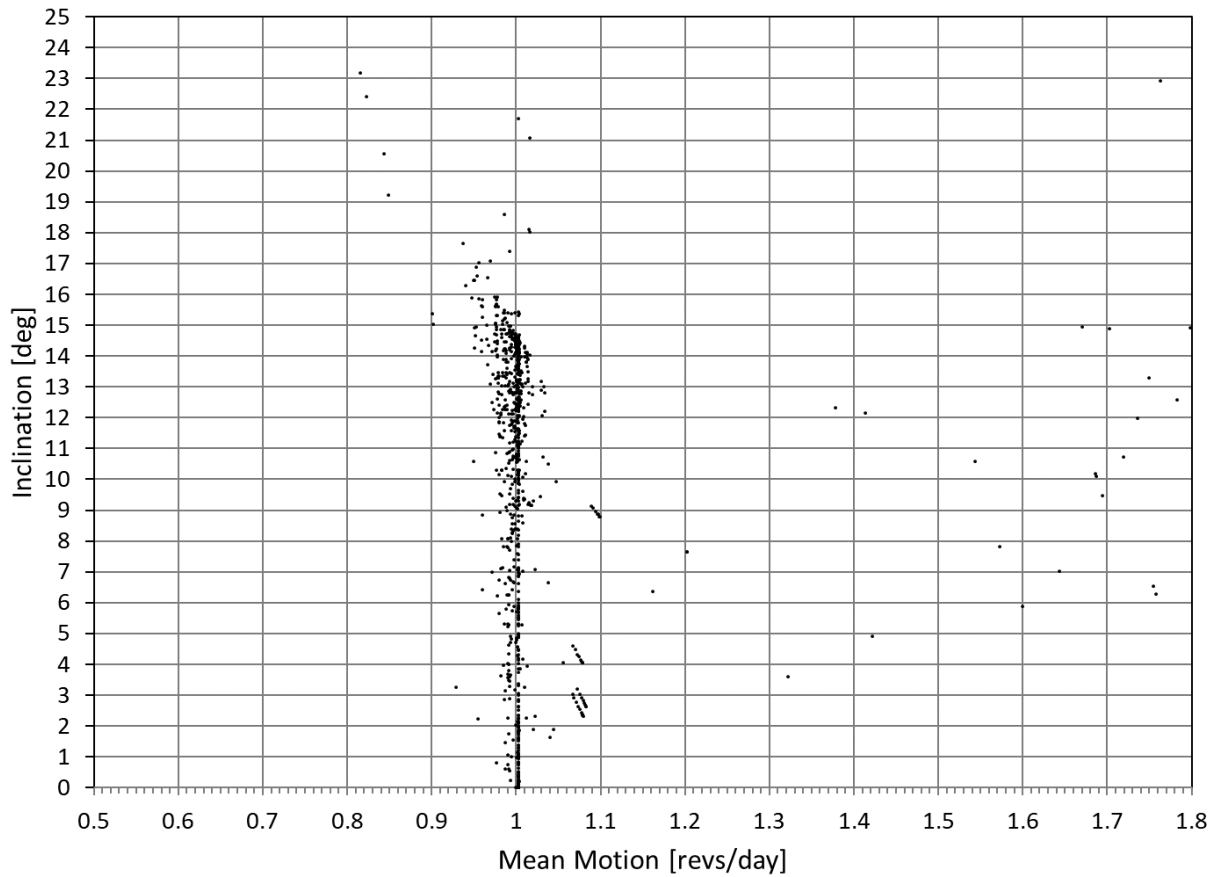


Figure 1-10. A 2010 catalog distribution of GEO objects in mean motion and inclination. The x-axis shows mean motion with tick mark spacing of 0.01 revs/day for clarity; however, GEO objects in ORDEM with a mean motion between 0.95 to 1.05 revs/day are binned with 0.001 revs/day-bin spacing (see Figure 1-8).

The y-axis (inclination) shows inclination with gridline spacing of 1° for clarity; however, GEO objects in ORDEM with an inclination between 0.0° to 0.2° are stored in bin 1, and objects with an inclination between 0.2° and 1.0° are stored in bin 2 (see Figure 1-9).

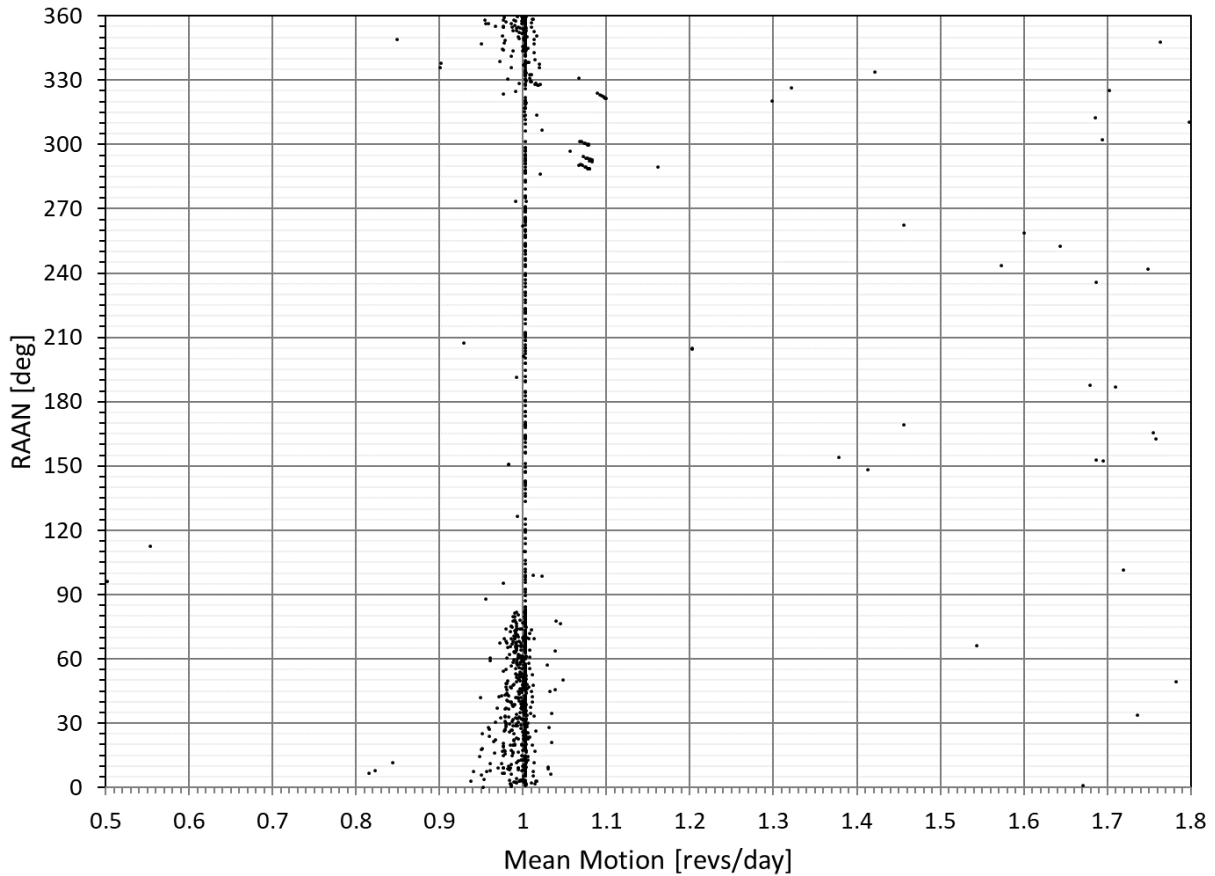


Figure 1-11. A 2010 catalog distribution of GEO objects in mean motion and right ascension of the ascending node. The x-axis shows mean motion with tick mark spacing of 0.01 revs/day for clarity; however, GEO objects in ORDEM with a mean motion between 0.95 to 1.05 revs/day are binned with 0.001 revs/day-bin spacing (see Figure 1-8).

As noted previously, some non-GEO bins may overlap with GEO bins (e.g., for highly-elliptical orbits with high perigee altitudes), in which case the fluxes from both regimes will contribute to the total flux in those regions where the spatial extent of the populations overlap.

1.3.4 Igloo Elements

The ORDEM spacecraft flux computation uses the concept of an encompassing 3-dimensional “igloo” around the spacecraft, where each igloo element is defined as a finite element in elevation (or pitch), azimuth (or yaw), and relative velocity spaces. The default igloo in the ORDEM model is the $10^\circ \times 10^\circ \times 1$ km/s igloo, which has relative velocity bins from 0 to 23 km/s in 1 km/s increments, elevation/pitch from -85° to 85° in 10° increments, and azimuth/yaw from -180° to 180° in 10° increments, with two “polar caps” from -90° to -85° and 85° to 90° in elevation/pitch and -180° to 180° in azimuth/elevation. Another igloo option included in ORDEM is the $30^\circ \times 30^\circ \times 2$ km/s igloo, which has relative velocity bins from 0 to 24 km/s in 2 km/s increments, elevation/pitch from -90° to 90° in 30° increments, and azimuth/yaw from -180° to 180° in 30° increments, with two “polar caps” from -90° to -85° and 85° to 90° in elevation/pitch and -180° to 180° in azimuth/elevation. Figure 1-12 shows a high-level schematic of how one igloo element represents multiple orbits (i.e., perigee and eccentricity values).

The spacecraft's perigee altitude, eccentricity, and inclination are used to calculate the appropriate igloo element. For telescope flux computation, the finite elements are distributed in beam altitude only.

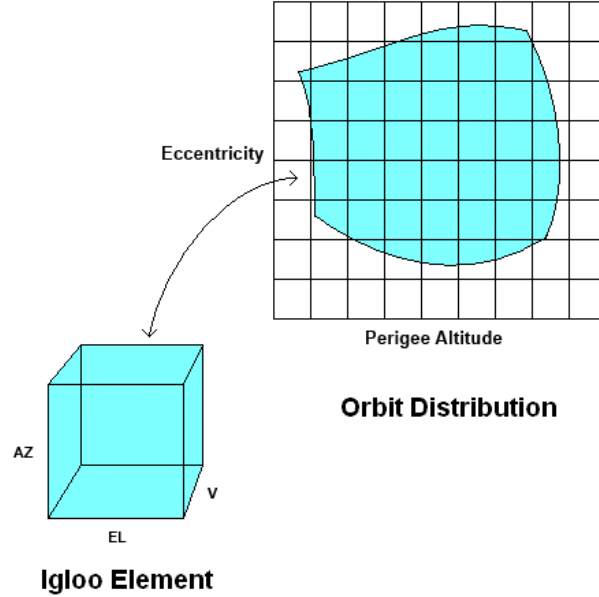


Figure 1-12. Conceptual relation between one igloo element (elevation, azimuth, relative velocity) and its orbit distribution (perigee, eccentricity)

1.3.5 Debris Sizes

Fluxes calculated in ORDEM are mainly categorized in terms of debris size, or characteristic length. The characteristic length, L_c , of an object is defined as the average of the largest projected dimensions for an object measured along three orthogonal axes:

$$L_c = \frac{X + Y + Z}{3}. \quad 1.3-1$$

The first axis coincides with the largest dimension, the second axis is the longest projection length in a plane orthogonal to the first axis, and the third axis is chosen to complete the orthogonal triad.

Figure 1-13 shows an example of body dimensions of a complex-shaped object projected to a 2-dimensional surface. Note the projection measurement for Y is used for the calculation of L_c .

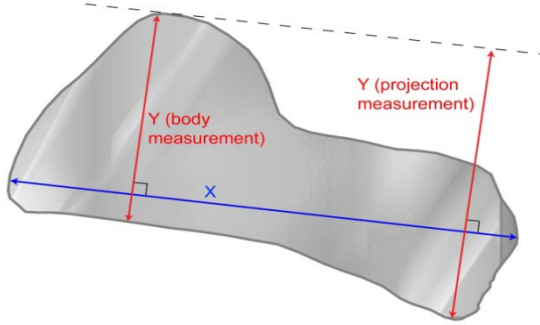


Figure 1-13. Illustration of body and projected measurement on complex shape (Hill, 2008).

It is important to note the Z dimension is not always the thickness of the object, due to curling, bending and other vertical projections. The characteristic length was determined to best represent the diameter of an object by averaging the three projected dimensions of any shape based on radar cross section (RCS) data, which is true for a sphere. This parameter is also used to define the median area one would expect to measure as an object tumbles or rotates in space. This characteristic length is also referred to in the remainder of this report as the size or diameter of the debris.

1.3.6 Material Densities

Before ORDEM 3.0 was released, the ODPO surmised that its small debris (1 mm to 10 cm) and microdebris (10 μ m to 1 mm) populations that were tagged with material density would lead to changes in the modeled environment. Earlier versions of ORDEM modeled debris smaller than 10 cm as aluminum spheres. However, different materials can pose different levels of risk to space vehicles, depending on the vehicle structure and shielding mechanisms, and they are thus important for micrometeoroid and orbital debris (MMOD) risk assessments. Investigations prior to the release of ORDEM 3.0 led to the ODPO separating materials into three categories: low-density (LD, representing plastics and phenolic, $\rho < 2 \text{ g/cm}^3$), medium-density (MD, representing aluminum and paint, $2 \leq \rho \leq 6 \text{ g/cm}^3$), and high-density (HD, representing steel and copper, $\rho > 6 \text{ g/cm}^3$). These material classes were maintained in ORDEM 3.1, except that the lower boundary of the HD category was further extended from 6 g/cm^3 down to 4.5 g/cm^3 , thereby designating impacts from titanium alloys as belonging to the population of HD debris instead of the MD population. These three categories were shown to be general in spacecraft and rocket body designs, though percentages within these vehicles vary (Opiela, 2009). Spacecraft appear to contain a non-trivial percentage of LD material, while rocket bodies contain more MD and HD materials. Modeled fragmentation debris and degradation particles are assigned material densities based on distributions seen in laboratory and *in situ* measurement data, as discussed in Sections 3.1.1 and 3.2.2.

2.0 SUPPORTING MODELS: LEGEND

NASA's full-scale, 3-dimensional debris evolutionary model, LEGEND, was developed in 2003 (Liou, *et al.*, 2004). It covers the Earth orbital space environment between 90 and 40,000 km altitude, including LEO (200–2000 km altitude), medium Earth orbit (MEO, 2000–34,000 km altitude), GEO (34,000–38,000 km altitude), and supersynchronous orbit (38,000 km and above) regions. The model is capable of providing debris characteristics (size distribution, spatial density distribution, velocity distribution, flux, *etc.*) as functions of time, altitude, longitude, and latitude. It also models known historical collisions and explosions as well as postmission disposal (PMD) and statistical breakup events during future propagation. The NASA ODPO typically uses LEGEND to evaluate the instability of the current debris environment and assess the long-term growth of the future debris populations. LEGEND also provides

the initial reference populations of intact (rocket bodies, spacecraft, and mission-related debris) and fragmentation debris (from explosions and collisions) for ORDEM.

Files developed by the ODPO containing information on known historical populations – including launched intact, maneuvers conducted in space (e.g., re-orbit or deorbit maneuvers), and fragmentation events (collisions and explosions) – serve as the inputs to LEGEND. These input space traffic files are predicated on the SSN catalog, which is maintained by the U.S. Department of Defense and contains information on trackable space objects that generally are 10 cm and larger in LEO and 1 m and larger in GEO. The historical simulation in LEGEND covers the period from 1957 to a specified epoch and adopts a deterministic approach to mimic the known historical launch traffic, maneuvers, and fragmentation events. Fragments for known historical breakup events are created using the NASA Standard Satellite Breakup Model (SSBM), which describes the size, area-to-mass ratio (A/m), and velocity distributions of the breakup fragments (Johnson, *et al.*, 2001). A customized scale factor is assigned to each historical explosion event such that the cumulative number of objects 10 cm and larger, generated from the breakup, matches the number of cataloged fragments. The motivation for using this approach is to better match the debris production of each event as recorded in the SSN catalog, which yields a better description of the historical debris environment and thus a better initial condition for future environment projections. Parameters for known breakup events include parent characteristic, event type, and state vector at the time of breakup. All objects are propagated forward in time, and decayed objects are removed from the environment immediately.

To simulate future traffic in LEGEND, future populations are added via an 8-year launch cycle, as commonly adopted by the international debris modeling community. Three constellations (Orbcomm, Iridium, and Globalstar) are repeated only until 2019. A given rate of compliance with PMD guidelines (*i.e.*, the “25-year rule”) is also assumed for future spacecraft and rocket bodies. After an 8-year operational life for spacecraft, the perigee altitude is lowered such that the object reenters the atmosphere within 25 years. For rocket bodies, PMD is assessed during the initial time step after launch. For the purposes of ORDEM 3.1, the PMD compliance rate was set to 90%. Future explosion and collision events are determined probabilistically (Liou, 2006), and fragments are generated using the SSBM. A Monte Carlo (MC) approach is adopted to simulate potential future on-orbit explosions and collisions. In general, averages from 100 MC runs are considered statistically sound and reliable (Liou, 2008; Stansbery, *et al.*, 2008). The spread in the possible future values (*i.e.*, the standard deviation of the MC runs) is folded into the uncertainty estimates for the debris populations.

The source orbits from the initial populations derived from LEGEND were binned by orbit parameters and the orbit population densities for ORDEM were assembled using these individual orbits. Non-GEO populations were binned by perigee altitude, inclination, and eccentricity, as indicated in Table 1-2. For GEO populations, the initial populations were binned by mean motion, inclination, eccentricity, and right ascension of the ascending node (RAAN), following the resolution indicated in Table 1-3.

3.0 DATA ANALYSIS AND POPULATION BUILDS

ORDEM 3.1, like its predecessors, is data-driven and uses data available from *in situ* and ground-based radar and optical sensors. Data from the SSN cataloged objects (e.g., orbital elements, launch date) are used to generate the space traffic files for LEGEND, which provide the basis for characterizing the environment from LEO to GEO. The estimation of debris populations below the threshold of the SSN sensors is dependent on dedicated statistical measurements from specialized sensors capable of detecting objects at smaller size ranges. Figure 3-1 shows the notional size and altitude coverage of datasets available for ORDEM 3.1 development and validation.

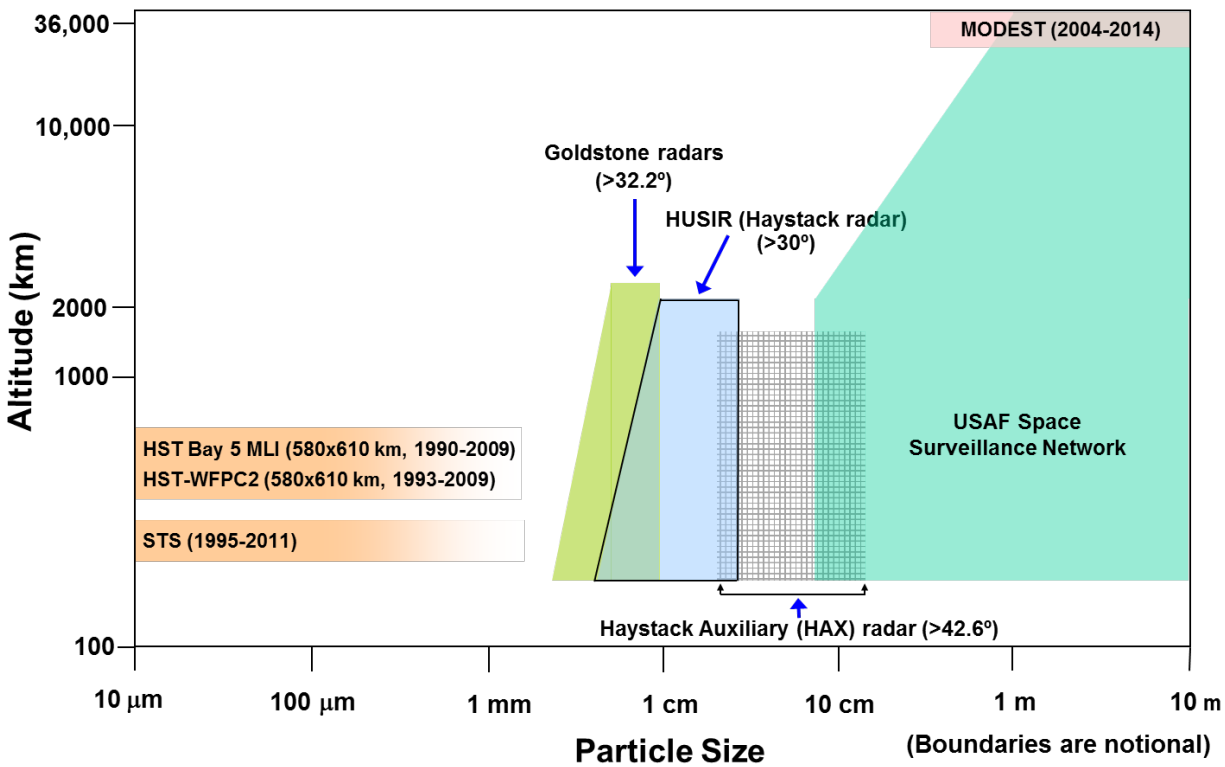


Figure 3-1. Measurement coverage for small debris from sources available for NASA models.

Table 3-1 lists the data sources used for building the ORDEM 3.1 populations, their size ranges, and the time periods covered in comparison to the ORDEM 3.0 source data. These data sets were used to build the radar-based populations (>1 mm), the degradation population ($10\text{ }\mu\text{m} - 3$ mm, based on *in situ* data sources), and the optical-based populations (>10 cm). The most recent available data were used for building the ORDEM 3.1 populations. Some specific older radar datasets were also reprocessed to better characterize major debris clouds.

Table 3-1. Data sources used for building the ORDEM 3.1 populations, with applicable size limits and years of coverage. Years covered by comparable datasets used for building ORDEM 3.0 populations are also shown for comparison.

Data Source	Size Limit (approximate)	Years Covered ORDEM 3.0	Years Covered ORDEM 3.1
STS windows	$10 - 300\text{ }\mu\text{m}$	1995–2011	1995–2011
STS radiators	$300\text{ }\mu\text{m} - 1\text{ mm}$	1995–2011	1995–2011
Goldstone	$2 - 8\text{ mm}$	2001, 2005–2007	N/A
HUSIR 75E	$>5.5\text{ mm}$	1999–2003	2007*, 2009*, 2013–2015
HUSIR 20S	$>2\text{ cm}$	1999–2003	2015
HAX 75E	$>3\text{ cm}$	1999–2003	N/A
SSN Catalog	$>10\text{ cm (LEO)}$ $>1\text{ m (GEO)}$	1957–2007 (LEO) 1957–2006 (GEO)	1957–2014 (LEO) 1957–2015 (GEO)
MODEST	$>30\text{ cm}$	2004–2006	2004–2006, 2007–2009

* Datasets used for characterization of large breakups (Fengyun-1C, Iridium 33, and Cosmos 2251). Portions of datasets only around the time of the event were used.

Observational data available for OD population simulations, in particular for small-size debris, are statistical samplings from the near-Earth environment, collected under rather limited conditions. This type of data is always incomplete, subject to random sampling uncertainties, and normally containing an element of inherent variability. For example, surveys of impacts to returned surfaces, such as the windows and radiators of the U.S. Space Transportation System (STS, or the Space Shuttle), are very small sets of samples from the environment. Radar data in the staring (or “beam park”) mode is another example of a Poisson statistical sample. Thus, to develop an adequate representation of the OD environment, a statistical approach to scaling model populations based on data is critical. The following sections discuss the methods used for developing the ORDEM 3.1 model populations based on data from radar (Section 3.1), *in situ* (Section 3.2), and optical (Section 3.3) sources, each of which requires its own unique approach.

3.1 Radar-Based Populations

3.1.1 Reference Population

The initial population for large particles (greater than 1 mm) was generated from LEGEND using the years 1957–2014 as the historical inputs and repeating the launch traffic cycle of 2007–2014 every 8 years for the future propagation. Breakup fragments down to 1 mm in size were generated using a special version of the SSBM, by which material density distributions were applied to fragments smaller than 10 cm.

Like ORDEM 3.0, the material density distributions applied to breakup fragments smaller than 10 cm in ORDEM 3.1 were based on analysis of data from the Satellite Orbital Debris Characterization Impact Test (SOCIT), a set of hypervelocity impact tests at Arnold Engineering Development Center performed in 1991 (McKnight, *et al.*, 1995). The fourth and final test (termed SOCIT4) targeted a flight-ready, U.S. Transit navigation satellite, yielding collision fragments in the size regime of sub-millimeter through tens of centimeters. The spacecraft materials offered a view of a typical mid-20th century satellite structure. All three of the material density categories noted in Section 1.3.6 were represented in that test. The collection and measurement of the fragments was performed by Kaman Corp., and analysis was subsequently performed to determine relative percentages of density families for spacecraft and upper stages (Krisko, *et al.*, 2008). The resulting material density percentages of plastic (LD, $\rho = 1.4 \text{ g/cm}^3$), aluminum (MD, $\rho = 2.8 \text{ g/cm}^3$), and steel (HD, $\rho = 7.9 \text{ g/cm}^3$) for spacecraft as a function of size are shown in Figure 3-2.

The SOCIT4 ratio of MD to HD materials only is approximately 9 to 1, as shown in Figure 3-3. This result is very similar to analysis of impacts to the STS radiators and windows. As a result, fragmentations in LEGEND were modeled with material density distributions assumed to be 90% MD and 10% HD for rocket bodies, and according to fits of the percentages shown in Figure 3-2 for spacecraft. These ratios were applied to fragments from 1 mm to 10 cm. Fragments larger than 10 cm were all assigned as MD. Size-dependent distributions in A/m also were applied to fragments from 1 mm to 10 cm based on fits to the SOCIT4 data for each material density category.

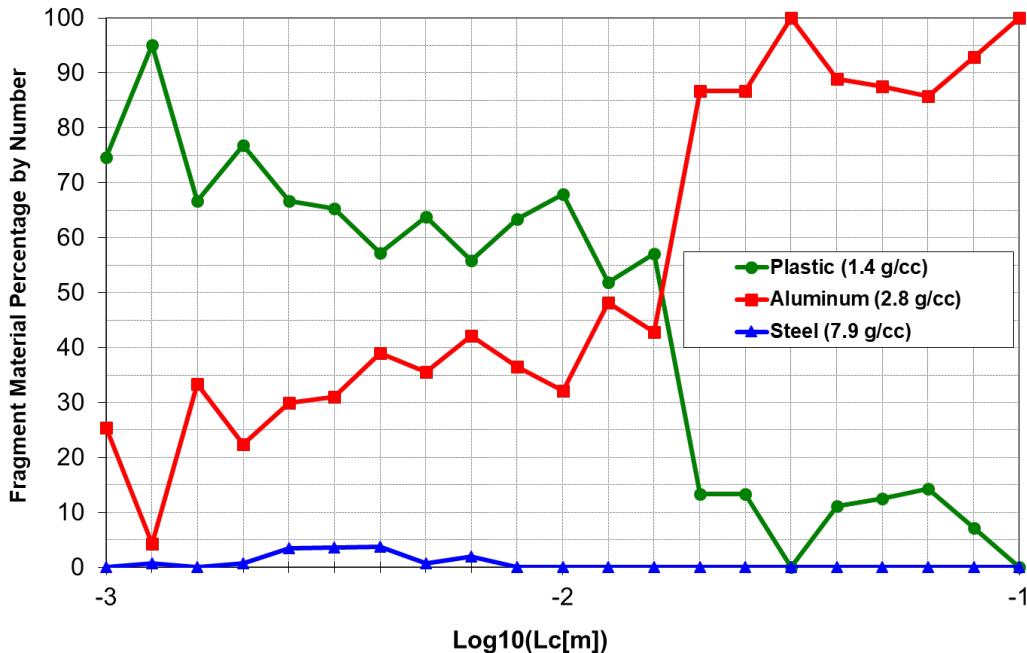


Figure 3-2. Relative density percentages for spacecraft plastic, aluminum, and steel fragments derived from the SOCIT4 data, as a function of debris size.

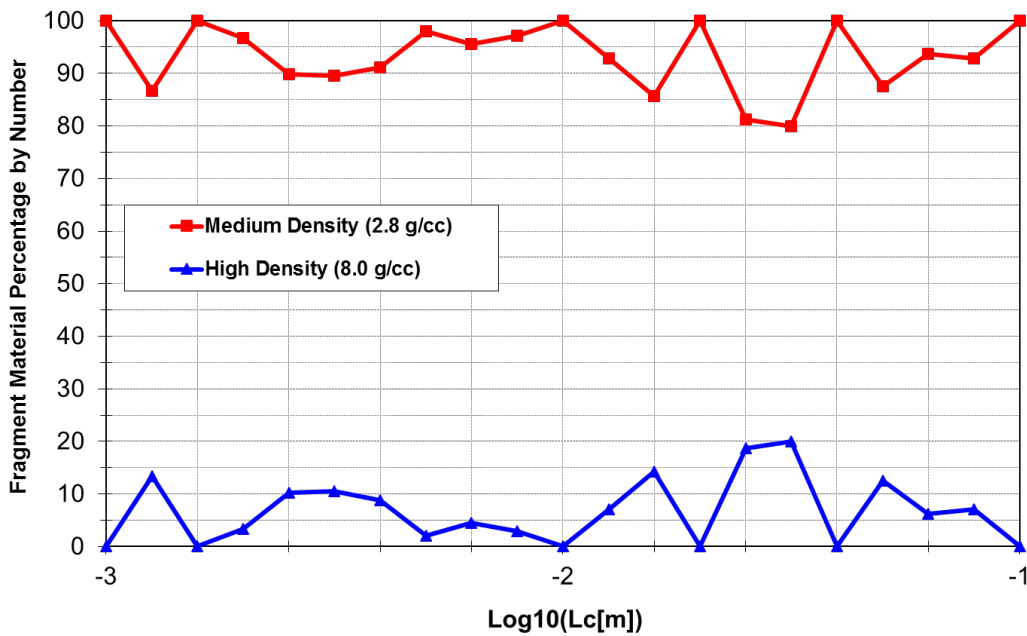


Figure 3-3. SOCIT4 MD and HD relative number percentages as a function of debris size. MD here includes aluminum, and HD includes steel and copper.

Results from 100 LEGEND MC runs were averaged per month for each year of the future projection. This initial population was scaled based on comparisons with radar data. Specific debris-generation events were removed from LEGEND and modeled independently, as discussed in Section 3.1.4.1.

3.1.2 Supporting Data

Measurements from the radars at the Massachusetts Institute of Technology's Lincoln Laboratory (MIT/LL) Space Surveillance Complex are used to cover the OD size regime in LEO from the limit of the SSN catalog at 10 cm down to approximately 5.5 mm. Recent data from the Haystack Ultrawideband Satellite Imaging Radar (HUSIR) – the first dataset from the upgraded Haystack radar – was used to develop the ORDEM 3.1 model for OD populations having a size of greater than approximately 5.5 mm in LEO. HUSIR data is collected on a U.S. Government fiscal year (FY) basis, and the data included for these population builds is from FY14 to FY15, corresponding to calendar year (CY) 2013–2015. Haystack underwent upgrades starting in FY10, which continued through the end of FY13, when the radar re-emerged as HUSIR. Observations from 2013–2015 were used to build the model, and data from 2016–2017 were used as a validation dataset. Additionally, Goldstone radar observations from 2016–2017 were used for ORDEM 3.1 validation purposes, with this latter dataset making observations down to a limiting size of approximately 3 mm. Details of the comparison between the ORDEM 3.1 model and these radar measurements are included in the ORDEM 3.1 Model Verification and Validation document (Sections 2.3 and 3.2).

HUSIR OD observations are conducted with the radar operated in a fixed beam mode rather than a typical tracking mode for the radar. Hence the radar, with its 0.058° 3-dB two-sided beamwidth at 10 GHz, is pointed at a fixed point in space with respect to the local topocentric coordinate system, and objects pass through the radar beam. The two pointing geometries for data collection considered in this report are 75° elevation or 15° from zenith, due East – referred to as 75E – and 20° elevation or 80° from zenith, due South – referred to as 20S. The majority of observations are from the 75E pointing geometry because of the increased orbital altitudes that are observed with this pointing. Fewer observations are typically conducted for the 20S pointing because of the longer slant range to debris in a given orbital altitude and the fact that radar performance falls off as the fourth power of the slant range from the radar to an object.

This sensitivity fall-off also leads to an altitude dependence of the OD size that may be observed by the radar. HUSIR is considered complete to approximately 5.5 mm at an orbital altitude of 1000 km and down to approximately 1 cm at 1600 km for the 75E pointing geometry. For the 20S pointing geometry, HUSIR is considered complete from approximately 2 cm out to 1000 km. Although observations from the 20S pointing are more limited, that dataset provides coverage of lower inclination bands that are not accessible with 75E pointing geometry. Data from 20S was only available from 2015 for use in ORDEM 3.1 development.

3.1.3 HUSIR Data Cleaning and Analysis

During ORDEM 3.1 population development, the process for converting raw data provided by the MIT/LL radars – HUSIR and Haystack Auxiliary (HAX) – was significantly refined. This process was developed from past experience with the dataset, coupled with new ODPO software processing tools (Debris Radar Automated Data Inspection System [DRADIS]) that give greater insight into the underlying radar data, to produce a consistent data product with quality assurance steps built into the process. A summary of the data cleaning and analysis process is shown in Figure 3-4.

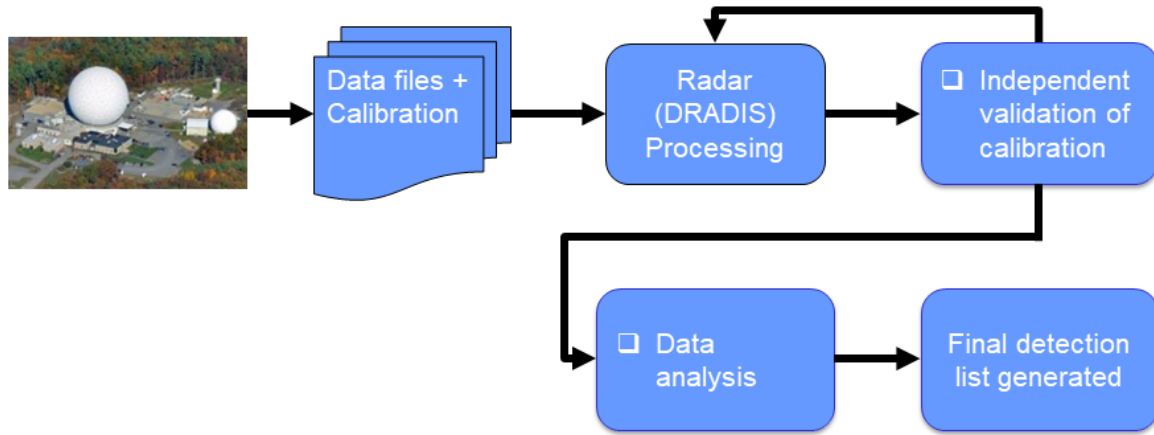


Figure 3-4. Radar data cleaning and analysis process – starting with data collected by the radars at MIT/LL through the delivery of final detection lists summarizing yearly OD observations.

Several of the steps in the process came about as analysis of the datasets revealed the presence of radio frequency interference (RFI), which has become more pronounced in recent years. The presence of RFI is relatively small because MIT/LL specifically screens the data for this, but it remains significant enough to warrant additional processing and removal. It typically represents less than 5 to 10 percent of the total detections on a yearly basis, and it has characteristics that make it relatively easy to identify through Range-Doppler images or by identification of outliers in Doppler time series. A comparison between an actual OD detection and RFI through Range-Doppler images is shown in Figure 3-5, and the identification of spurious Doppler – another typical characteristic of RFI – is shown in Figure 3-6.

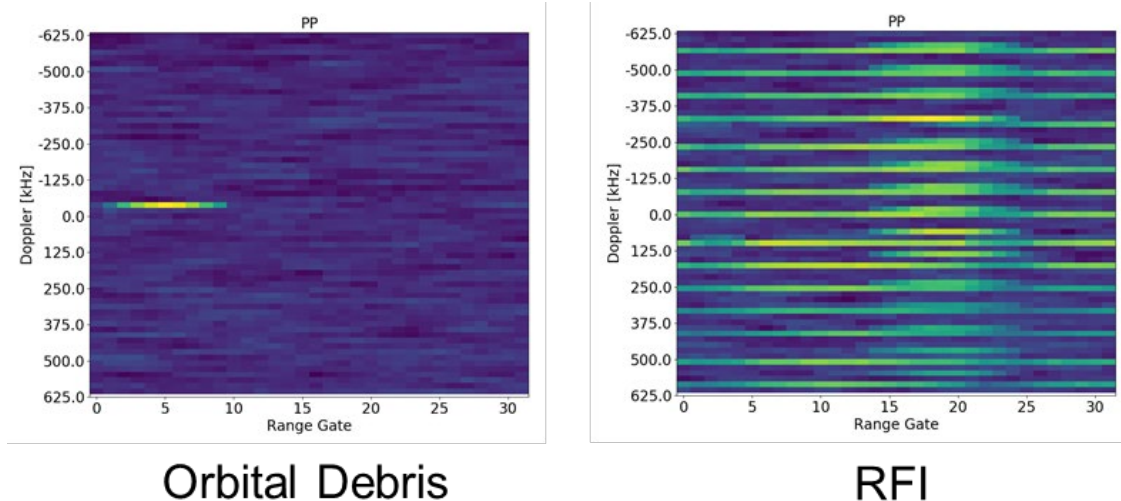


Figure 3-5. Range-Doppler Image for an OD detection (left) and a more obvious example of RFI (right).

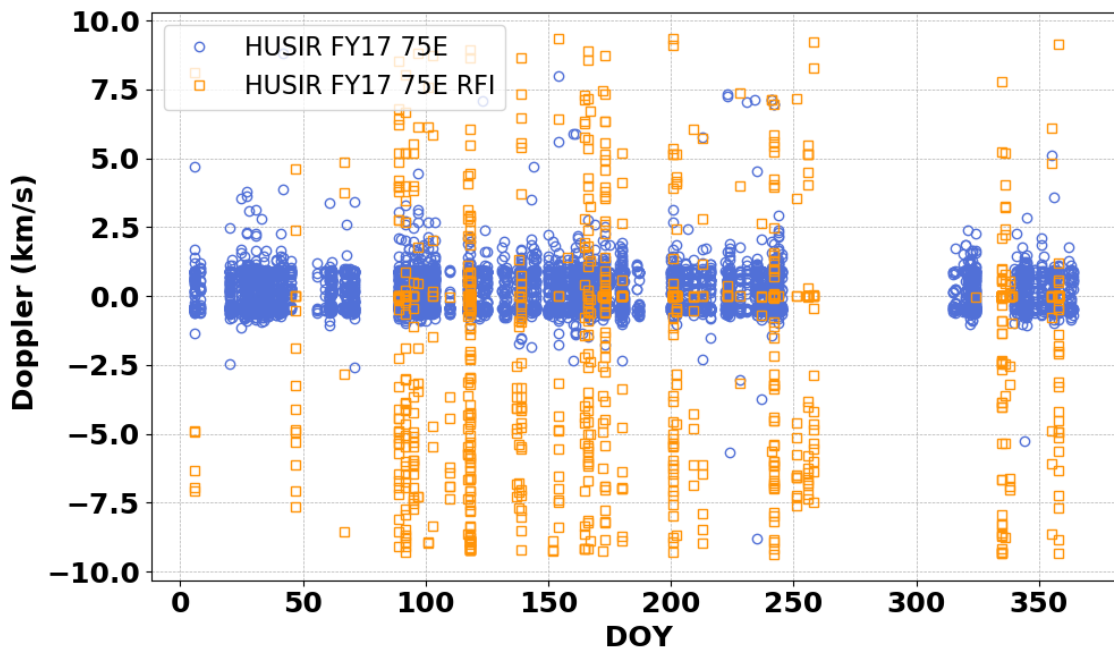


Figure 3-6. Identification of spurious Doppler, or range-rate, as a function of day of year. Large spreads in Doppler and increased detection rates over short time windows are another indication of RFI.

In addition to reviewing the dataset for RFI, several calibration steps subsequent to those provided by MIT/LL are conducted. The first calibration check independently verifies calibration data provided by MIT/LL using software tools developed by the ODPO. This independent calibration verification step provides quality assurance that the calibration used is correct and has successfully caught errors that were jointly resolved by NASA and the data provider. MIT/LL radars, and many other ground-based radar sites, are calibrated through the use of on-orbit calibration spheres. These spheres have well-known RCS values and orbital elements that are used to calibrate the RCS reported by the radar, the beamshape, and the monopulse channels, which are used to correct for a debris object's path through the beam. Beamshape data is reported by MIT/LL in spiral scan files, and RCS calibration data is reported in calibration sphere track files.

The second calibration check is conducted within the dataset by taking advantage of the unique properties of the NaK population. NaK is a population of electrically conducting spheres ranging in size from a few millimeters to a few centimeters. As a result, this population has well-defined characteristics with respect to the distribution of the RCS of the spherical particles and operating frequency of the radar, enabling it to be used for calibration purposes. For HUSIR, the peak in the statistical distribution is nominally near -35 dBsm. Figure 3-7 shows a comparison between a typical distribution of NaK for HUSIR collected on day of year (DOY) 150–160 in 2017, and an atypical distribution collected over DOY 250–260 of the same year. The shift in the peak of the distribution during the latter timeframe is indicative of an uncorrected bias in the radar data. Data collected during such time periods, which are relatively infrequent, are typically excluded from the dataset unless the source for that bias is identified and corrected. Additional properties of the NaK population, its source, and identification are discussed in Section 3.1.4.1.4.

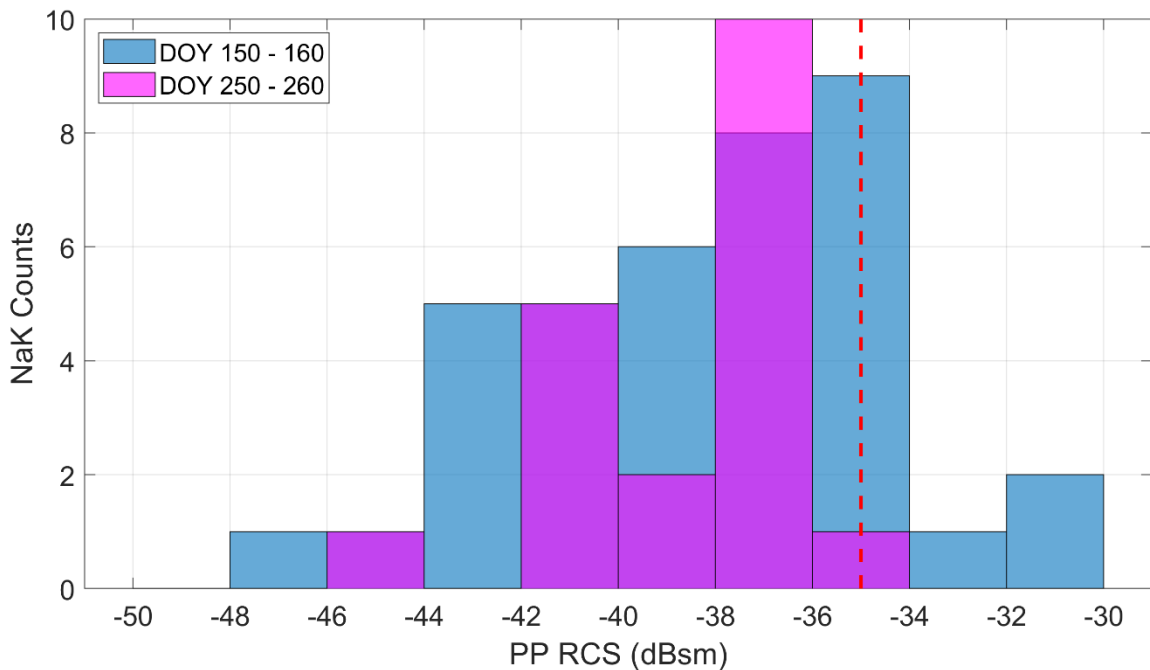


Figure 3-7. Comparison between NaK data collected on DOY 150–160 of FY17, representing a nominal NaK count distribution, and that collected over DOY 250–260, representing a data collection containing additional uncorrected bias. A vertical line at -35 dBsm, the distribution peak for HUSIR, is shown for reference.

A summary of the high-level steps involved in processing and analysis of the radar data, which results in detection lists for generating radar-based populations, is provided below.

1. MIT/LL radar data including debris, spiral scans to describe beam pattern, and calibration sphere track data files are sent to NASA. Additional information on the data contained within each of the debris and calibration files is covered in Section 3 of Murray, *et al.*, 2019.
2. Debris data files are batch processed using spiral scans on calibration objects.
3. Calibration sphere track files are processed to generate an independent calibration check for the data set, which are then compared to calibration files provided by MIT/LL.
4. Radar data is processed for all pointing geometries, and detections of OD are identified. Measurements made or derived for each detection include range, range-rate, RCS, time of observation, size estimation model (SEM) size, signal-to-noise ratio, inclination, altitude, and polarization information for each OD observation.
5. The dataset is reviewed for RFI using Range-Doppler Images.
6. Data is screened for spurious Doppler or range-rate.
7. An NaK calibration check is conducted.
8. Standard data representations are constructed for analysis of the year-over-year behavior of the OD populations and further analysis by subject matter experts (SME)
9. Data is manually reviewed by SMEs.
10. Finalized detection lists are placed under configuration management.

3.1.4 Scaling LEGEND Model Populations

A composite of the HUSIR 2013–2015 75E datasets was used to scale the initial LEGEND modeled populations. This composite dataset represents a weighted average of the individual 2013–2015 datasets, where the number of detections for a given size, range, etc. and for a given year was weighted by the number of observation hours for that year divided by the total observation hours across all three years. Special populations in LEO, including specific non-generic debris generation events (e.g., the Fengyun-1C breakup and the Iridium 33/Cosmos 2251 collision), other anomalous non-explosive events (SNAPSHOT, Transit), and the NaK population, were scaled individually and are discussed in the next section.

3.1.4.1 Special Populations in LEO

Several special debris-producing events have been identified independently of the debris background. These events are notable for their release mechanism, exceptionally detrimental effect on the environment, lack of obvious source, or notable differences from behavior predicted by the SSBM. For each of the LEO special populations incorporated into the ORDEM yearly population files, fragments were generated according to modeled rates and orbital families. Descriptions of these fragment populations are listed in Table 3-2. They include 10 custom breakup events, the Fengyun-1C (FY-1C) anti-satellite (ASAT) test, the Iridium 33/Cosmos 2251 accidental collision, shedding events from the SNAPSHOT and Transit vehicles, and the NaK droplets. The NaK droplets are the only special population identifiable in the ORDEM populations; all others are part of the combined debris environment. Each of these sources is discussed in Sections 3.1.4.1.1 through 3.1.4.1.4.

Table 3-2. LEO Special Debris Populations

Description	Estimated parent orbit (altitude, inclination) at event date	Debris event date
Ten custom breakup events	Varies	Varies
Chinese anti-satellite test (i.e., ASAT, FY-1C)	~850 km, 98.8°	11 Jan 2007
Iridium 33 / Cosmos 2251 collision	~790 km, 86.4° / ~790 km, 74.0°	10 Feb 2009
SNAPSHOT (1965-027A) satellite debris event	~1300 km, 90.3°	Multiple events and a single large event in 1984
Transit constellation satellite debris event	~1100 km, 90°	Deposited at end-of-mission + 20 years, per vehicle
NaK	900–1000 km (one at 700–760 km), ~65°	16 events, 1980–1988

3.1.4.1.1 Custom Breakups

The standard breakup model used in generating fragments for the initial LEGEND population does not capture the behavior of all breakup events in orbit. To compensate for this, specific breakup events were singled out and individually given a custom size-dependent scaling to match the available HUSIR 2013–2015 composite radar data. To aid in the modeling process, the composite radar data was separated into four natural inclination bands: 62°–68°, 68°–80°, 80°–93°, and 93°–108°. This breakdown into inclination bands allowed for the isolation of breakup events in the reference LEGEND population that appeared to require custom adjustments to better match the available radar data. Ten breakup events were specifically evident in this inclination breakdown and are indicated by yellow circles in Figure 3-8. For reference, the general locations of three major breakups of FY-1C, Iridium 33, and Cosmos 2251, discussed in Section 3.1.4.1.2, are also indicated by red circles. Breakup information for these 10 custom breakup events is shown in Table 3-3.

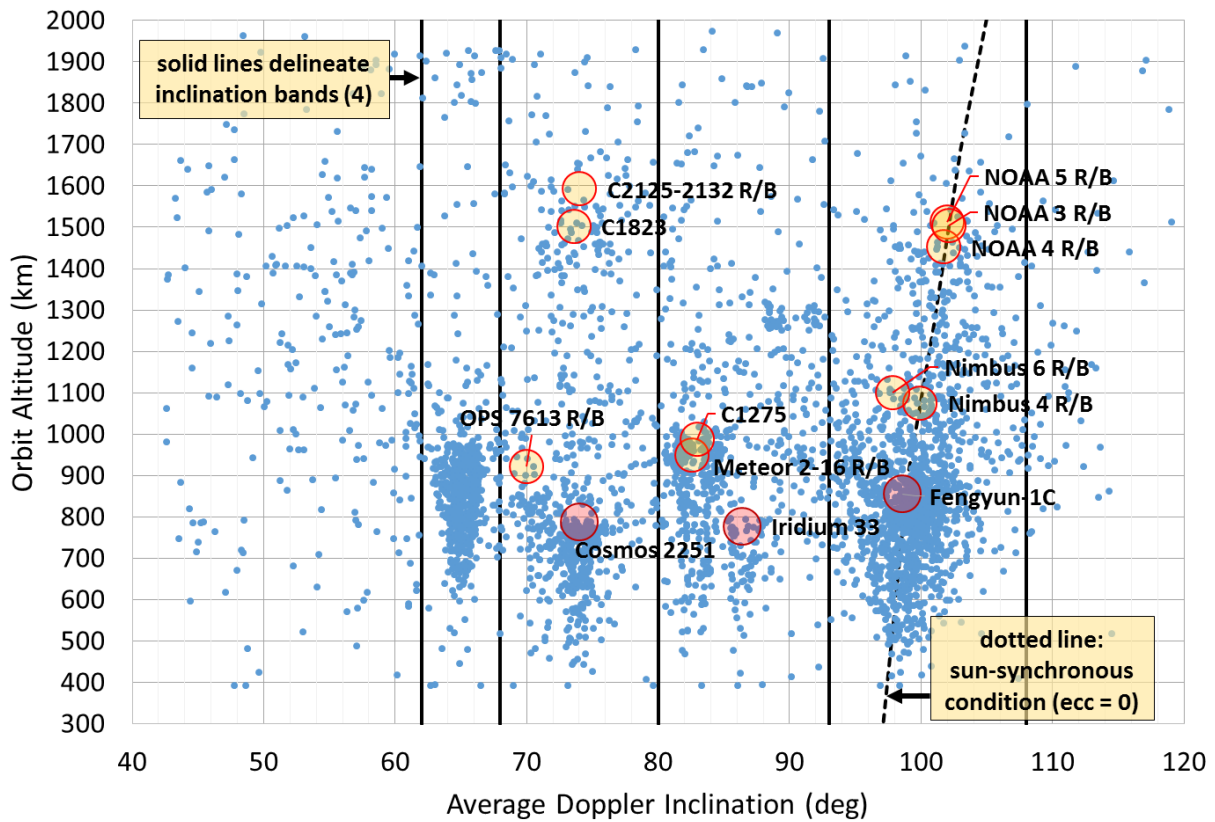


Figure 3-8. Altitude vs. inclination plot of the 2013–2015 HUSIR radar data. The data have a natural separation and were subsequently broken into five inclination bands. The modeled LEGEND population was then compared to the radar data by inclination band and individual breakup events in each band were adjusted to better match the available radar data.

Table 3-3. Ten breakups selected by inclination band that received a custom scaling factor.

International Designator	Mission Name	Fragmenting Object	Object Type	Breakup Date	Inclination (°)	Scaling Factor (SF)
1970-025C	NIMBUS 4	Agena D upper stage	Rocket body	17 Oct 1970	99.9	0.75
1976-077B	NOAA 5	Delta 1 2 nd stage	Rocket body	24 Dec 1977	102.0	1.25
1974-089D	NOAA 4	Delta 1 2 nd stage	Rocket Body	20 Aug 1975	101.7	1.10
1973-086B	NOAA 3	Delta 1 2 nd stage	Rocket Body	28 Dec 1973	102.1	0.45
1975-052B	NIMBUS 6	Delta 1 2 nd stage	Rocket Body	01 May 1991	97.8	1.10
1987-068B	METEOR 2-16	SL-14 <i>Tsiklon</i> 3 rd stage, 11K68	Rocket Body	15 Feb 1998	82.6	-0.15
1981-053A	COSMOS 1275	Parus, 11F627	Payload	24 Jul 1981	83.0	0.05
1991-009J	COSMOS 2125-32	SL-8 <i>Cosmos-3M</i> 2 nd stage, 11K65M	Rocket Body	5 Mar 1991	74.0	0.25
1987-020A	COSMOS 1823	Musson, 11F666	Payload	17 Dec 1987	73.6	0.25
1969-082AB	OPS 7613	Agena D upper stage	Rocket Body	04 Oct 1969	70.0	10.0

To find the custom scaling factors for the breakup events, the initial LEGEND populations for 2014 were broken into the same inclination bands as the radar data. Simulated radar data were then produced from

the initial LEGEND population via a MC simulation to simulate the expected detection rate that HUSIR would obtain for the model. The simulated radar data were then compared with the actual radar data in terms of detection rate vs. altitude, and a size-dependent scale factor was applied to fit the model's simulated radar detection rate to the HUSIR detection rate. The breakups were scaled based on the characteristic length L_c of the parent body according to the equation

$$W = W_0 \left(\frac{L_c}{0.1} \right)^{SF} \quad 3.1-1$$

where W_0 is the initial weight of a fragment, as given by the initial LEGEND simulation, SF is the scale factor given in Table 3-3, and W is the final weight applied to the fragment. This scaling explicitly changed the number of debris objects generated by each custom breakup event. The form of this equation was chosen such that the weight of 10 cm (cataloged) objects would be unchanged, but the slope of the cumulative size curve for objects less than 10 cm would be raised or lowered to better match the radar data for debris as small as approximately 5.5 mm. Since the version of LEGEND used to generate the initial reference population used customized scale factors to match the number of cataloged objects, the combination of that scale factor and the custom one applied for the 10 breakups served to both shift the standard power law curve up and down as well as change its slope below 10 cm. An example of three custom scaled breakups in the 68° – 80° inclination band is shown in Figure 3-9. The Cosmos 2251 debris, also in this inclination band, is shown for reference.

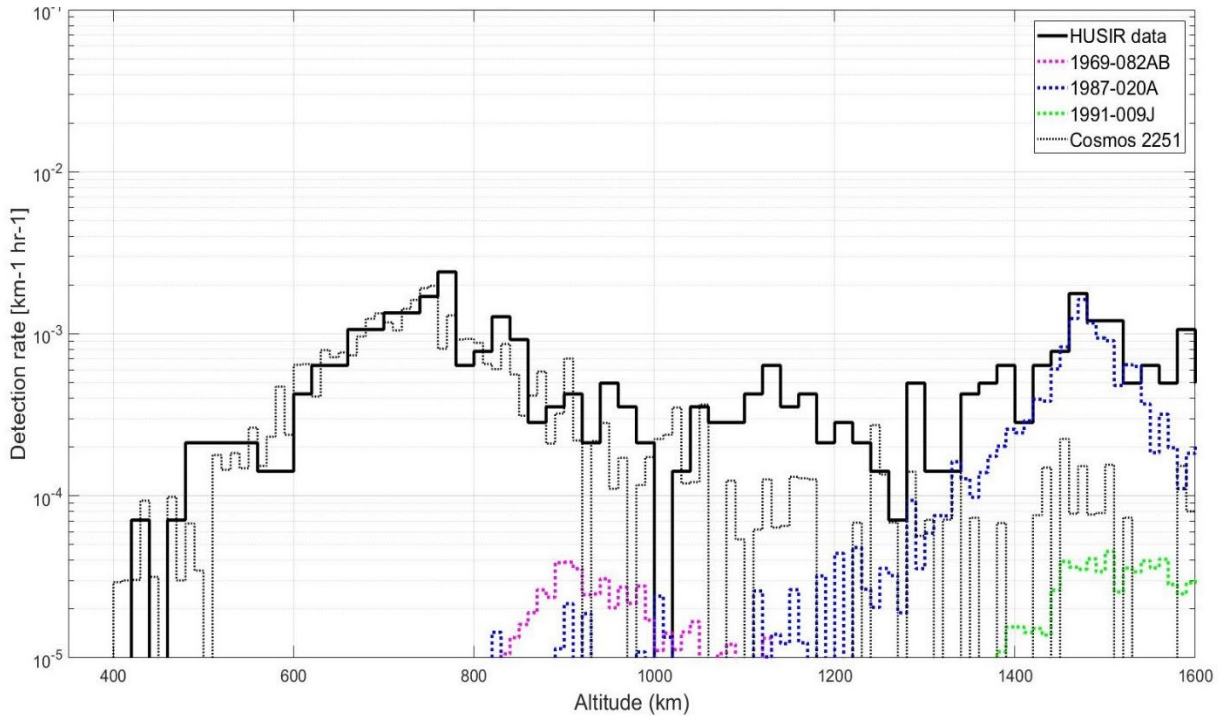


Figure 3-9. The detection rate of > 1 cm objects in the 68° – 80° inclination band for the HUSIR data and the three breakups in this inclination band after custom scale factors were applied. This inclination band also includes the Cosmos 2251 debris, which dominates the debris population at lower altitudes and is shown for reference.

3.1.4.1.2 Major Collisions: FY-1C, Iridium 33, and Cosmos 2251

Two major collision events have occurred on-orbit: the FY-1C ASAT test and the accidental collision between Iridium 33 and Cosmos 2251. The FY-1C meteorological spacecraft (International Designator 1999-025A, SSN Number 25730) was launched on 10 May 1999. On 11 January 2007, it was destroyed through collision with a ground-launched, sub-orbital interceptor in an ASAT test conducted by the Chinese government. The resulting debris cloud, measured by the number of trackable fragments, was the largest in the history of spaceflight (Stansbery, *et al.*, 2008). As compared to the SSBM, the distribution of A/m for the cataloged FY-1C fragments shows an excess of fragments with A/m values greater than approximately 0.3 m²/kg. By design, FY-1C was covered with approximately 13 m² of Multi-Layer Insulation (MLI) and equipped with two larger solar panels (6 m² each). It is very likely that the excess of fragments with A/m values above approximately 0.3 m²/kg consists of composite material, solar panel, and MLI pieces (Liou, *et al.*, 2013).

The accidental collision of the defunct Cosmos 2251 spacecraft (International Designator 1993-036A, SSN Number 22675) with the operational Iridium 33 spacecraft (International Designator 1997-051C, SSN Number 24946) on 10 February 2009 was the first major collision of an inoperable satellite with a functional spacecraft. Cosmos 2251 was an older satellite while Iridium 33 was relatively modern. Analysis of the fragments cataloged by the SSN has indicated that Cosmos 2251 fragments are well-described by the NASA SSBM, but noticeable discrepancies exist between the model predictions and the observation data for the Iridium 33 spacecraft. Lightweight composite materials were extensively used in the construction of the Iridium vehicles, and each vehicle was equipped with two solar panels (3.9 m² each). This could be a reason behind the discrepancy between the model prediction and the data (Liou, *et al.*, 2013).

Special data were collected using the Haystack sensor in 2007 and 2009, around the time of the FY-1C and Iridium 33/Cosmos 2251 breakup events. These special data were reprocessed using DRADIS for reassessment of these breakups clouds for ORDEM 3.1 development. In particular, the data calibration was checked using the NaK method (Section 3.1.4.1.4), and the estimated size distribution was recalculated. In addition, the breakups were re-examined and breakup conditions were adjusted to better match the orbits of tracked debris, including computing new momentum transfer values and new delta-velocity distributions. Table 3-4 provides details on the adjusted scalings for these breakup clouds, in terms of overall number based on the initial Haystack data and delta-velocity based on orbits of the cataloged fragments.

Table 3-4. Overall number and delta-velocity scalings for the three major breakup clouds (ASAT, Iridium 33, and Cosmos 2251).

Spacecraft	Overall number scaling based on initial Haystack data	Delta-velocity scaling based on catalog	Delta-v along track	Delta-v cross track (v x r)	Delta-v radial
ASAT	3.2	2.05	-1 m/s	-52 m/s	+33 m/s
Iridium 33	3.0	0.581	+7 m/s	+10 m/s	+14 m/s
Cosmos 2251	1.5	1.28	-17 m/s	+10 m/s	+14 m/s

Additionally, comparisons were made between the modeled breakup clouds and the HUSIR 2013–2015 composite data to characterize the smaller fragments from these major clouds. The 2013–2015 HUSIR data represents the state of the clouds after nearly a full solar cycle, and analysis showed that some of the clouds (especially Iridium 33) were decaying out of the environment much faster than anticipated. Thus, size-dependent A/m distribution adjustments were applied to reflect the higher drag rates and match the altitude distribution of the measured clouds. The enhanced A/m distributions as a function of characteristic length are shown in Figure 3-10.

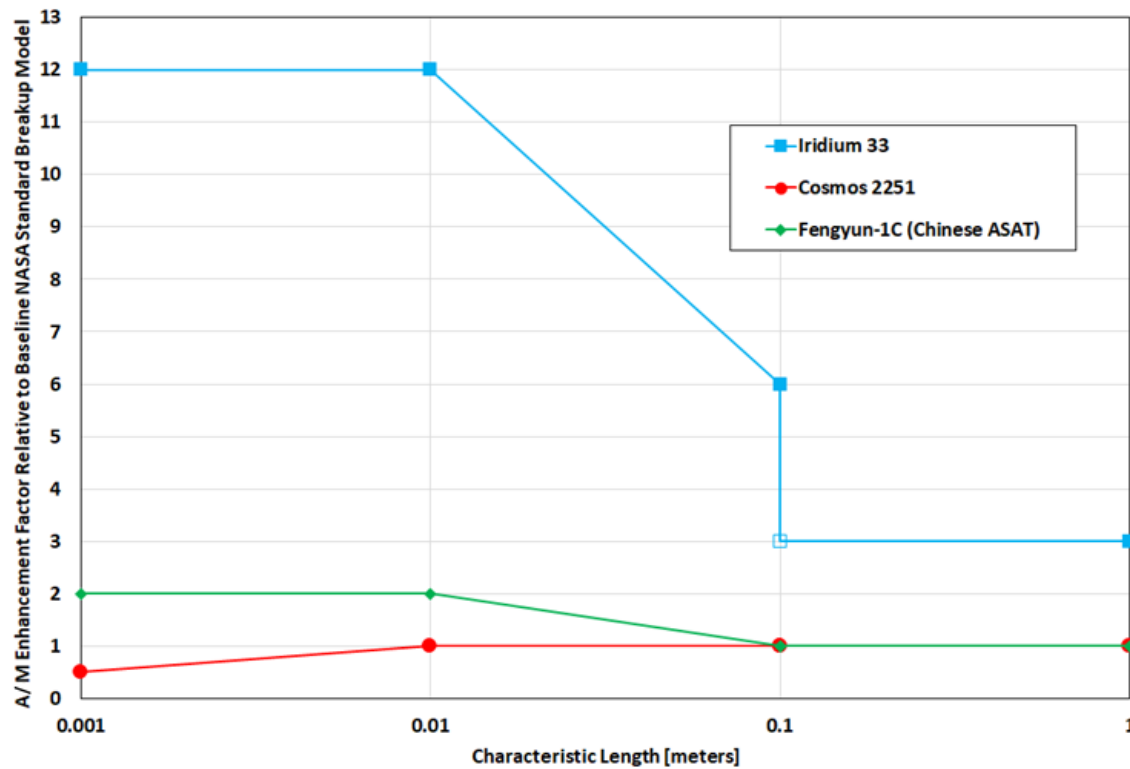


Figure 3-10. Empirical model enhancements to the modeled A/m ratio of fragments as a function of characteristic length for the three major breakup clouds (FY-1C ASAT, Iridium 33, and Cosmos 2251).

Figure 3-11 shows a comparison of inclination distribution for the cataloged FY-1C ASAT fragments, the initial modeled breakup cloud using the SSBM, and the adjusted breakup cloud after all scalings and adjustments were applied. Clearly, the adjusted, modeled breakup cloud provides a better match to the catalog data in terms of the distribution shape.

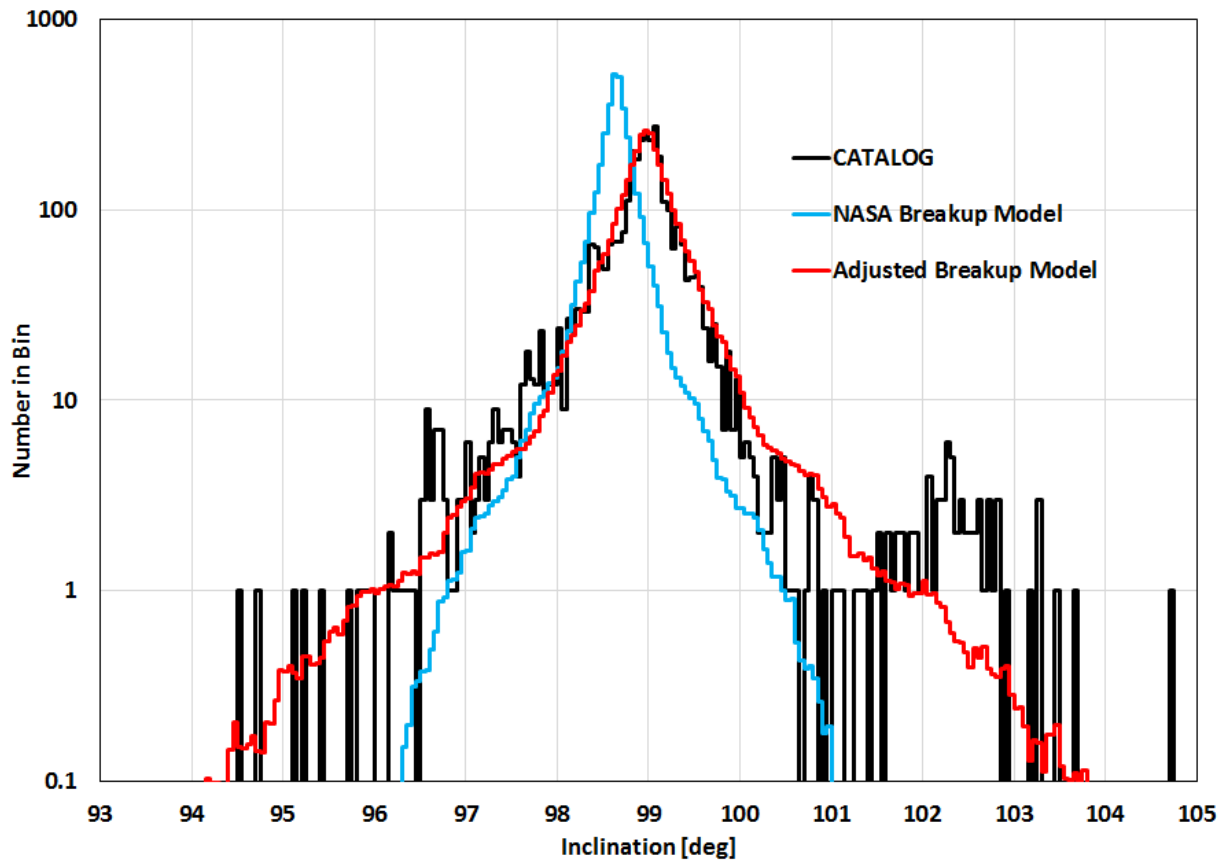


Figure 3-11. Comparison of the inclination distribution for the FY-1C ASAT breakup cloud between the SSN catalog (based on the earliest-available TLE for each debris object), the NASA SSBM, and the adjusted breakup model.

The modeled breakup clouds were also transformed into simulated radar detections for comparison to the HUSIR data. Figure 3-12 through Figure 3-14 show the simulated detection rate vs. altitude, to a limiting size of 1 cm, for the ASAT, Iridium 33, and Cosmos 2251 breakup clouds, respectively. Comparisons are shown between the modeled clouds from ORDEM 3.0 and ORDEM 3.1, and to the HUSIR 75E 2013–2015 data within the inclination band corresponding to each breakup cloud. Note that, in each of these figures, the ORDEM 3.1 curve is for the specific breakup cloud only, whereas the black HUSIR data curve is for all objects detected in that inclination band. Ideally, the predicted model cloud should be less than or equal to the HUSIR data at all altitudes because other sources contribute debris in these inclination bands. However, in altitude bands where the detection rate is low (and the sampling error high), this criterion may not be strictly true (e.g., the 550–600 km altitude bin for the Cosmos 2251 cloud, see Figure 3-14). Note that it was especially difficult to match the Iridium 33 cloud at low altitudes (see Figure 3-13), as a significant fraction of the debris had already decayed from the environment compared to initial model predictions.

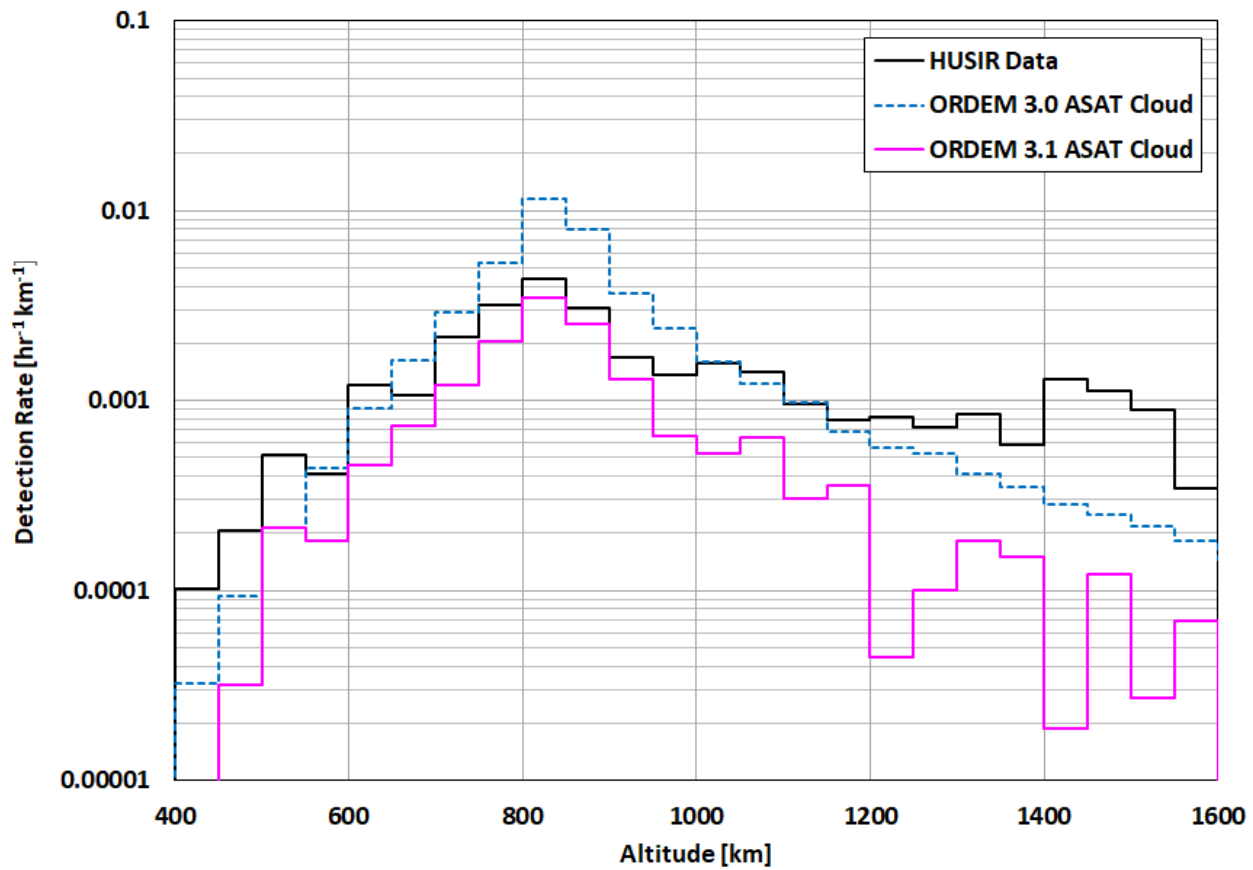


Figure 3-12. Comparison of the detection rate vs. altitude, to a limiting size of 1 cm, for the FY-1C ASAT breakup cloud between ORDEM 3.0 and ORDEM 3.1, and to the HUSIR 75E 2013–2015 data within the inclination band corresponding to the FY-1C ASAT cloud.

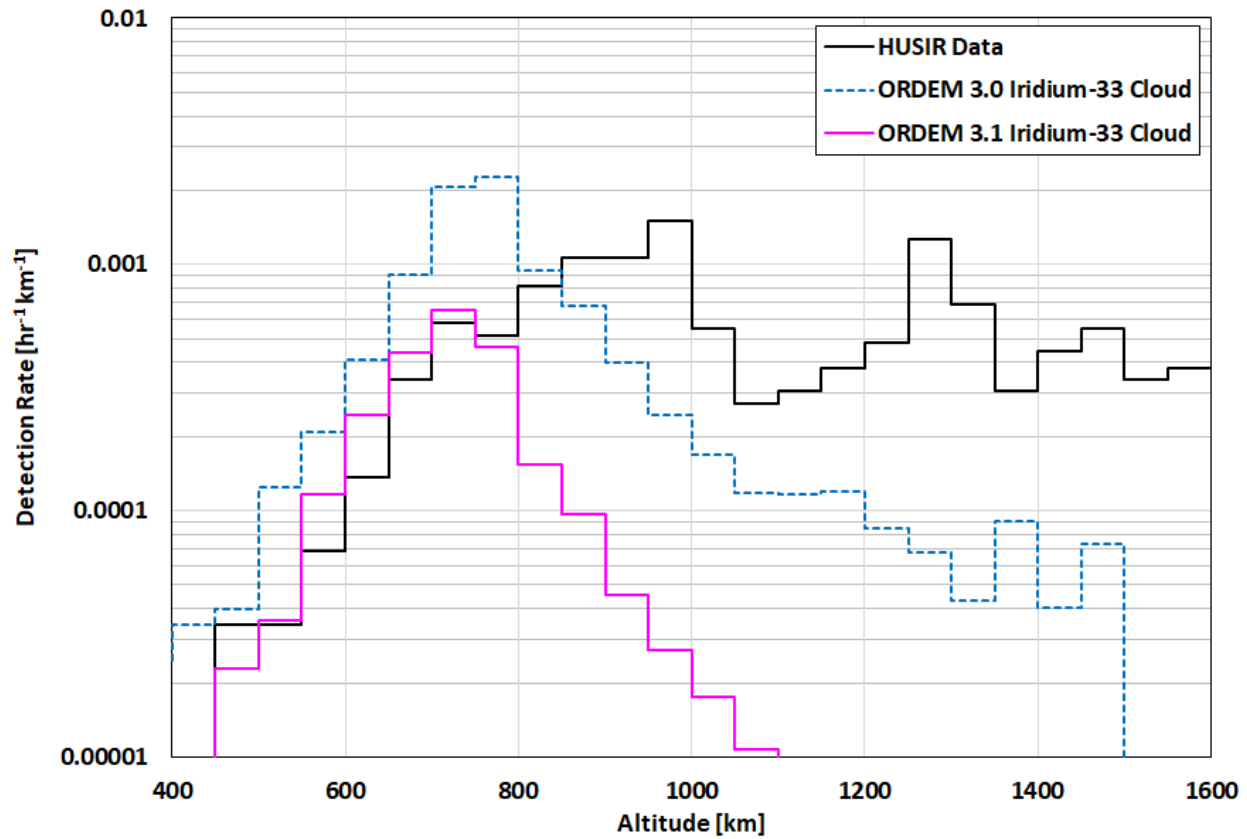


Figure 3-13. Comparison of the detection rate vs. altitude, to a limiting size of 1 cm, for the Iridium 33 breakup cloud between ORDEM 3.0 and ORDEM 3.1, and to the HUSIR 75E 2013–2015 data within the inclination band corresponding to the Iridium 33 cloud.

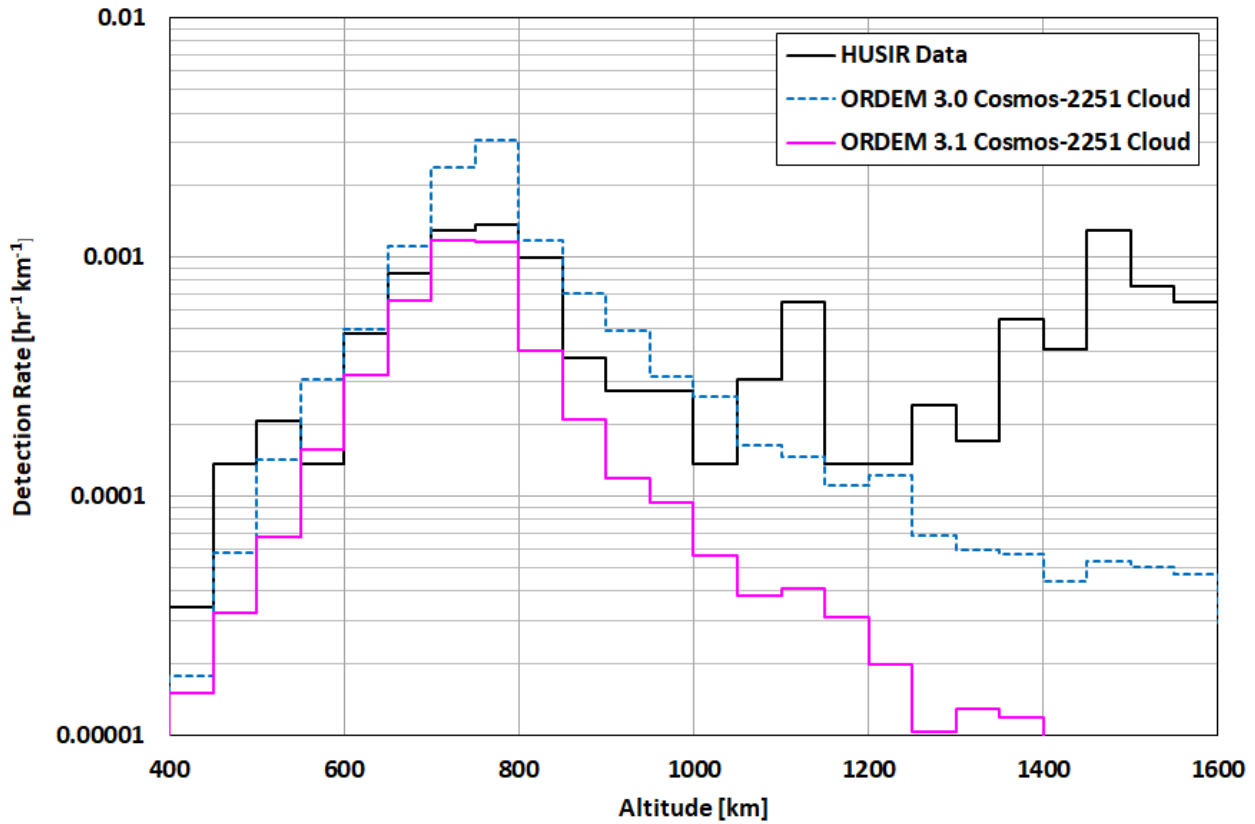


Figure 3-14. Comparison of the detection rate vs. altitude, to a limiting size of 1 cm, for the Cosmos 2251 breakup cloud between ORDEM 3.0 and ORDEM 3.1, and to the HUSIR 75E 2013–2015 data within the inclination band corresponding to the Cosmos 2251 cloud.

3.1.4.1.3 SNAPSHOT/Transit

Previous analysis of the Haystack data revealed evidence of a near-circular debris ring in a polar orbit with altitudes ranging from 1270 km to 1330 km. This debris ring appears twice each day to the radar, corresponding to viewing two portions of the ring. Most of the debris ring candidates are smaller than 4 cm. The altitude, inclination, and radar observation times of the debris ring correspond to the orbit plane of the nuclear powered SNAPSHOT satellite (International Designator 1965-027A; SSN Number 1314, common name OPS 4682). The SNAPSHOT satellite is well known for shedding pieces of debris with 158 cataloged debris pieces as of 4 July 2018 (Anz-Meador, *et al.*, 2018). At a slightly lower altitude, a second debris ring was associated with spacecraft of the Transit navigation satellite system. The Transit dataset includes several Transit-class spacecraft that were involved in anomalous debris-producing events at ~1100 km as early as the 1960s and 1970s. Examination of anomalous events did not associate the Transit rocket boosters with debris production events. Details of the anomalous events for these satellites are shown in Table 3-5. Note that the entry for Transit, Transit 5B-6, is a representative example of the 10 known Transit constellation anomalous events (Anz-Meador, *et al.*, 2018).

Table 3-5. Anomalous event dates for the SNAPSHOT and Transit satellites.

International Designator	Name	Launch Date	First Event Date	Inclination (°)
1965-027A	OPS 4682 (SNAPSHOT)	3 Apr 1965	1 Nov 1979	90.3
1965-048A	OPS 8480 (Transit 5B-6)	24 Jun 1965	Aug 1980	89.9

The SNAPSHOT/Transit events are anomalous in that they do not demonstrate breakup behavior consistent with explosive events. Instead, they appear to be slowly breaking up and shedding off mass over time. To model these events, it was assumed that some percentage of the mass of the original satellites is shed each year, with each shedding event following the NASA SSBM power law distribution for fragmentation size. Separation velocity relative to the parent body was assumed to have a maximum of 5 m/s.

For ORDEM 3.1, these events in the Sun-synchronous inclination band were initially scaled by a flat weighting factor because the SSBM size distribution assumed for each shedding event appeared to be undercounting the contributions of these events to the modeled environment at each size by a similar amount. Therefore, rather than change the slope of the distribution of particles at a given size as generated by the breakup model, each curve was given an initial flat scaling factor to roughly match the radar data. Then, a Bayesian fitting method was applied to these clouds to statistically fit them to the radar data, as discussed in Section 3.1.4.2.

3.1.4.1.4 NaK

The NaK population was originally identified in the early 1990s in Goldstone and Haystack radar data. It represented a population of electrically conducting spheres from a few millimeters in size to a few centimeters, all in 65° inclination, near-circular orbits, mostly between the altitudes of 850 and 1000 km. The spherical nature was deduced from the polarization of the radar returns, which indicated a strong principal polarization (PP) and a very weak orthogonal polarization (OP). Further work by MIT/LL succeeded in cataloging a few of these objects, determining their ballistic coefficients, and measuring their optical properties. All the evidence pointed to electrically conducting spheres, with densities consistent with the NaK liquid metal coolant used in the Soviet Radar Ocean Reconnaissance SATellite (RORSAT) reactors, which had nuclear cores jettisoned into these orbits in the 1980s. In the microgravity of orbit, the droplets formed into individual spheres. In addition to the RORSAT source, “Topaz” reactors (aboard Cosmos 1818 and 1867) also have been noted to produce NaK droplets in their operational orbits, though they did not separate reactor cores.

Previous modeling had assumed that the deposition of the NaK took place only at the jettisoned times, but the newest HUSIR data encompassed another solar cycle from the radar data used in the previous ORDEM model, indicating how the droplets have decayed over the latest solar maximum. The newest data still showed a significant contribution of small (< 1 cm) droplets at the highest altitudes, where atmospheric drag should have removed them by now, as seen in Figure 3-15. This indicates that there is some sort of continual source for these droplets. Likely candidate(s) are RORSATs that did not jettison reactor cores. Additionally, recent “Topaz” reactor spacecraft anomalous debris events may correspond to ongoing sporadic leakage events. Because of these apparent continual sources, for ORDEM 3.1, the NaK model was represented as a steady state over the future projections of the model. Until further analysis reveals the causes and details of ongoing production events, this is a reasonable conjecture.

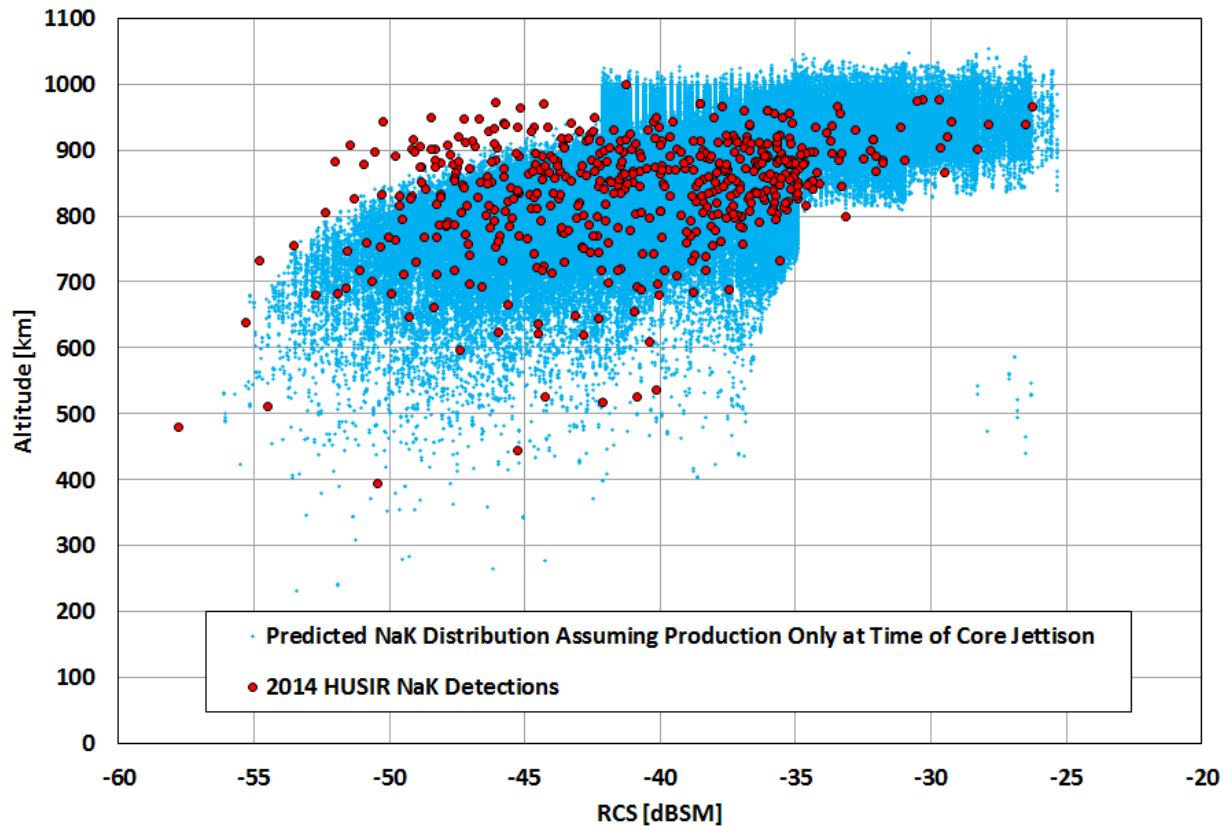


Figure 3-15. NaK distribution predicted for 2014 by assuming production only at time of core jettison, compared to the NaK detections from the 2014 HUSIR 75E data.

In order to construct the NaK population, a reference NaK model for a given year was simply replicated for all years. The easiest approximation is to model the NaK population as having a single inclination (65°), a single eccentricity (circular orbits), and an empirical distribution in altitude and size.

Ascertaining the sizes of individual NaK particles is complicated by the fact that, as spheres, certain RCS values can correspond to up to three different sizes based on the SEM (see Figure 3-16). This means that for certain RCS values, the size determination can be ambiguous. Fortunately, the HUSIR data sees objects well into the Rayleigh regime of the size-RCS curve, where the object size is much smaller than the radar wavelength and the RCS-to-size conversion is less ambiguous.

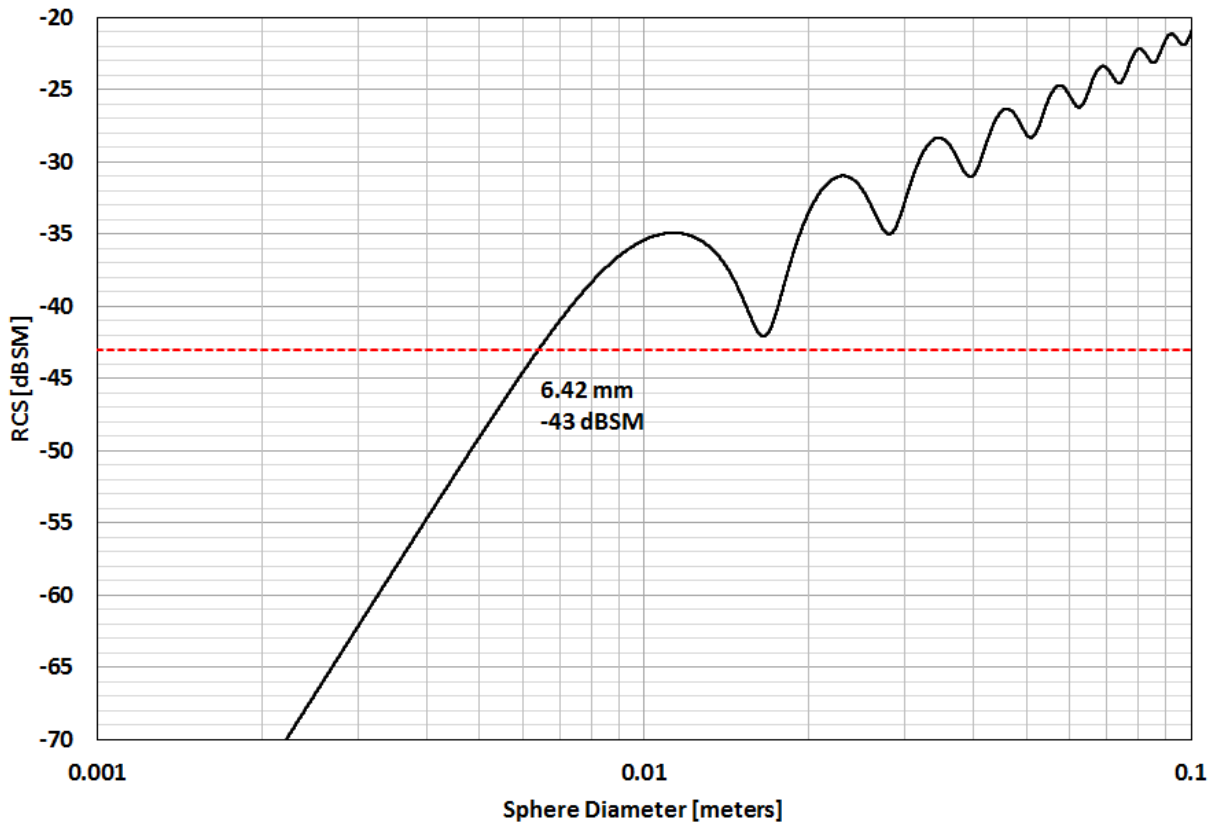


Figure 3-16. The black curve shows the theoretical RCS value for a given conducting sphere diameter (given the HUSIR 3 cm wavelength). The red dashed line is for an RCS of -43 dBISM, corresponding to a sphere 6.42 mm in diameter. For HUSIR detections of objects with RCS values above about -43 dBISM, there is an ambiguity in determining the size of the object for a given RCS. Counting the number of detections with RCS above -43 dBISM gives a good estimate of the total number of spheres larger than 6.42 mm in diameter.

Choosing NaK particles (filtered out of HUSIR data based on a high PP/OP ratio, altitudes below 1000 km, and inclinations near 65°) with RCS greater than -43 dB square meters (dBISM) provides a representative accurate count of all NaK particles detected larger than approximately 6.42 mm. Previous work (Foster, 2003) estimated the overall size distribution of the NaK population by fitting a functional form to the size curve and predicting the corresponding RCS distribution. The size distribution was varied until the computed RCS curve matched the data. This size distribution was used to scale the 6.42 mm populations at the ORDEM reference sizes and is shown in Table 3-6.

Each NaK object seen represents some number of unseen NaK objects. To determine a statistical estimate of the NaK population at a particular altitude, the detection rate for a single object in that orbit (inclination 65°, circular, with altitude given by the altitude of detection) was first determined. The probability of seeing such a single object was found by multiplying the detection rate by the observation time. Each object seen was then weighted by the inverse of its detection probability, and the resulting sum over all NaK objects detected in a particular altitude bin provided a statistical estimate of the NaK population in that bin.

Table 3-6. Model ratio of the NaK population at the ORDEM fiducial sizes to the empirical size distribution at 6.42 mm, as scaled to the total number of objects counted with size 6.42 mm.

NaK Sphere Reference Size	Model Ratio of Empirical NaK Population Fit to Measured 6.42 mm NaK Population
3.16 cm	0.0244
1.0 cm	0.532
3.16 mm	2.30
1.0 mm	8.25

3.1.4.2 Bayesian Approach Applied to ORDEM Populations

The Bayesian procedure was devised during the development of ORDEM 3.0 and is summarized here. This approach is generally applicable to count-data-based OD-population estimations (Xu, *et al.*, 2005, 2009, 2010a,b; Xu, 2006) and its practical implementation in OD-population estimations was tested and validated in different ways during the development of ORDEM 3.0 (Stansbery, *et al.*, 2015; Xu, *et al.*, 2009). The Bayesian approach demands, besides data, prior information on all the data-related OD populations, *i.e.*, reference (or initial) models for all component populations that the data involves. Given the data, the Bayesian process first searches for best estimates of model parameters that link model populations with data and are appropriately defined as desired. The reference model populations are then refined (or updated) in terms of the best estimated model parameters. In Bayesian terminology, observed results change *a priori* into a *posterior* distribution that characterizes the related OD populations. The fidelity of the outcomes from such statistical estimations depends on the quality and quantity of the available data and the credibility of the input reference component populations.

The Bayesian approach was used to provide an overall inspection of the match between the radar-based candidate model populations and the HUSIR data for sizes ≥ 5.62 mm. The candidate model populations included the initial LEGEND population with scaling factors applied to the 10 custom breakup events and all the special ASAT, Iridium 33, Cosmos 2251, SNAPSHOT, and Transit clouds. Because NaK detections in the radar data can be identified mainly from measured polarizations and are separable from other detections, the special NaK populations were modeled independently (see Section 3.1.4.1.4) and are thus excluded here. The term “NoNaK” appearing in the following text means that NaK populations or detections were not included. The overall inspection served to investigate if possible further refinements were needed for the candidate ORDEM 3.1 model populations from the perspective of the Bayesian statistics. Uncertainties on population estimates are also a by-product of this analysis.

The Bayesian inference process scales, when necessary, reference model populations at discrete quarter-decade (quarters in \log_{10} space) sizes from ≥ 1 m, ≥ 56.2 cm, ..., down to ≥ 5.62 mm step-by-step, seeking the best possible match of model predictions with data. The model population re-estimation process starts with large-size (≥ 10 cm) populations, and model parameters were estimated to best match the radar data in the 2-dimensional space of range vs. range rate. Adjustments for subsequently smaller sizes were made only to the un-adjusted size ranges. For example, to refine ≥ 5.62 cm reference populations, the subgroup of 5.62–10 cm objects was adjusted. Similarly, for the ≥ 3.16 cm populations, only the 3.16–5.62 cm subgroup was adjusted. To avoid discontinuity at the discrete, benchmark size points, actual adjustment factors were interpolated from the model parameters estimated respectively for the populations in the smaller and larger size ranges (*e.g.*, the model parameters for sizes between 5.62 cm and 10 cm were interpolated in terms of the two estimates for the ≥ 5.62 cm and ≥ 10 cm populations to provide a continuous result). Normally, the Bayesian process requires iteration until all the

model parameters converge close to one. In general, noticeable improvements on the model-to-data matching are achieved at each iteration. Model-to-data comparisons, such as for flux, RCS, detection-probability, object-size and other distributions, were scrutinized after each iteration to better understand the model-to-data agreement and also the credibility of the reference populations, as shown in Stansbery, *et al.*, 2015.

In the re-estimation process, orbits in the model populations were divided into three subgroups: (1) inclination $\geq 40^\circ$ and perigee height < 1350 km, (2) inclination $\geq 40^\circ$ and perigee height ≥ 1350 km, and (3) inclination $< 40^\circ$. The division was based mainly on the limitations in the available radar data associated with radar viewing geometry. When HUSIR points to 75° elevation and East, objects with inclination less than approximately 40° will not be seen by the radar. To better fit radar data at high altitudes, orbits of $\geq 40^\circ$ inclinations were divided further based on perigee height below or above 1350 km. The group of $< 40^\circ$ inclination was not further divided, mainly because the only radar data available for this group is the 20°S data set of the year 2015, which had no detections at altitudes above 1350 km. As discussed in Section 3.1.2, HUSIR's ability to detect small-size targets at high altitudes is reduced as its detection efficiency drops at large distance. The Bayesian statistical approach in the current implementation does not include a correction for this issue, and radar detections of altitudes under $\sim 1,000$ km play a dominant role in the estimation of 5.62–10 mm populations.

While the candidate model populations were all developed separately, as discussed above in Sections 3.1.1 and 3.1.4.1, no specific criterion has been established to enable filtering radar detections corresponding to a specific component population (e.g., ASAT) from the radar data. As a result, the model parameters for all the NoNaK component reference populations (*i.e.*, LEGEND with the 10 custom breakup scalings and the special ASAT, Iridium-Cosmos, SNAPSHOT, and Transit clouds) were all estimated simultaneously in the Bayesian process. Thus, the estimated model parameters for an individual component population are coupled with those of some of the other component populations.

Overall results of the Bayesian analysis of the candidate model populations suggested that all the preliminary, candidate NoNaK component ≥ 5.62 cm populations needed some minor, further adjustments in underlying structure (by dividing the populations in terms of eccentricity, inclination, *etc.*). Final radar-based model adjustments are discussed in Section 3.1.4.3. However, the special SNAPSHOT and Transit models seemed to be coupled largely with the related background LEGEND population. Thus, the refined SNAPSHOT and Transit models were used for ORDEM 3.1 population development. Table 3-7 presents the model parameters from the initial iteration for the special SNAPSHOT and Transit clouds, obtained as a weighted average across all years of available HUSIR data. Note that the SNAPSHOT and Transit models include only objects less than 10 cm. “N/A” shown in the table for Transit objects > 5.62 cm is because, under certain circumstances, no estimation is obtained for some desired model parameters because of a low detection efficiency of radar, limitations of a radar viewing geometry, or low probability of the objects being detectable in the specific areas.

Table 3-7. Weighted-average model parameters estimated in the initial iteration of the Bayesian scheme from HUSIR 75E data of CY2013–15 for the special SNAPSHOT and Transit clouds.

Object Size	Weighted Avg., SNAPSHOT	Weighted Avg., Transit
> 5.62 mm	$0.265 \pm 15.4\%$	$0.275 \pm 12.0\%$
> 1 cm	$0.352 \pm 21.6\%$	$0.355 \pm 50.7\%$
> 1.78 cm	$0.229 \pm 31.8\%$	$0.466 \pm 64.3\%$
> 3.16 cm	$1.261 \pm 50.4\%$	$1.544 \pm 90.4\%$
> 5.62 cm	$0.804 \pm 97.6\%$	N/A

3.1.4.3 Final Scaling of Radar-Based Populations

After custom scaling for special populations as discussed in the preceding sections, final adjustments based on object size, eccentricity, and inclination were applied to the model populations to better match the structure of the radar data in terms of surface area flux vs. size. This surface area flux is defined as the number of debris objects that pass through the radar beam, divided by the surface area of the radar beam (assuming the 3-dB beamwidth of the radar) per unit time – in this case on a yearly basis. Specifically, the adjustments shown in Table 3-8 were applied, where W_0 is the initial weight of the object, and W is the final weight. Note that, for fragments from the 10 custom breakups that meet the size, eccentricity, perigee, and inclination criteria indicated, W_0 is the scaled weight based on the size-dependent scaling (Equation 3.1-1). Otherwise, W_0 is the initial weight from the LEGEND simulation.

Table 3-8. Final scale factors applied to radar-based populations in ORDEM 3.1

Reference Population	Size (L_C , m)	Eccentricity	Perigee (km)	Inclination (deg)	Final Scaling
LEGEND (> 1 mm), without 10 custom breakups	< 0.01	-	≤ 2000	$93^\circ < i < 108^\circ$	$W = 2.5 \cdot W_0$
	$0.01 \leq L_C < 0.1$	-	≤ 2000	$68^\circ < i < 80^\circ$	$W = 0.5 \cdot W_0$
	< 0.1	-	≤ 2000	$62^\circ < i < 68^\circ$	$W = 1/3 \cdot W_0$
LEGEND + all special populations (except NaK)	< 0.1	≥ 0.1	≤ 2000	-	$W = 5.0 \cdot W_0$
	$\log_{10}(L_C) < -2.25$	-	-	-	$W = 1.375 \cdot W_0$
	< 0.01	-	-	-	$W = 1.375 \cdot W_0$ $-1.5(\log_{10}(L_C) + 2.25)$

Figure 3-17 shows the comparison of the initial ORDEM 3.1 modeled populations (as modeled by LEGEND), the final ORDEM 3.1 populations after all scalings were applied, and the HUSIR composite dataset, presented as surface area flux vs. altitude for the 1 cm and greater population. The data uncertainties shown are the one σ -confidence intervals. Figure 3-18 shows the same for the 5.6 mm and greater population.

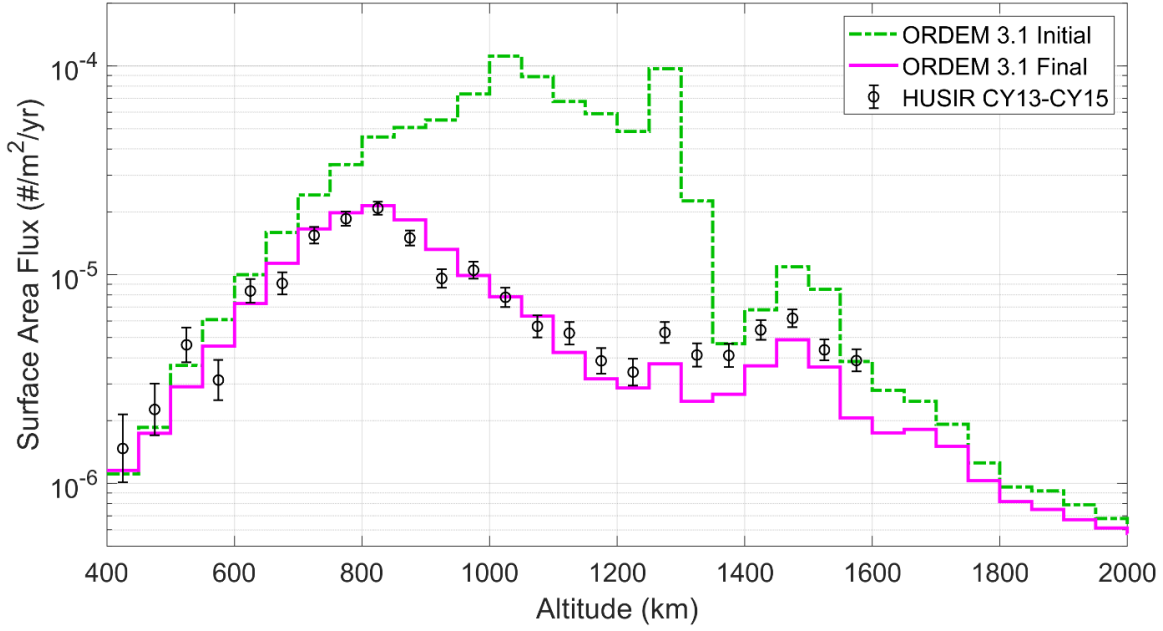


Figure 3-17. Comparison of the surface area flux vs. altitude for a limiting size of 1 cm and larger between the initial unscaled ORDEM 3.1 population, final ORDEM 3.1 population after all radar-based scalings were applied, and measurements from the HUSIR 75E 2013–2015 composite dataset.

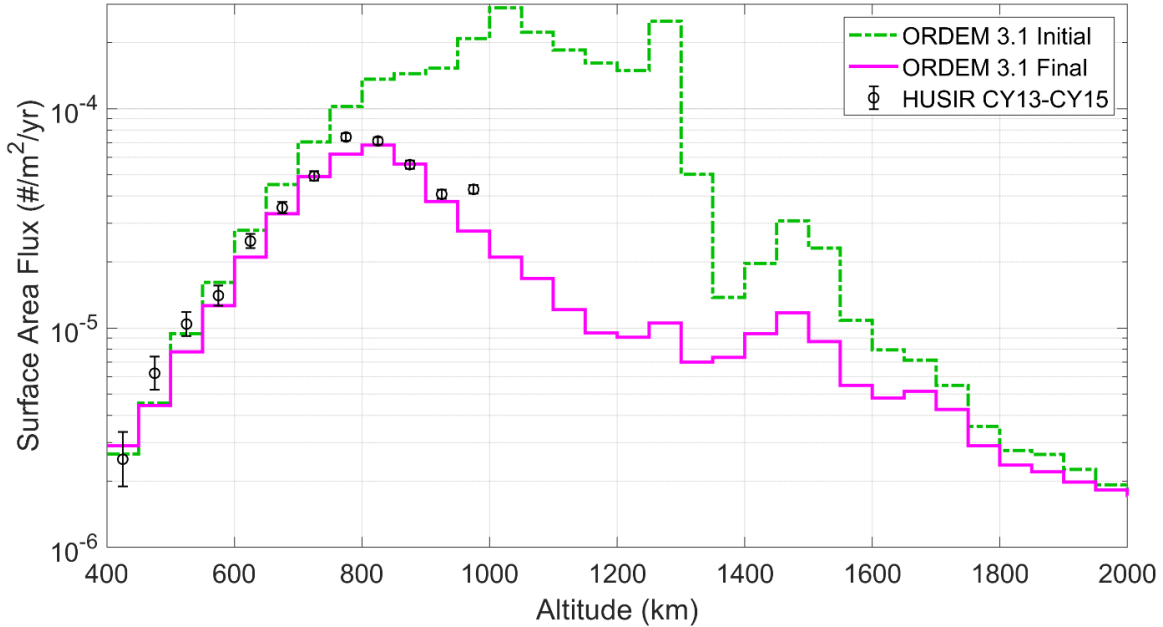


Figure 3-18. Comparison of the surface area flux vs. altitude for a limiting size of 5.6 mm and larger between the initial unscaled ORDEM 3.1 population, final ORDEM 3.1 population after all radar-based scalings were applied, and measurements from the HUSIR 75E 2013–2015 composite dataset.

3.2 *In situ*-Based Populations

The primary contributor to the population of very small (sub-millimeter) debris particles is the surface degradation or erosion of spacecraft materials exposed to the outer-space environment. The physics of the degradation process is not well-understood. For certain materials such as paint, exposure to the

atomic oxygen environment and thermal cycling may be a significant mechanism (Johnson and McKnight, 1987); for metallic particles, secondary debris (*i.e.*, ejecta) from small-debris impacts and micrometeoroid (MM) impacts can excavate significant mass from the target and may be an important contributor. Figure 3-19 depicts an example of space weathering aboard the International Space Station (ISS). Figure 3-20 illustrates the formation of prototypical ejecta and spallation clouds during impact of a small projectile onto a Whipple shield-type bumper. Dedicated studies have been commissioned at the international level to describe resulting surface damage and ejecta production; see IADC, 2013 and IADC, 2018 for such spacecraft damage assessments.

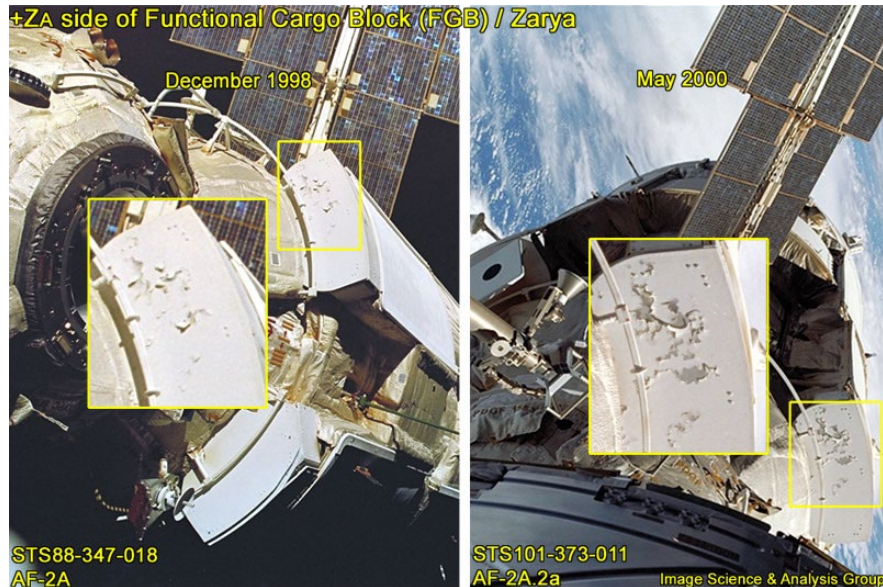


Figure 3-19. Example of chipped paint on coated surfaces aboard the ISS. Note the liberation of a significant amount of the coating, revealing the substrate material, between December 1998 (left) and May 2000 (right).

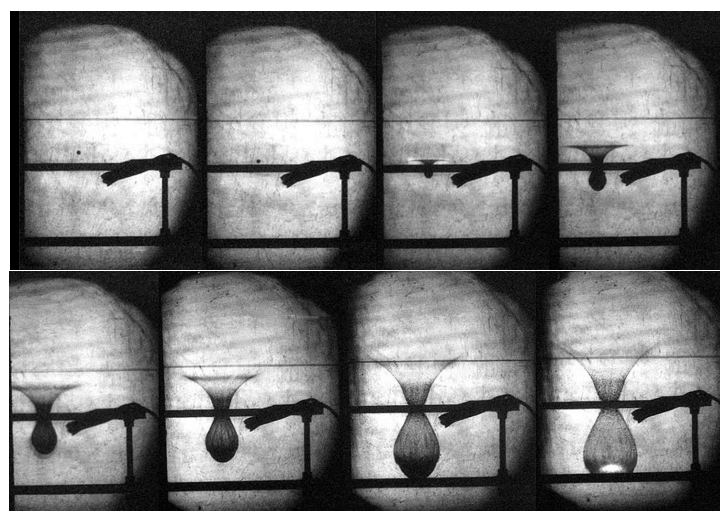


Figure 3-20. High-speed imagery of a spherical particle impacting a Whipple shield test article. Clearly visible are the upwards ejecta and downwards spallation clouds, the latter impacting the target plate.

The models used to produce ORDEM's baseline populations do not attempt to model the cause-and-effect process for degradation products, *i.e.*, impacts of MM and OD particles are not used to generate ejecta-type degradation debris. This process would require an initial MM/OD population or flux to generate the impacts, the results of which would likely require overall ejecta population re-scaling to match the available impact record due to uncertainties in production per impact event, *etc.* Similarly, sophisticated coating ageing and particle liberation models would be required to model, even to a first order, surface degradation caused by weathering; weathering caused by atomic oxygen may differ significantly from that caused by exposure to the solar extreme ultra-violet or ionizing radiation. While investigation into these mechanisms and applicable models is an area of future research, due to the uncertainties involved in this complex process, the production of degradation particles was assumed to follow a simple process.

3.2.1 Reference Population

The degradation source model simulates production of small particles 10 μm to 3.16 mm in size from spacecraft and upper stage ("intact" object) surfaces and was constructed to provide the desired reference populations for the micro-debris population derivations. Since the NASA SSBM produces debris larger than 1 mm, there is overlap between the degradation and breakup populations over the size range of 1 mm to 3.16 mm. Unlike fragmentation debris, however, degradation debris in ORDEM were produced by resident space object surface degradation without attribution to a specific cause or model. The number of micro-debris objects, created by a surface degradation process, was assumed to be proportional to the surface area of a parent body.

The initial LEGEND population served as the main input into the degradation model, and intact objects were used as parent bodies of the degradation particles. Particles were simulated from 1957 to 2050 (historical plus future projection). To minimize output file size, an initial production rate was set to 0.1 particle/ m^2/month (object/surface area/time interval). Intact, parent body candidate objects with perigee altitudes greater than 5000 km or apogee altitudes less than 500 km were omitted from degradation production modeling. In the case of the former population, the products would not be expected to penetrate the LEO zone within the projection lifetime of the model. In the case of the latter population, product lifetimes are significantly shorter than 1 year, in many cases being on the order of days to weeks, and their contribution to the environment was deemed negligible. Additionally, omitting parent body objects below 500 km minimized the effects from human spaceflight. The degradation particles were simulated as having the same initial orbits as their parents (zero relative velocity from the emitting parent object), with their orbits evolving under the effects of gravitational perturbations, solar radiation pressure, and atmospheric drag until they reentered. MD and HD populations were each simulated separately. The number of simulated particles was calculated from a Poisson sample using the initial average production rate, and the sizes of the newly created small degradation particles were chosen between 10 μm and 3.16 mm from a log-uniform distribution. Both MD and HD particles were produced from each parent object, and the size-dependent production rates were scaled to be compatible with data from impacts to STS windows and radiators, as discussed in Section 3.2.5.

A study was conducted to explore the effects of fitting two distinct populations simultaneously: the degradation debris from rocket bodies, and the degradation debris from spacecraft. The effects of distinct debris populations as simulated from low- and high-eccentricity parent populations were also investigated. The contribution to the degradation population using breakup debris as the parent bodies was also analyzed. However, the introduction of these various sub-populations resulted in parameterizations that were computationally unstable (due to the solution being under-constrained). Because of the difficulties in using these split-parent populations, only a single combined-parent population for the final degradation populations was used, as was the approach with ORDEM 3.0. However, the methods developed for these studies are expected to be useful in future analyses.

3.2.2 Supporting Data

Since small particulates are not directly trackable by remote sensing, the primary means of detection is via historical counts of small impact features on returned surfaces. NASA's Hypervelocity Impact Technology (HVIT) group maintains a database of impact features on STS surfaces, based on measurements from post-flight inspections by personnel at Johnson Space Center (JSC) and Kennedy Space Center. Data on size and material of impacts to the STS radiators and windows from 1995–2011 (mission STS 71 to STS 133), defined by the HVIT Shuttle Impact Database (21 February 2012 edition), were used to scale the initial modeled degradation populations based on a reference particle production rate and to establish the final, scaled, small debris population for ORDEM 3.1. These datasets are the same as those used for building ORDEM 3.0, but were reanalyzed for use in ORDEM 3.1.

STS window crater and radiator perforation data were used in building both ORDEM 3.0 and 3.1. Additional impacts to the orbiter vehicle reinforced carbon-carbon (RCC) nose cap and wing leading edges, or to the flexible reusable surface insulation (FRSI) of various outer surfaces, or to the structure, were not utilized for either model building or validation. Craters in the RCC suffered from erosion during the heat of Shuttle reentry, adding uncertainty to the size of the original crater. The FRSI data was not obtained on a consistent or thorough basis like was done for the windows and radiators, and there are some uncertainties in the associated damage equation. In addition, these data sets did not cover as many missions as the windows and radiators. Therefore, it was decided not to use the data from these sources for either model building or validation.

3.2.2.1 STS Window Craters

The STS windows were composed of fused silica outer thermal panes (from the three-layer window configuration) with a total surface area of 3.6 m² distributed among the 11 STS windows. The windows are identified in Figure 3-21.

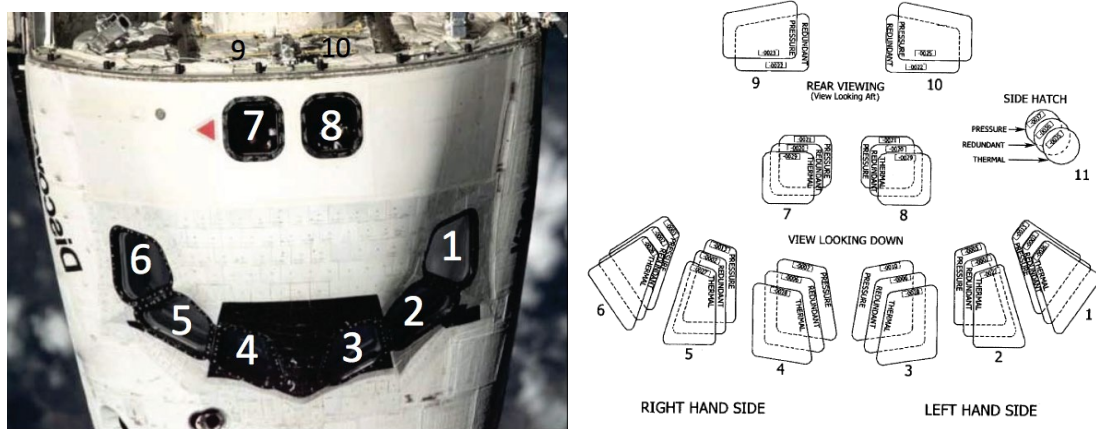


Figure 3-21. Crew module windows location. Note that windows 9 and 10 (aft-facing cargo bay windows) were not used for building ORDEM 3.1 populations.

Fused silica is a brittle target material and impacts typically resulted in conchoidal crater structures. Measurements of impact-crater length, width, and depth from nine window surfaces were used to calibrate the 10 µm – 3.16 mm population for ORDEM development. The aft-facing windows of the cargo bay (windows 9 and 10) were not included in the analysis as they were less susceptible to OD impact during flight due to their nominal in-flight orientation, resulting in a total effective area of 3.4 m² for the window surfaces. The window outer-thermal-pane material of Corning 7940 fused silica allowed for more exact chemical identification of impacting particle types than the radiators, particularly aluminum impactors that were difficult to recognize on the aluminum radiators since aluminum and its alloys were

not a component in the window composition. This small surface area provided the majority of the impacts recorded in the orbiter-impact dataset due to the unique response of the fused silica material under hypervelocity impact conditions, which allowed for the detection of very small impact features.

A total of 86 STS flights were examined post-flight in window surveys. A total of 1986 impacts were recorded, for a mission average of 23.1 impacts. Impactor origin was determined by Scanning Electron Microscopy-Electron Dispersive X-ray (SEM-EDX) analysis of craters conducted at NASA JSC to determine projectile residue material(s) and hence source (MM or OD, following an established classification rubric) and mass density. Categorization of window impacts by type resulted in approximately 70% (1398) unknowns, 13% (265) MM, and 16% (323) OD, as illustrated in Figure 3-22. For those window craters identified as OD, SEM-EDX analysis resulted in the constituent breakdown illustrated in Figure 3-23.

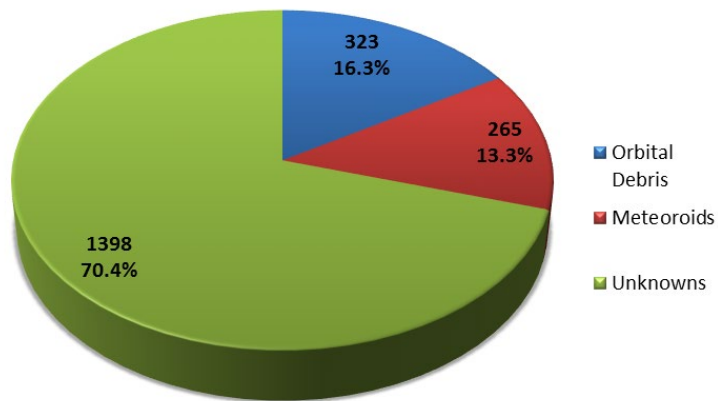


Figure 3-22. Shuttle Impact Database distribution of MM, OD, and unknown impacts on STS windows identified by SEM-EDX analysis. Annotations indicate the absolute number and corresponding percentage of identified constituents out of the total of 1986 identified impacts.

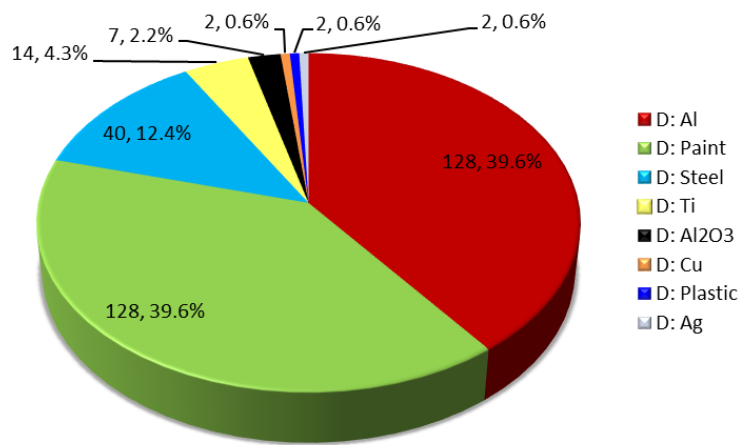


Figure 3-23. Identified OD impactors for STS window craters by material category. The “D” prefix in the legend for each material type refers to the identification of the impactor as debris vs. the other possible classifications of MM or unknown. Annotations indicate absolute number (out of 323 OD) and percentage of that total.

For ORDEM 3.1 development purposes, constituents were classified as being LD ($\rho < 2 \text{ g/cm}^3$), MD ($2 \leq \rho \leq 4.5 \text{ g/cm}^3$), or HD ($\rho > 4.5 \text{ g/cm}^3$). This is slightly different from the density ranges given in Section 1.3.6 in order to group titanium (Ti) in the HD category for the purposes of building the degradation population. Debris impactors were therefore identified by mass density class as 2 LD ("plastic"), 263 MD (aluminum [Al], paint, and aluminum oxide [Al₂O₃]), and 58 HD (Ti, steel, copper [Cu], and silver [Ag]). Due to the small number of low-density debris impactors identified, LD constituents were grouped together with MD objects. This resulted in ORDEM 3.1 development using two density classes from the STS impact data: MD ($\rho \leq 4.5 \text{ g/cm}^3$) and HD. During ORDEM 3.0 development, the ODPO decided to distribute "unknown" category window impacts by the known MM and OD percentages measured on the windows, as illustrated in Figure 3-22, e.g., the identified impactors were regarded as a sample that could be extended to a census of the entire impact record. Extending the density survey of the known impactors to the entire window data set, MM accounts for 45% (895 impactors), MD OD for approximately 47.4% (941 impactors), and HD OD for approximately 7.5% (150 impactors). For purposes of building the ORDEM 3.1 populations, the unknown category impact craters were distributed into MM or OD using rounded percentages of the total: MM 45%, MD OD 46%, and HD OD 9%.

3.2.2.2 STS Radiator Perforations

Eight radiator panels mounted on the inside surface of the payload doors offered a total surface area of approximately 119 m², distributed among eight panels, that remained protected during liftoff and descent; this relatively large surface area (7.6% of vehicle total) increases the number of expected impact features. These panels are diagrammed in Figure 3-24. The radiators were constructed of Al sandwich panels with a thermal Al 2024-T8 facesheet covered with silver-Teflon™ thermal control tape.

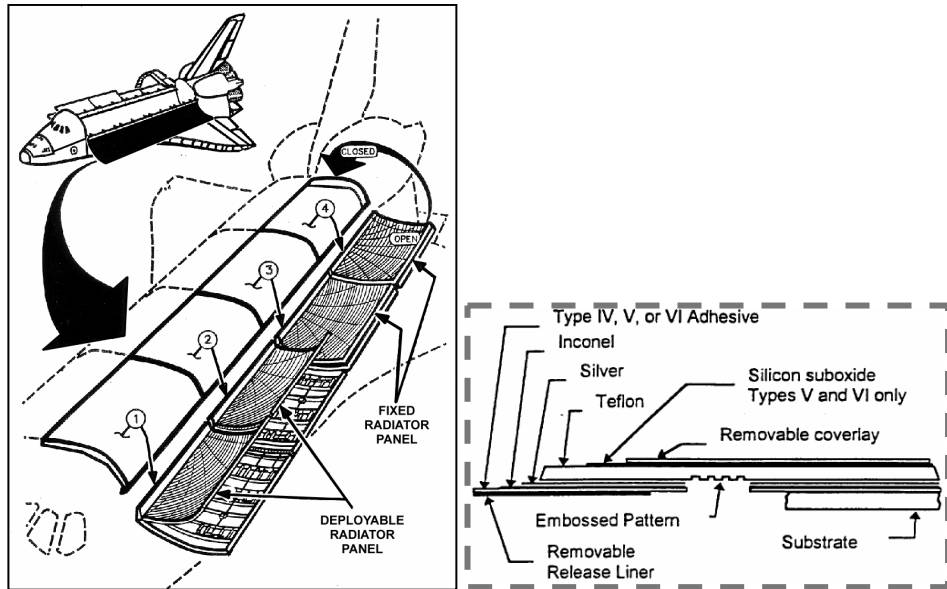


Figure 3-24. Payload bay door radiator diagram.

Three types of damage to the radiators were typically recorded, including thermal tape holes, facesheet craters, and facesheet perforations. The thermal tape had a hole size with its own damage equation, but there were concerns about the accuracy of that data. There were also two types of craters, one that did not perforate the facesheet (in which case the depth of the crater was recorded), and one where the particle perforated the facesheet (in which case the diameter of the perforation was preserved). Because of the small size of the non-perforating craters, the completeness of that data set is in question. Generally, the inspection teams were more concerned with complete perforations and possible risk to the orbiter, so that dataset is expected to be more complete. In addition, the transition damage equations for

large, non-perforating craters is not accurately known like those for full perforations or small “semi-infinite” craters, meaning that only the smallest features (which were not expected to have complete coverage) and the largest features (full perforations) had good damage equations. Thus, only the dataset for facesheet perforations was used during ORDEM 3.1 population development.

A total of 67 STS missions were examined post-flight in radiator surveys. A total of 640 impact features were observed for a flight average of 9.6 impacts. Of these, 133 were facesheet tape perforations, 436 were facesheet craters, and 81 were facesheet perforations. Type categorization, based on SEM-EDX analysis of impact feature residues, was 70% (450) unknown; 13% (86) MM; and 16% (104) OD, an outcome essentially identical to the window distribution. Figure 3-25 illustrates the overall assessment in MM, OD, or unknown categories for all recorded impact features.

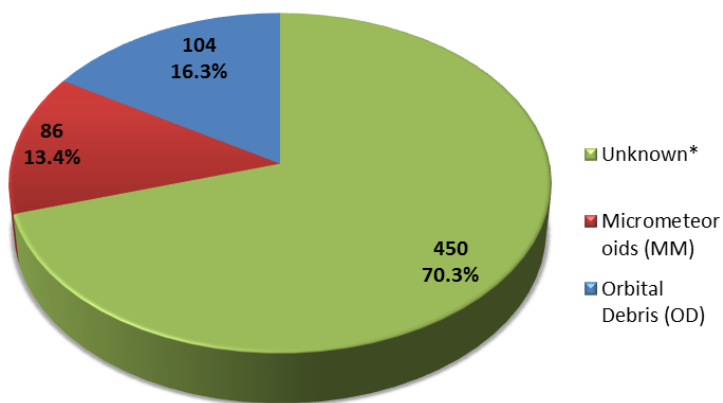


Figure 3-25. Shuttle Impact Database distribution of MM, OD, and unknown impact features on STS radiators identified by SEM-EDX analysis. Annotations indicate the absolute number and corresponding percentage of identified constituents out of the total of 640 identified features.

Facesheet perforations were examined in detail, and additional, detailed SEM-EDX analyses were sponsored by ODPO in 2012 for ORDEM 3.0 development. Figure 3-26 and Figure 3-27 illustrate the breakdowns in the MMOD perforation distribution and identified OD sources, respectively, for radiator perforations.

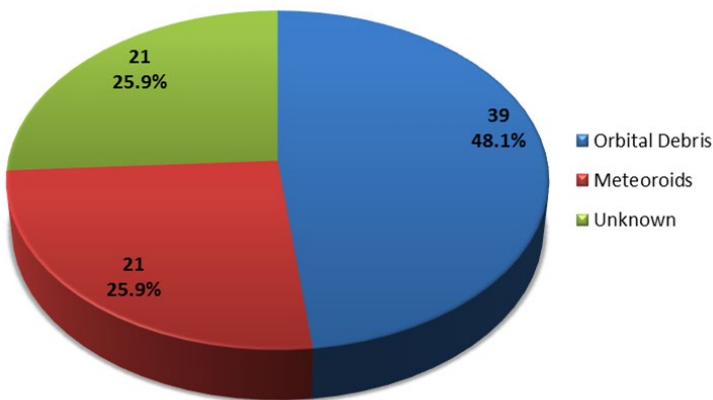


Figure 3-26. Shuttle Impact Database distribution by source (MM, OD, and unknown) for STS radiator perforations. Annotations indicate absolute number (out of 81 total) and percentage of that total.

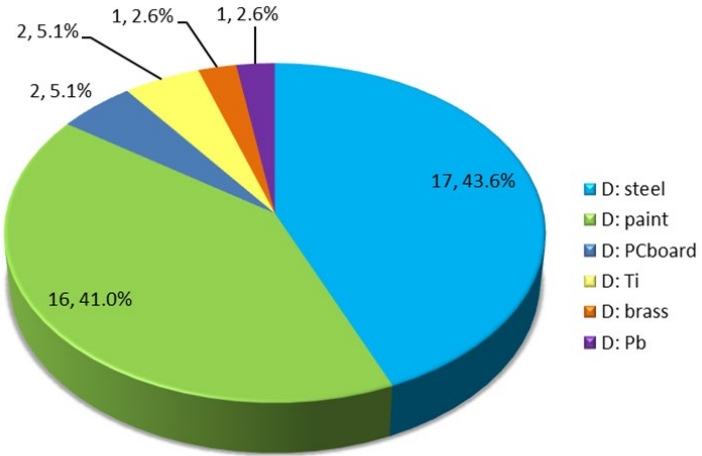


Figure 3-27. STS radiator OD perforations by material type. The “D” prefix in the legend for each material type refers to the identification of the impactor as debris vs. the other possible classifications of MM or unknown. Note that AI is not present as AI traces cannot be distinguished from the radiator’s AI substrate. Annotations indicate absolute number (out of 39 OD) and percentage of that total.

As with the window impacts, the radiator perforation OD constituents were classified according to LD, MD, and HD categories, with 2 LD (5%), 16 MD (41%), and 21 HD (54%) identified. Unlike the window distribution, which unambiguously identified AI impactors, AI impactors could not be identified on the AI radiator surfaces. Thus, the unknown radiator perforation impactors were reclassified to approximately match the window proportions of OD-to-MM and HD-to-MD, resulting in 100% of the unknowns being reclassified as MD (assumed entirely AI). Even with all of the unknowns assigned at MD, however, MD was still underrepresented in the radiator perforations as compared to the windows.

3.2.3 MARK files

To compare the ORDEM OD model with the HVIT STS impact database, the specific as-flown attitudes of the STS missions were taken into account to incorporate the directionality of the debris flux for each STS surface (window and radiator) and mission. This detailed accounting includes the shadowing of surfaces by other spacecraft components, such as when the Shuttle was docked to the ISS. The HVIT team developed so-called “MARK files,” which give the area-time products for each surface and mission. The threat directions of the debris environment are mapped to the angle of impact relative to the surface normal; this mapping is in the form of a matrix and maintained in a file specific to each surface. In this case, the “threat direction” is defined as the direction from which an inbound flux in the local horizontal plane will arrive at the surface. The area-time products were calculated using 90 equally-spaced threat directions in the spacecraft local horizontal plane. The angles relative to the surface normal were divided into nine, 10° segments. The number tabulated represents the area-time product for an STS orbiter vehicle’s particular window or radiator segment, with the projection area for off-normal impacts already taken into account. For calculation of the area-time products, each radiator was divided into quarter strips. Figure 3-28 and Table 3-9 show the individual windows (11 total) and radiator segments (8 total) and their corresponding surface areas, respectively. The calculation of the presented area of specific surfaces was an intermediate step in mapping the predicted degradation production rates to the STS impact data.

In ORDEM 3.0, all of the window and radiator-element areas were combined as a single surface area for ease of computation. For ORDEM 3.1, each window and all eight radiator elements were used independently in fitting the predicted model distributions to the measured data, a distinct processing

improvement relative to ORDEM 3.0. The pointing directions of the individual surfaces were preserved for ORDEM 3.1 to help distinguish debris families, particularly from different inclinations.

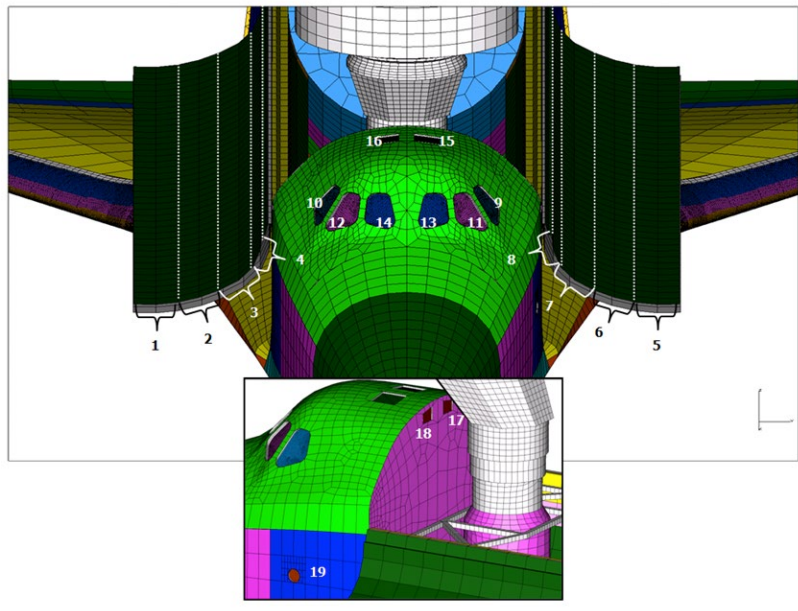


Figure 3-28. Window and radiator identifiers for Table 3-9. Note that the window identifiers here are not associated to those presented in Figure 3-21, but are identifiers corresponding to the MARK files.

Table 3-9. Numerical designation, description, and surface area for each radiator and window. Identifiers correspond to the surfaces shown in Figure 3-28. Crew module window numbers listed correspond to those shown in Figure 3-21.

Identifier	Region description	Area (m ²)
1	Starboard payload bay radiator (outboard)	15.96
2	Starboard payload bay radiator	15.98
3	Starboard payload bay radiator	15.00
4	Starboard payload bay radiator (inboard)	12.69
5	Port payload bay radiator (outboard)	15.96
6	Port payload bay radiator	15.98
7	Port payload bay radiator	15.00
8	Port payload bay radiator (inboard)	12.69
9	Crew Module window 1	0.484
10	Crew Module window 6	0.484
11	Crew Module window 2	0.484
12	Crew Module window 5	0.484
13	Crew Module window 3	0.414
14	Crew Module window 4	0.414
15	Crew Module window 8	0.279
16	Crew Module window 7	0.279
17	Crew Module window 10 (not used)	0.091
18	Crew Module window 9 (not used)	0.091
19	Crew Module window 11	0.061

3.2.4 Feature to Impactor Sizes

Impactor sizes from *in situ* impact data cannot be directly measured, but must be inferred from the measured feature size. Damage equations are used to convert feature size to impactor size based on

debris size, material density, velocity, and impact angle for each surface type. Damage equations are interpretive, empirical equations that relate simple projectile characteristics (diameter d_p , mass density ρ) and impact circumstances (impact/relative velocity, v , and impact angle θ) to tangible impact characteristics (crater depth, crater or perforation diameter, *etc.*). In general, these equations are of the form:

$$Y = c \cdot d_p^\alpha \cdot \rho^\beta \cdot v^\gamma \cdot (\cos \theta)^\delta, \quad 3.2-1$$

where the ensemble ($c, \alpha, \beta, \gamma, \delta$) are fit coefficients for the specific dependent feature characteristic Y , which represents the crater depth, diameter, *etc.* These may be inverted easily to solve for an unknown independent characteristic, usually the projectile diameter d_p , if the impact velocity and angle are known or can be assumed. Other independent parameters are either assumed, estimated in simulation by sampling over distributions in impact parameters (e.g., impact angle and velocity), or determined by analysis, such as SEM-EDX analysis of craters to determine projectile residue material(s) and hence source (MM or OD) and mass density. Extensive hypervelocity impact range testing has yielded sufficient data to formulate damage equations for the returned surfaces used for ORDEM 3.1 development, specifically, the STS window crater depth and diameter and the STS radiator facesheet perforations.

Window crater depth P_{depth} [cm] is a function of the impactor diameter d_p [cm] and other parameters, and can be computed using the NASA-developed damage equation (Burt and Christiansen, 2003):

$$P_{depth} = 0.53 \cdot d_p^{1.06} \cdot \rho^{0.5} \cdot (v \cdot \cos \theta)^{2/3} \quad 3.2-2$$

where all other variables are as defined above. Similarly, crack/flaw (or surface spall) diameter D [cm] can be computed by

$$D = 30.9 \cdot d_p^{1.33} \cdot \rho^{0.44} \cdot (v \cdot \cos \theta)^{0.44} \quad 3.2-3$$

The facesheet perforation diameter damage equation (Hyde, *et al.*, 2015) was updated and revalidated for use during ORDEM 3.0 development and used again in the ORDEM 3.1 build process. The equation for the diameter of a perforation D_{fs} [mm] as a function of the impactor diameter d_p is given by

$$D_{fs} = 0.611 \cdot d_p^{0.957} \cdot \rho^{0.231} \cdot v^{0.638} \cdot (\cos \theta)^{-0.145} \quad 3.2-4$$

In addition, there is an equation that determines whether there will be any radiator facesheet perforation at all given a particle's diameter and other parameters:

$$d_p = 1.05 \cdot \rho^{-1/3} \cdot (v \cdot \cos \theta)^{-2/3} \quad 3.2-5$$

There were also damage equations created for the non-perforating crater depth, and a simple transition equation to estimate the size of the perforation D_{fs} in the transition region where the particle barely perforated the surface. It was discovered that this simple transition equation did not work well, so perforation diameter was only considered accurate if $D_{fs} \geq 1$ mm. This corresponds to "clean" perforations of the facesheet, without transitional crater behavior. However, the general perforation/no-perforation equation was retained to compute the total predicted number of perforations.

3.2.5 Fitting Procedure

Of the missions for which radiator and window damage was recorded, impact data from 60 missions (spanning STS 71-133) were used to build ORDEM 3.1, due to a lack of availability of detailed time-area product histories via “MARK files” (Section 3.2.3) for the earliest missions. The approach used to relate feature size distributions to actual orbital populations and fluxes for the purpose of scaling the initial ORDEM 3.1 degradation production rates is similar to that used for ORDEM 3.0 development and is diagrammed in Figure 3-29. Model populations were used to predict flux on the STS surfaces at the time of measurement. This method used the damage equation applicable to the surface and feature type to convert the modeled flux as a function of size, velocity, and direction into a predicted, feature size distribution. This method is straightforward (when damage equations are available), because the size, velocity, and direction flux distribution in the spacecraft frame are all predicted by the model, and the mapping of these flux distributions to each surface is provided by the MARK files (Section 3.2.3) and their detailed pointing histories for each mission. As discussed in Section 3.2.3, the analysis for ORDEM 3.1 was separated into individual surfaces and individual missions, which allowed for more detailed evaluation of fitting performance, but at the expense of increased complexity of the analysis.

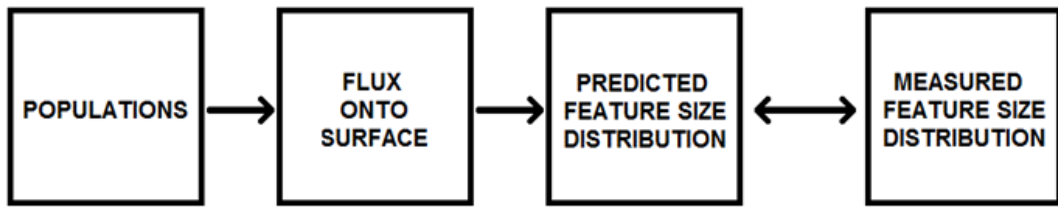


Figure 3-29. General process for comparing modeled fluxes on a surface with the distribution of feature sizes on that surface, used to scale the reference ORDEM 3.1 degradation population to match the STS impact record. Double arrows indicate where comparisons between the model and data were made.

The general procedure for using *in situ* measurement data for the statistical derivation of ORDEM 3.1 degradation population modeling followed several key steps:

1. Selecting and analyzing the data: This step consisted of identifying which missions should be used for each analysis, assigning impact features to each material density category, and defining the size and extent of the defined feature size bins. Careful analysis of the missions indicated that, in the case of the window data, each mission was not complete to the same minimum size, so a careful mission-by-mission analysis of the limiting size was conducted.
2. Simulating reference populations from supporting source models such as LEGEND and a degradation model (Section 3.2.1)
3. Defining model parameters in terms of the reference model populations: This step assigned the simulated particles to one of 50 size categories on a logarithmic (base 10) scale from 10 μm to 3.16 mm. Populations were separated into MD and HD categories.
4. Using the model populations to compute a corresponding prediction for the measured data: This step involved using the orbit of each STS mission, computing the size-dependent spacecraft flux from the reference populations, using the MARK files to predict the velocity and direction-dependent flux for each surface, and predicting the corresponding feature size distributions, also in logarithmically distributed bins.
5. Searching for best estimates of the model parameters based on measurement data through a Maximum Likelihood Estimator (MLE): The flux was parameterized by assigning a separate production-rate scaling to each of the 50 particle-size bins, with the degradation populations and the impact data split into HD and MD populations and fitted separately. In principle, each of the 50 size bins could have been scaled independently, but because of the paucity of data, a low-order (log-log) polynomial was used to compute a scaling function across the size

distribution. The polynomial was then interpolated to the 50 size categories to avoid estimating 50 scaling parameters.

6. Iterating until results converged to a statistically reasonable solution: The iterations were continued to maximize the log-likelihood until the method converged on a best-fit solution. Because multidimensional fits can have issues with local maxima, sometimes restarting the method was necessary to locate a global maximum fit.
7. Assessing the modeling results: The resulting fits were examined and compared to different subsets of the data (such as low-altitude and high-altitude missions). Statistical tests were applied to see if the data represented a reasonable sample from the fitting functions. Balancing the number of terms included in the polynomials was also important; using too many terms resulted in highly-oscillatory behavior, and using too few did not fit the data well.

The general process for building the ORDEM 3.1 degradation population less than approximately 3 mm is illustrated in Figure 3-30.

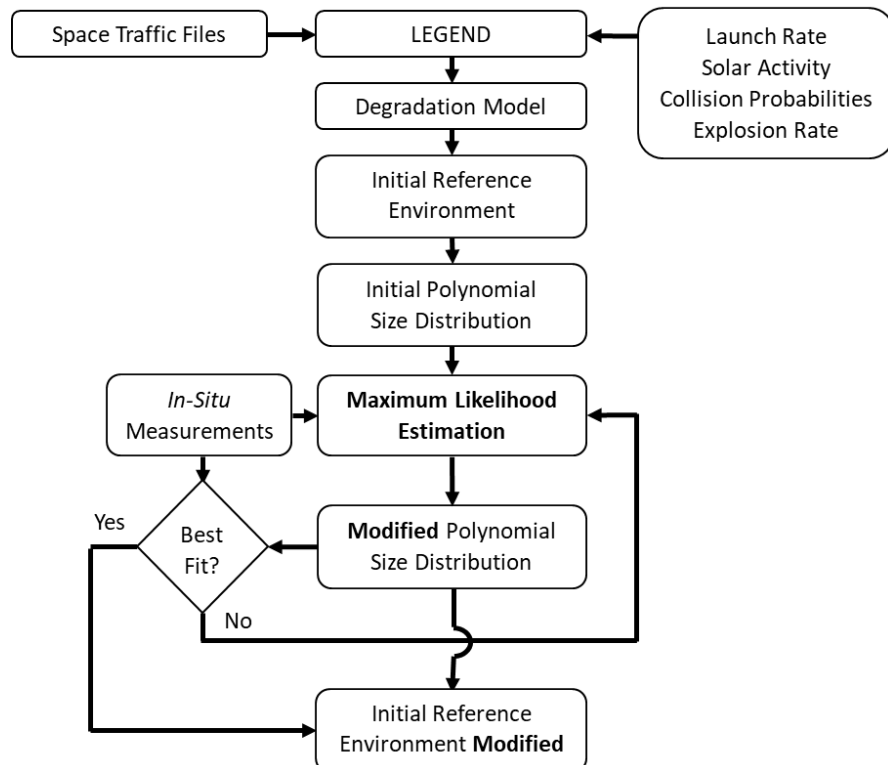


Figure 3-30. Small particle ($\leq \sim 3$ mm) estimation methodology.

Maximum likelihood was computed by comparing the computed Poisson expectation value for each feature size bin, each surface, and each mission against the measured number of features seen. If each feature size bin j has d_j features, and each Poisson prediction is m_j , then the likelihood that the data is a sample from the model is computed using the product of the Poisson probabilities from each size bin:

$$\mathcal{L} = \prod_j \frac{e^{-m_j} (m_j)^{d_j}}{d_j!} \quad 3.2-6$$

It is computationally much easier, however, to compute the log-likelihood, where the product becomes a simple sum, given by

$$\mathcal{L} = \sum_j -m_j + d_j \ln(m_j) - \ln(d_j!). \quad 3.2-7$$

The key is to adjust the values of the m_j 's until the log-likelihood is maximized. Because the data do not change during the fitting process, the $\ln(d_j!)$ term can be ignored for the calculations. There are a number of methods available to maximize this equation, with special emphasis placed on keeping all the m_j values non-negative (as negative Poisson expectation values have no real meaning in this context). The fitting function was parameterized as a log-log polynomial, and a multi-dimensional simplex method was used to solve for the polynomial parameters (Press, *et al.*, 1992).

Maximum likelihood estimation was employed for the development of both ORDEM 3.0 and ORDEM 3.1. For ORDEM 3.1, a continuous third-order polynomial modeled the MD and HD scalings across the range of 50 size categories. For ORDEM 3.0, a fifth-order polynomial was used, but a constraint was applied to the distribution curve at larger sizes, where the sample data are sparse. Using a lower-order fit without a terminal constraint was deemed to be a better approach when considering the estimation of flux uncertainties (Section 4.0), generated from large ensembles of MC simulations (10,000). A lack of terminal constraint permits larger variation in the results of the MC trials in the region of large particle size where data are lacking and thus is likely to be more indicative of the actual uncertainty. The lower order on the polynomial smoothed out wild variations in the curve that were introduced for some of the parametric bootstrap resample cases (Section 4.3).

Figure 3-31 through Figure 3-34 show the comparison between the measured cumulative number of radiator facesheet perforations as a function of size, and the distribution predicted by ORDEM 3.1 from the final degradation population. The ORDEM flux was multiplied by the aggregated, presented-area-time product to represent expected accumulated count on the STS radiators. The isolated point on the left is the predicted and measured total number of perforations of any size, based on the special equation 3.2-5.

The statistical tests used to evaluate quality of fit involved MC Poisson sampling from the model distributions and the computation of the log-likelihood from each sample. The confidence limit was computed by comparing the log-likelihood of the actual data to the distribution of log-likelihoods from the MC sampled data. If the data log-likelihood was higher than at least 10% of the sampled distribution, then it was deemed to be within the 90% confidence limits. Note how the model “splits the difference” between low-altitude and high-altitude HD fits, with the high-altitude fit being somewhat higher than the data (Figure 3-32) and the low-altitude fit being somewhat lower than the data (Figure 3-31).

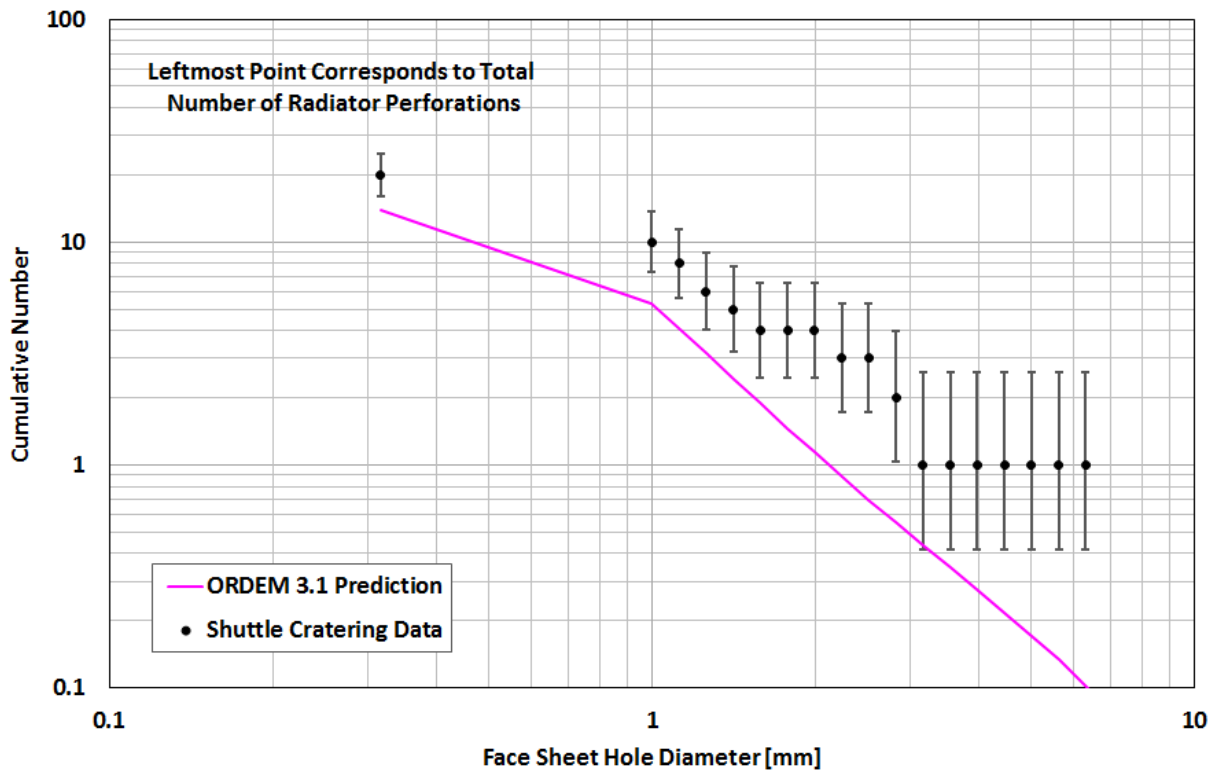


Figure 3-31. Comparison of cumulative number of radiator perforations vs. facesheet perforation diameter for ORDEM 3.1 predictions and STS HD impact data from low altitude missions. Statistical tests indicate that these data are within the 95% confidence limit of being sampled from this distribution. Note that if the rightmost point did not exist, this fit would be substantially improved (well within 90% confidence limits).

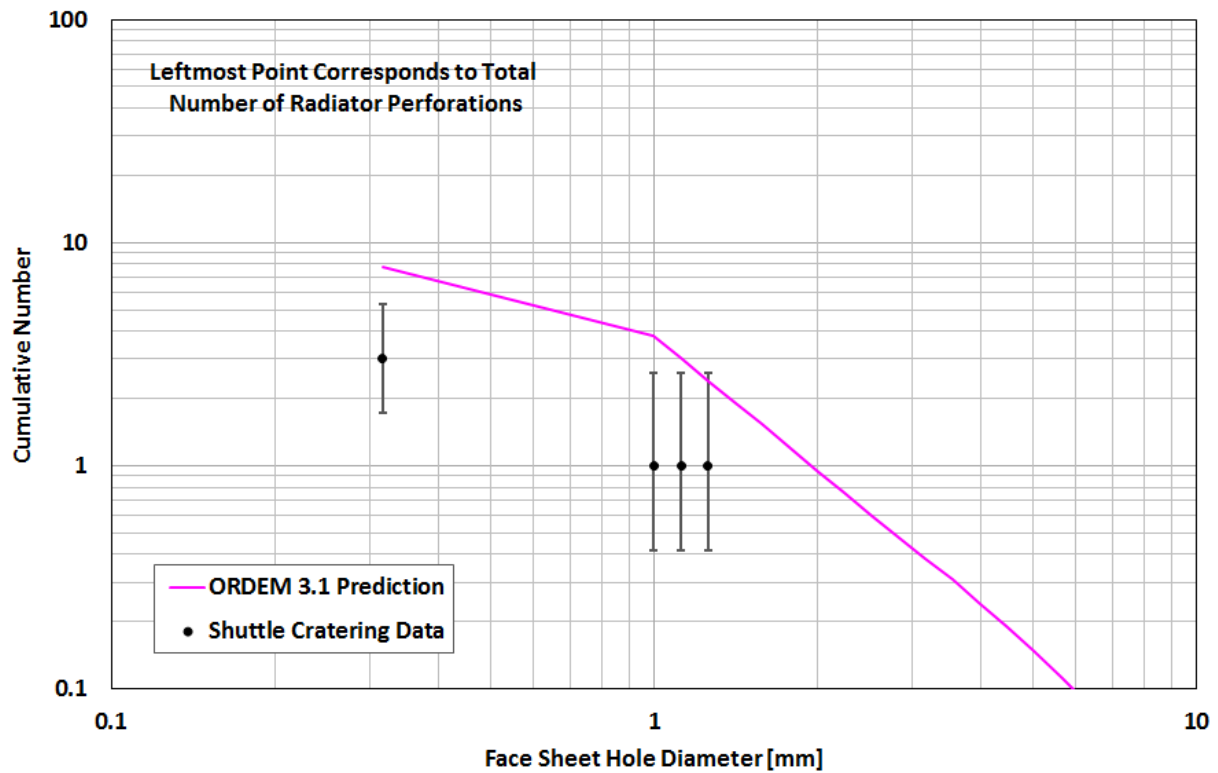


Figure 3-32. Comparison of cumulative number of radiator perforations vs. facesheet perforation diameter for ORDEM 3.1 predictions and HD STS impact data from high altitude missions. Statistical tests indicate that these data are within the 95% confidence limit of being sampled from this distribution.

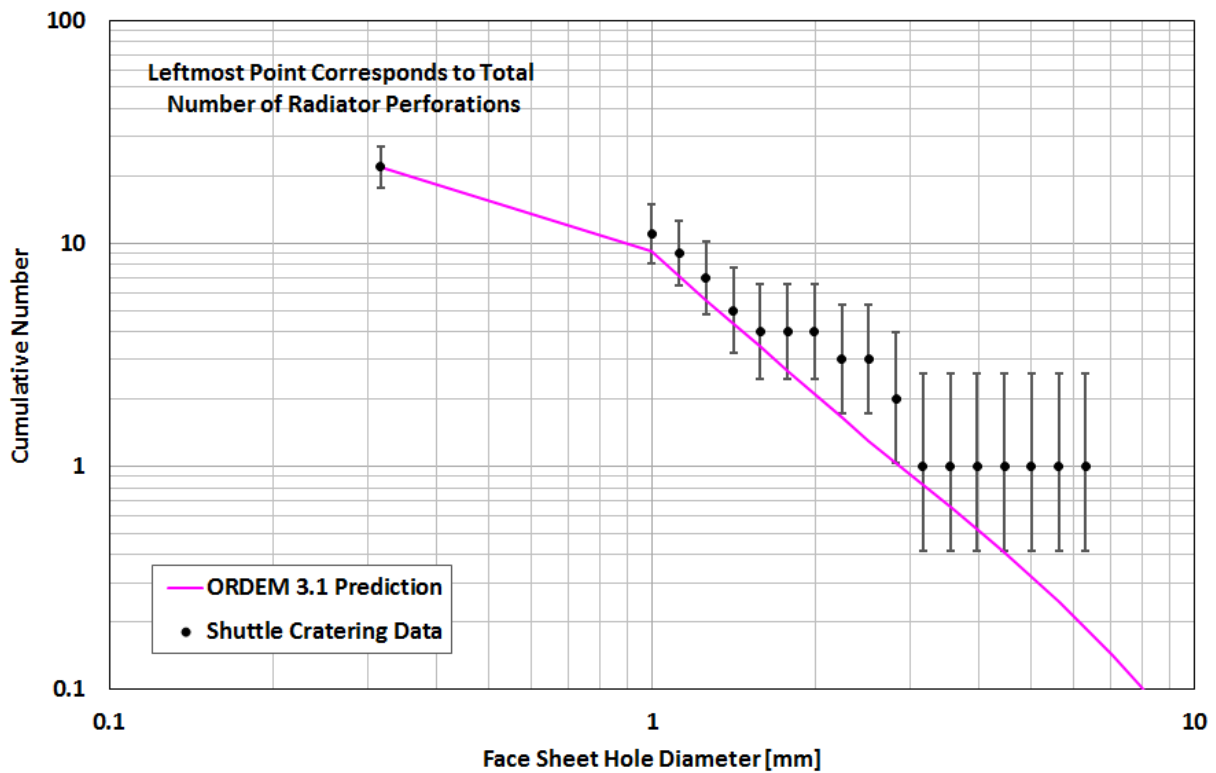


Figure 3-33. Comparison of cumulative number of radiator perforations vs. facesheet perforation diameter for ORDEM 3.1 predictions and HD STS impact data from all missions. Statistical tests indicate that these data are well within the 90% confidence limit of being sampled from this distribution.

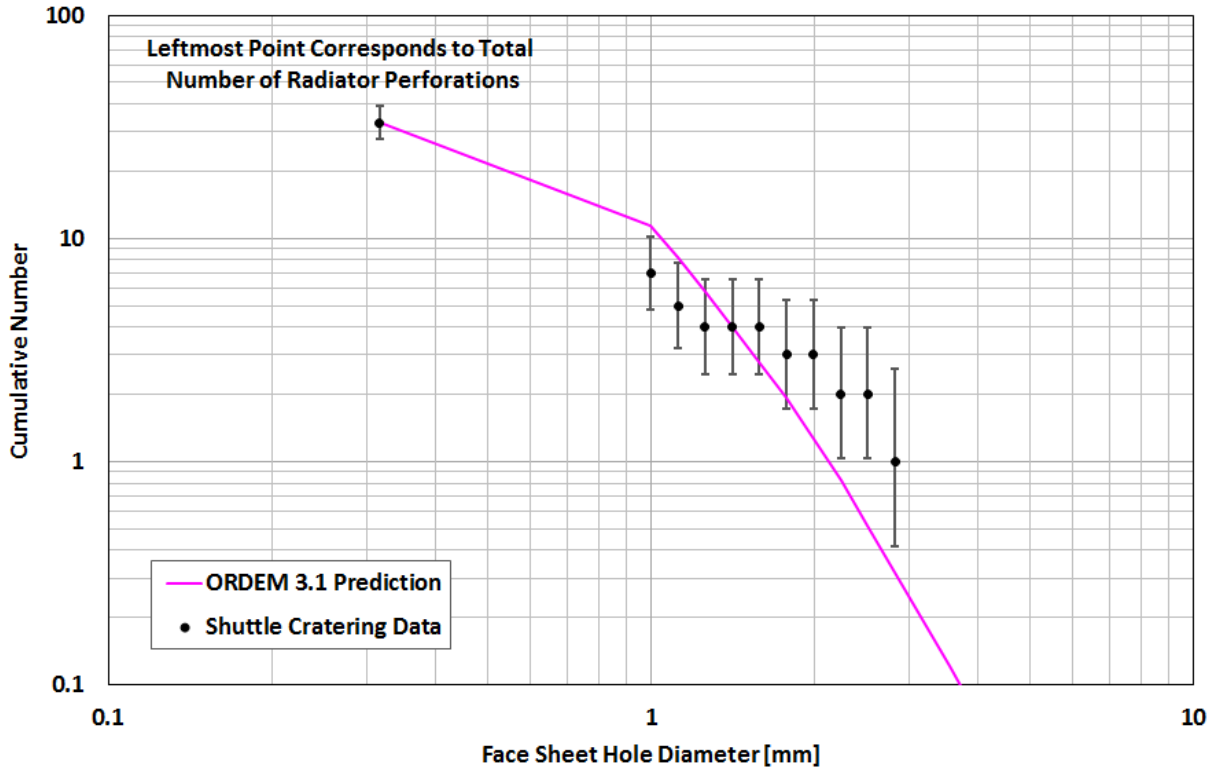


Figure 3-34. Comparison of cumulative number of radiator perforations vs. facesheet perforation diameter for ORDEM 3.1 predictions and MD STS impact data from all missions. Statistical tests indicate that these data are well within the 90% confidence limit of being sampled from this distribution.

3.3 Optical-Based Populations

3.3.1 Reference Population

The GEO population in ORDEM 3.1, covering 10 cm and larger objects, was derived separately from the non-GEO population. As with the non-GEO populations, LEGEND provided the initial population, and future populations were generated as the average of 100 MCs. For GEO, the LEGEND historical period covered 1957–2015, and the launch traffic for the years 2008–2015 were repeated every 8 years for the future propagation. The difference in the historical years covered by the non-GEO and GEO regions is due to a revision in the time period of radar data to be used for building the non-GEO populations in ORDEM 3.1 after processed HUSIR data for CY 2015 became available during ORDEM 3.1 development. This occurred after the non-GEO LEGEND runs through 2014 were completed, and due to resource constraints it was decided to proceed with the non-GEO LEGEND runs as completed. The GEO LEGEND runs, however, were completed after this revision, and therefore the historical period covered years through 2015.

Unlike the non-GEO populations, where the initial LEGEND component is scaled based on available data sources, for GEO, optical data is added to the LEGEND population as a separate component.

Fragmentation debris is implicitly included in the optical datasets, so fragmentation debris from known historical breakups (*i.e.*, prior to 2015) were excluded from the LEGEND reference population to avoid double-counting fragmentation debris. Thus, the historical LEGEND inputs to the ORDEM 3.1 GEO population include only cataloged intact and mission-related debris from the space traffic files. As of the date of ORDEM 3.1 development, seven breakups had been confirmed in GEO (Anz-Meador, *et al.*, 2018). The parent objects and breakup dates are listed in Table 3-10. Four of these breakups occurred

during the historical period covered by LEGEND, two of which – the Ekran 2 spacecraft and Titan 3C (1968-081E) rocket body – were fully identified in terms of time and/or orbital elements at the time of the event. Two additional breakups, Ekran 4 and Ekran 9, were recently confirmed by day of event only, with no breakup time or orbital element information available. Three GEO breakups occurred in 2016 or later, during the future projection of LEGEND, and were explicitly modeled in LEGEND using the NASA SSBM. As only 10 cm and larger objects are modeled in GEO, all GEO objects were assigned a MD designation.

Table 3-10. Confirmed breakup events in GEO as of the time of ORDEM 3.1 development.

Satellite Name	International Designator	SSN Catalog Number	Launch Date	Breakup Date
Titan 3C Transtage R/B (OV2-5 R/B)	1968-081E	3432	26 Sep 1968	21 Feb 1992
Ekran 2	1977-092A	10365	20 Sep 1977	23 Jun 1978
Ekran 4	1979-087A	11561	03 Oct 1979	23 Apr 1981
Ekran 9	1982-093A	13554	16 Sep 1982	23 Dec 1983
Breeze-M R/B (Cosmos 2513 R/B)	2015-075B	41122	13 Dec 2015	16 Jan 2016
BeiDou G2	2009-018A	34779	14 Apr 2009	29 Jun 2016
Titan 3C Transtage R/B (OPS 0757 [TACSAT] R/B)	1969-013B	3692	9 Feb 1969	28 Feb 2018

3.3.2 Supporting Data

For the GEO region, the SSN catalog provides coverage down to a limit of approximately 1 m. To create a more statistically complete GEO population for ORDEM down to 10 cm in size, observations of GEO objects from the Michigan Orbital DEbris Survey Telescope (MODEST) were used. Data from two observation periods covering 2004–2006 (Abercromby, *et al.*, 2010) and 2007–2009 (Abercromby, *et al.*, 2011) were used for development of the ORDEM 3.1 GEO orbital regime.

MODEST is a 0.6-m aperture, Curtis-Schmidt of classical design and is located at the Cerro Tololo Inter-American Observatory (CTIO) in Chile and is equipped with a 2048 by 2048-pixel charged coupled device camera with a 1.3 by 1.3 degree field of view (FOV). The standard exposure time is 5 sec, with a total time between exposures of 37.9 sec. An object's instrumental magnitude is the direct observable in the MODEST survey dataset. The instrumental magnitude is converted to an absolute magnitude using an assumed range, r , of 36,000 km and a Lambertian phase function correction for an astronomical red "R" filter. A 5-sec exposure through a broad R filter centered at 630 nm and 200 nm wide (full width at half maximum) produces a signal-to-noise of 10 on a point source detection of 18th R magnitude under typical dark sky conditions at MODEST. The frame number, right ascension (RA), declination (DEC), instrumental magnitude, epoch, observation date, and universal time (UT) are calculated for each detection of each object. A detection is counted if the object is seen in at least four frames; however, most GEO objects are seen in eight, which equates to observations spanning approximately five minutes of time. The orbital arc is consequently short and an assumed circular orbit (ACO) is thus necessary to obtain the orbital elements.

For each exposure, the day, year, UT, and the field center of the FOV are determined. Then, using an augmented version of the Simplified General Perturbation code (SGP), the satellite catalog is compared to the RA, DEC, and time of each exposure to determine whether an object might be in the FOV. Detected objects that are found to be in the publicly-available SSN catalog, with available Two Line Elements (TLEs), are termed correlated targets (CTs). Detected objects not correlated to objects in the catalog, based on the missed distance (absolute value of the squared difference between the observed and the predicted RA and DEC positions), are termed uncorrelated targets (UCTs).

The MODEST datasets provide the following information for each target (*i.e.*, each detection) in the dataset:

- Detection date
- Detection time referenced to UT
- ID (SSN catalog number for CTs, “99999” or “UCT” for UCTs)
- Observed mean motion (assuming circular orbit)
- Observed inclination (INC, deg, assuming circular orbit)
- Observed Right Ascension of the Ascending Node (RAAN, deg, assuming circular orbit)
- Absolute magnitude
- Predicted eccentricity (ecc, UCTs will be reported as 0 ecc, otherwise ecc is provided from TLEs for CTs)
- Expectation value (EV)
- Number of detections
- Size (d , m)

Each MODEST target has an associated expectation value, EV, which is defined as the likelihood of detection in a given orbit and is calculated based on the location of the telescope at a given date and time. Each MODEST 3-year dataset provides “complete” coverage over the entire 3-year timespan, so that the given expectation value is the likelihood of seeing a target over the entire 3-year interval. This expectation value is used to assign each target a weight, w , representing how many times that target should be counted for a statistical sampling of the population. The weight, or number of objects represented by each target in the MODEST dataset, is equal to the inverse of the expectation value, that is, $w = 1/EV$. An object in the GEO belt that is expected (on average) to be detected multiple times over a set of observation runs would have an expectation value greater than one, and, thus, a weight less than one. This statistically accounts for multiple detections of the same object. Likewise, an object with an orbit that has a low expectation value of being detected due to the observation times and pointing directions would have a weight greater than one, indicating that object is a sample from a larger population that is, on average, undetected or under-sampled. This weighting procedure applies to both UCTs and CTs. The expectation values, and thus the object weights, given in each MODEST dataset are determined based on the observation coverage of each observation campaign, so the weights applied to the targets in the 2004–2006 dataset are independent of the weights applied to targets in the 2007–2009 dataset.

Figure 3-35 and Figure 3-36 show the probability of detection, overlaid with actual detections, for the MODEST observation periods of 2004–2006 and 2007–2009, respectively, in the Cartesian coordinates of $[\text{INC} \cdot \cos(\text{RAAN}), \text{INC} \cdot \sin(\text{RAAN})]$. The probability of detection is shown as a background “tie-dye” pattern. Darker red colors (> 0.8 on color scale) indicate a high probability of detection, given the observing geometry during the applicable period, and darker blue colors (< 0.4 on color scale) indicate low probabilities of detection. In these figures, the color scale is capped at 1.0, so any probabilities greater than 1.0 are reset to 1.0. The actual MODEST detections are overlaid as black diamonds, with filled and open diamonds indicating CTs and UCTs, respectively. Note that each MODEST detection has a weight not necessarily equal to one, based on its expectation value, so that detections in densely-populated regions may be weighted lower to avoid over-counting of those orbits, and detections in sparsely-populated regions may be weighted higher to avoid under-counting orbits that were under-sampled.

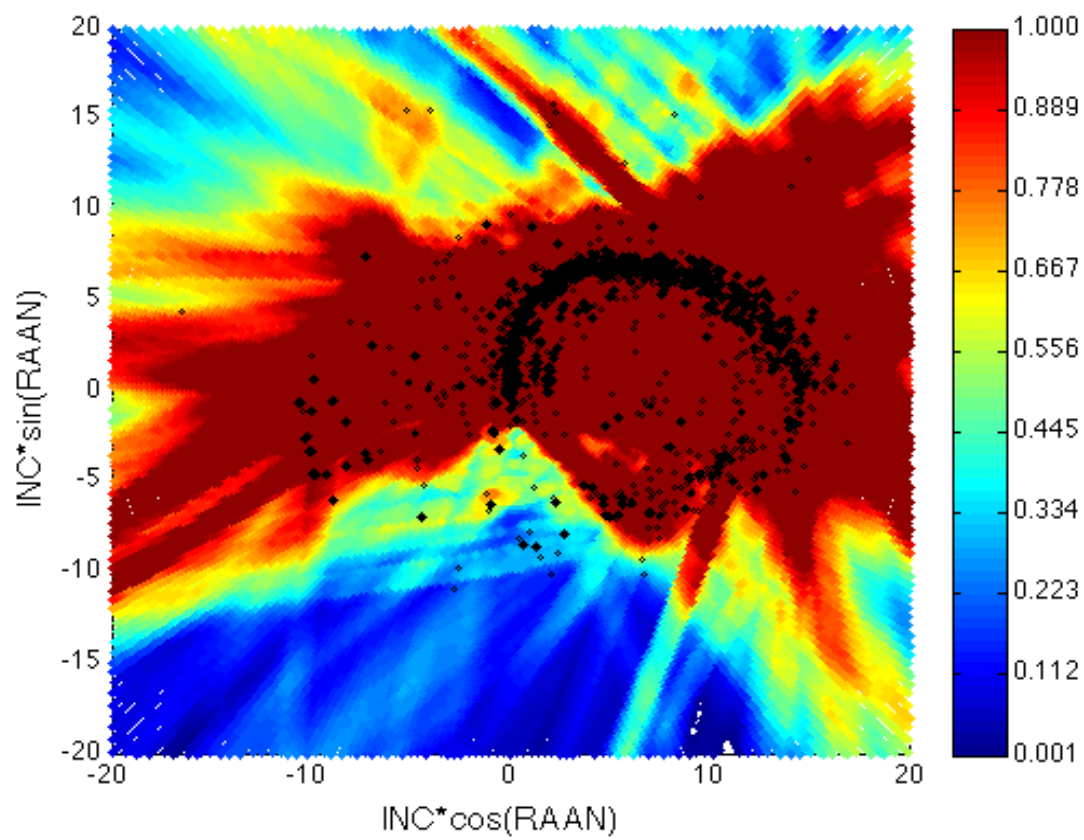


Figure 3-35. Probability of detection, overlaid with actual detections, in $[\text{INC}\cdot\cos(\text{RAAN}), \text{INC}\cdot\sin(\text{RAAN})]$ Cartesian space, for the 2004–2006 MODEST observation period. CTs are represented by solid diamonds and UCTs are represented by open diamonds.

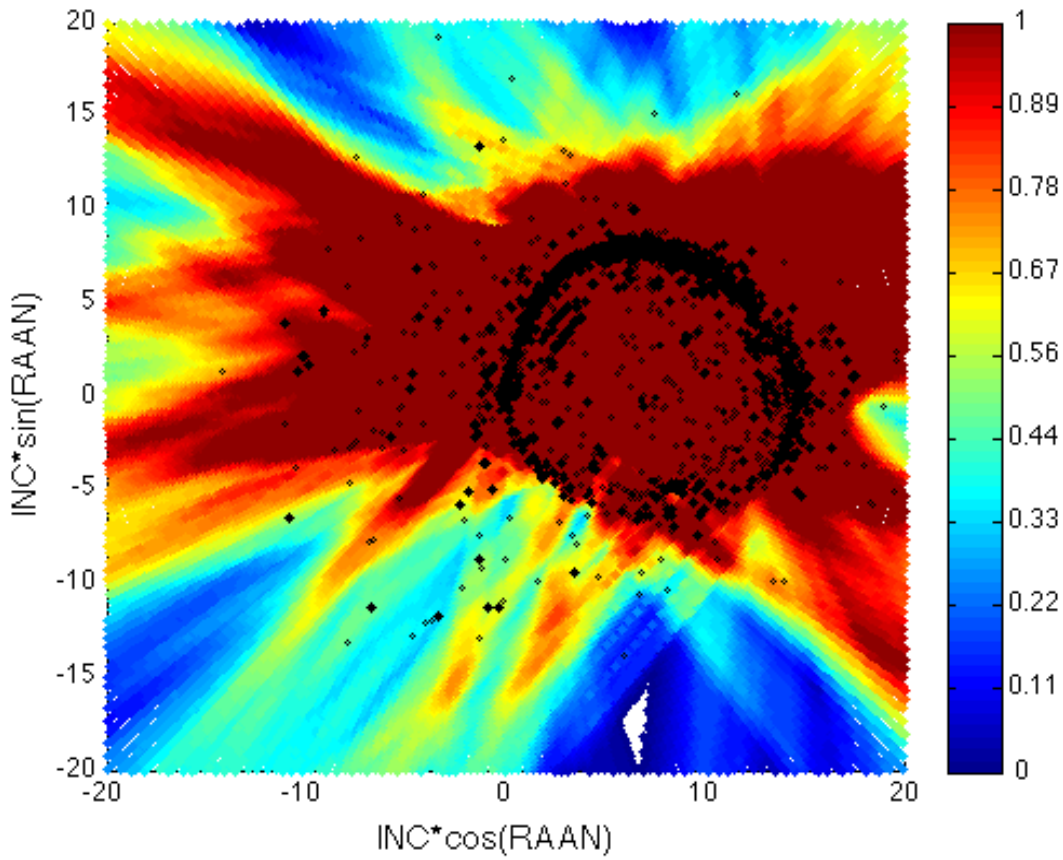


Figure 3-36. Probability of detection, overlaid with actual detections, in $[\text{INC}\cdot\cos(\text{RAAN}), \text{INC}\cdot\sin(\text{RAAN})]$ Cartesian space, for the 2007–2009 MODEST observation period. CTs are represented by solid diamonds and UCTs are represented by open diamonds.

The ring behavior shown by the detections in Figures 3-35 and 3-36 is typical of the orbital behavior of uncontrolled GEO objects. As discussed in Abercromby, *et al.*, 2010, uncontrolled objects in GEO naturally precess in inclination - right ascension space due to effects from the Earth's oblateness and the gravity of the Sun and the Moon. This natural precession traces out a loop in the Cartesian coordinates of $[\text{INC}\cdot\cos(\text{RAAN}), \text{INC}\cdot\sin(\text{RAAN})]$, termed the debris ring, which represents the projection of the orbit's angular momentum vector on the equatorial plane. Objects found to reside on or near this idealized loop represent GEO or near-GEO objects at various stages in their orbital evolution. Controlled (station-kept), intact objects will tend to clump near $(0^\circ, 0^\circ)$ in these coordinates, while derelict intact satellites and debris, will tend to spread out in this ring. The ring of precession exhibits an approximately 50-year cycle, so that fragments from a breakup occurring near $(0^\circ, 0^\circ)$ will traverse clock-wise around the ring, and pass through $(0^\circ, 0^\circ)$ again approximately 50 years after the breakup event. Thus, the location of a group of fragments around the ring can help identify the approximate time and location of the initial breakup event.

The size, d , of each target is inferred from its absolute magnitude assuming a given geometrical albedo of the object's surface, A_g , a phase function, $\Psi(\alpha)$, which defines how sunlight is scattered by the surface in a direction α to the observer, and range, r . Here, $A_g = 0.175$ (Mulrooney, *et al.*, 2008) and $r = 36,000$ km are used. The size determination also corrects observed magnitudes using a uniform phase function (a diffuse Lambertian phase function at a phase angle of $\alpha = 0^\circ$). The magnitude-to-size conversion is thus given by (Barker, *et al.*, 2004):

$$d = \frac{2 \cdot r}{[\pi \cdot A_g \cdot \Psi(\alpha)]^{0.5}} \cdot 10^{\left[\frac{M_{abs}(R) + M_{sun}(R)}{-5.0} \right]} \quad 3.3-1$$

where $M_{abs}(R)$ is the absolute magnitude of the object and $M_{sun}(R) = -27.103$ is the magnitude of the Sun.

Absolute magnitude and size are inversely related so that low magnitude (bright) objects have a large size, and high magnitude (dim) objects have a smaller size. The MODEST system is capable of detecting 19th-magnitude objects, which corresponds to approximately 10 cm in size given Eqn. 3.3-1 and the stated assumptions for magnitude-to-size conversion; however, the dataset is considered complete to approximately 17th magnitude (approximately 30 cm in size). Figure 3-37 shows the distribution in absolute magnitude for the 2004–2006 and 2007–2009 MODEST datasets. There are two peaks in this distribution, corresponding to CTs at lower magnitudes (larger sizes) and UCTs at higher magnitudes (smaller sizes). The peak around 12th magnitude (approximately 2.5 m) in both datasets corresponds to nonfunctional (and presumably tumbling) CTs, while functional CTs peak at around 10th magnitude (Abercromby, *et al.*, 2010 and Abercromby, *et al.*, 2011). The MODEST datasets exhibit a roll-off in the absolute magnitude distribution for magnitudes greater than ~ 17 (sizes smaller than ~ 30 cm), as seen in Figure 3-37. This roll-off in the distribution reflects the detection capability of MODEST, not the true nature of the population. The true debris population is believed to continue at the same slope through fainter magnitudes (smaller sizes) based on comparisons with the standard breakup model for explosions (shown by the “NASA SSBM power law fit” dashed line in Figure 3-37, scaled to approximately match the two MODEST datasets).

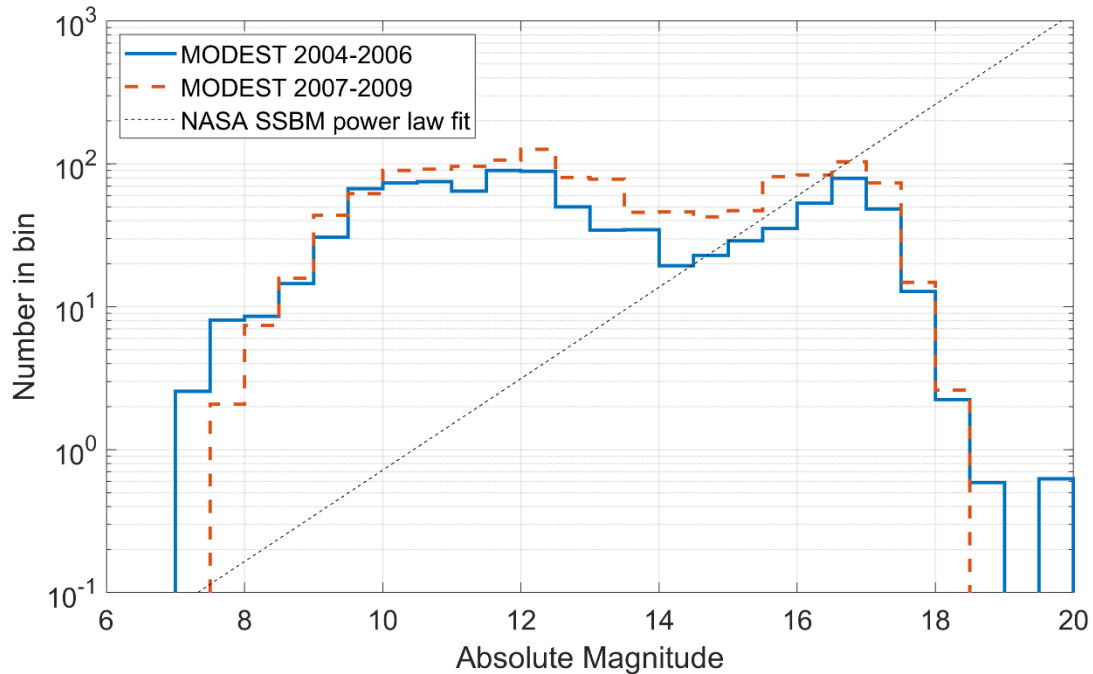


Figure 3-37. Absolute magnitude distribution of the MODEST 2004–2006 and 2007–2009 datasets. The slope of the NASA SSBM power law for explosions, scaled to the MODEST distributions, is overlaid for reference.

Since each MODEST dataset is an independent set of statistical observations of the GEO debris environment, the 2004–2006 and 2007–2009 datasets were combined into a composite 2004–2009 dataset to build the ORDEM 3.1 GEO population. The observed orbital elements for each MODEST

target correspond to a specific detection date and time, so to combine the MODEST detections from the 2004–2006 dataset with those from the 2007–2009 dataset, each target was propagated forward or backward in time to a common epoch of 0h UT 1 January 2007, corresponding roughly to the midpoint of the two datasets. For UCTs, an initial zero eccentricity was assumed for propagation. CTs were propagated using the actual predicted eccentricity as given in the MODEST dataset. An additional constraint for combination of the two separate datasets was imposed based on the observed (circular) mean motion (MM_{circ}). The 2007–2009 UCT and CT debris detections exhibit better coverage in circular mean motion ($MM_{circ} = 0.7$ to 1.3 rev/day) as compared to the 2004–2006 detections ($MM_{circ} = 0.88$ to 1.15 rev/day). The 2004–2006 dataset is considered complete for circular mean motions covering approximately 0.9 to 1.15 rev/day, so detections from the 2004–2006 dataset with MM_{circ} outside this interval were excluded. In the mean motion interval where the datasets overlap, the weights from the individual datasets were averaged. Thus, a composite weight, w_{comp} , was assigned to each detection based on the observed MM_{circ} and given the completeness of each dataset, as summarized in Table 3-11. All subsequent references to number of objects refer to the sum of the composite weights of individual targets, and the final model populations determined from the MODEST dataset take this weighting into account.

Table 3-11. Completeness in circular mean motion and composite weights calculated for the 2004–2006 and 2007–2009 MODEST datasets.

MODEST dataset	Mean Motion (MM , rev/day)	Composite Weight
2004–2006	$0.9 \leq MM_{circ} \leq 1.15$	$w_{comp} = 0.5 \cdot w$
2007–2009	$0.7 \leq MM_{circ} \leq 1.3$	$w_{comp} = \begin{cases} 0.5 \cdot w, & 0.9 \leq MM_{circ} \leq 1.15 \\ w, & \text{otherwise} \end{cases}$

3.3.3 Fragmentation Debris Identification

The MODEST data provides a statistical sampling of the GEO environment for building the ORDEM 3.1 GEO population. Specifically, the MODEST data was used to estimate the fragmentation debris population smaller than the detection limit of the SSN catalog, separately from the LEGEND reference population. Only MODEST debris targets are of interest for building the statistical population since the larger, intact objects are included in the cataloged population modeled by LEGEND. However, extracting fragmentation debris from the MODEST datasets requires some careful analysis of the UCTs. While debris are identified in the CT portion of the database, the UCTs may contain debris as well as intact objects. Larger (brighter) UCTs are likely intact, while smaller (fainter) UCTs are likely debris. Therefore, a method to filter UCTs for only those objects most likely to be GEO fragmentation debris was developed based on a target's size (magnitude) and location relative to the ring of uncontrolled objects discussed above.

A lower size limit of 30 cm, using the albedo-to-size-conversion assumptions discussed above, was imposed as the completeness limit for building the statistical population from the MODEST UCT data. This lower size limit corresponds to an upper limit in absolute magnitudes of approximately 17.1, which is consistent with the roll-off seen in Figure 3-37 for higher magnitudes (smaller sizes) as well as typical reports of the completeness limit of the MODEST datasets. Detections with sizes smaller than 30 cm (magnitudes higher than 17.1) were excluded. An upper size limit of 1.25 m was also imposed to designate an object as debris. This approximately corresponds to a lower limit in absolute magnitude of 14.1, which is near the transition between the peaks for CTs and UCTs seen in the absolute magnitude distribution (Figure 3-37). UCTs with lower absolute magnitudes (and larger sizes) are likely to be intact objects, so they were excluded to avoid over-counting objects that were already modeled in LEGEND. Therefore, only UCT detections with sizes ranging from 30 cm to 1.25 m (absolute magnitude approximately 14.1 to 17.1) were used for building the statistical population. Additionally, only CTs identified as fragmentation debris were included. Note that the upper size limit of 1.25 m was not imposed on CT fragmentation debris since those objects were already identified as debris.

An additional constraint was imposed on the UCTs to filter out detections of non-GEO objects, in particular GTO objects, which have highly elliptical orbits but can appear in the rate box of a GEO object and be misclassified as part of the GEO population due to the short-time arc (5 min) for GEO observations and the circular orbit assumption. In an effort to exclude these objects, which are not truly a part of the statistical GEO environment, a debris ring filter was applied to best capture the ring of naturally precessing, uncontrolled GEO objects. The debris ring filter is defined here based on a range of angles between an object's angular momentum vector and a unit vector perpendicular to the stable Laplace plane, assumed to be inclined at 7.2° (Rosengren, *et al.*, 2014). The angular momentum vector for a target's orbit is dependent on the target's identified INC and RAAN, and these orbital parameters are not largely affected by the circular orbit assumption.

The (specific) angular momentum unit vector, \hat{h} , of a generic orbit plane is given by

$$\hat{h} = \hat{x} \sin(\text{INC}) \sin(\text{RAAN}) - \hat{y} \sin(\text{INC}) \cos(\text{RAAN}) + \hat{z} \cos(\text{INC}). \quad 3.3-2$$

The (specific) angular momentum unit vector, \widehat{h}_0 , of an orbit coincident with the Laplace plane is then defined by

$$\widehat{h}_0 = -\hat{y} \sin(7.2^\circ) + \hat{z} \cos(7.2^\circ). \quad 3.3-3$$

The orbit angle, α , between an object's orbit plane and the stable plane is given by the dot product of the angular momentum vectors:

$$\cos(\alpha) = \hat{h} \cdot \widehat{h}_0 \quad 3.3-4$$

$$\beta = \cos^{-1}(\hat{h} \cdot \widehat{h}_0). \quad 3.3-5$$

Choosing a range of values for β results in a double-ring structure when projected in $[\text{INC} \cdot \cos(\text{RAAN}), \text{INC} \cdot \sin(\text{RAAN})]$ space. Figure 3-38 shows the composite UCTs and CT debris from the MODEST 2004–2009 combined datasets, propagated to 0h UT 1 January 2007 and overlaid with the limits of the debris ring filter. Clouds associated with the four GEO breakups that occurred prior to 2009 are also indicated. The debris ring is then defined by $\beta \in 7.2^\circ \pm \Delta$, and $\Delta = 2.6^\circ$ and was chosen to best capture the cluster of MODEST detections near the modeled Titan 3C (1968-081E) breakup. Thus, MODEST targets with orbits satisfying $4.6^\circ \leq \beta \leq 9.8^\circ$ were selected to build a composite MODEST dataset that formed the basis of the ORDEM 3.1 GEO population.

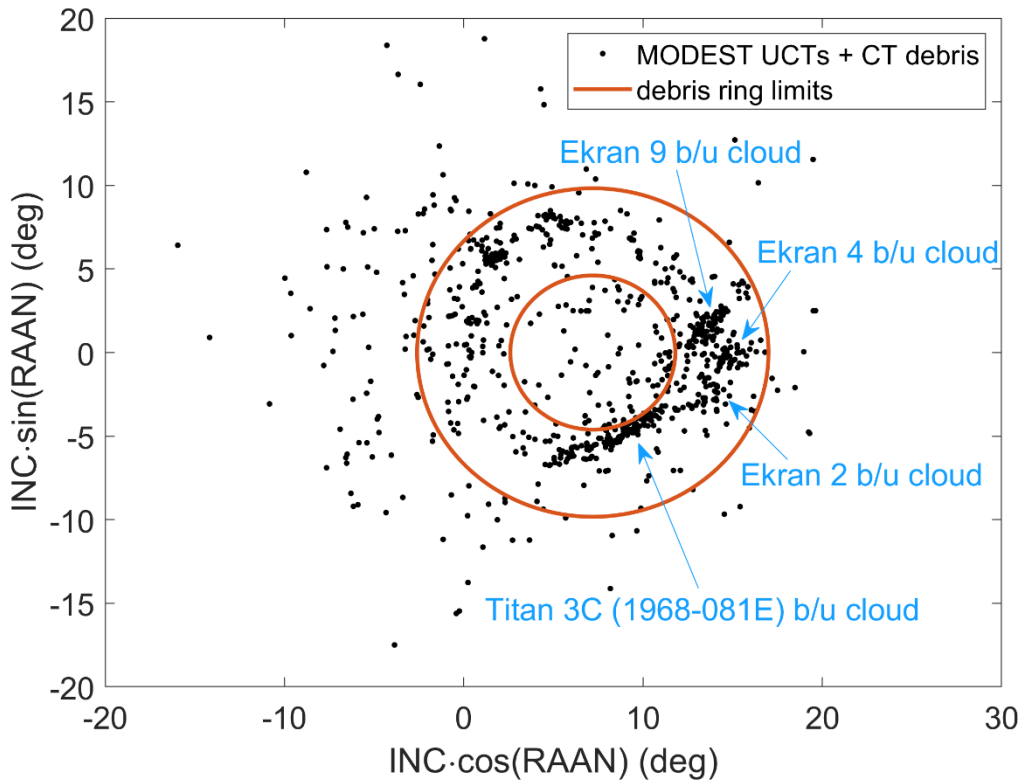


Figure 3-38. MODEST 2004–2009 UCTs and CT debris, propagated to the common epoch of 0h UT on 1 January 2007 and projected in $[\text{INC}\cdot\cos(\text{RAAN}), \text{INC}\cdot\sin(\text{RAAN})]$ Cartesian space, overlaid with the debris ring limits calculated based on the angle between the orbit plane and that of the stable Laplace plane. General regions of fragments associated with the four GEO breakups that occurred prior to the MODEST campaigns are indicated for reference. Objects seen outside the ring were excluded from the model as probable non-GEO objects imitating GEO behavior over the short-time arc of observations.

3.3.4 Assigning Orbital Elements

To incorporate the MODEST targets into the ORDEM GEO population, the full set of orbital elements needed to be determined. Since a circular orbit assumption is made for MODEST UCTs, a more statistically accurate orbit requires a non-circular mean motion and eccentricity. Non-circular mean motion and eccentricities for UCTs were assigned based on breakups modeled using the SSBM.

A distinct relationship can be seen between the mean motion and the orbit angle (β) of fragments modeled for the GEO breakup events. Figure 3-39 shows these relationships for the modeled Ekran 2, Titan 3C (1968-081E), Ekran 4, and Ekran 9 breakup clouds. Since there is currently no information available for the breakup time of day of Ekran 4 and Ekran 9, sample breakup times were used to model the breakups and propagate them to a common epoch. The resulting sample breakup clouds were compared to the shapes of detection clusters in the MODEST composite dataset to visually determine a best-match for the estimated breakup time, leading to breakup times of 00:00 and 18:00 for the Ekran 4 and Ekran 9 breakups, respectively, on their respective breakup dates. While the modeled fragments for Ekran 2, 4, and 9 show relatively linear behavior for mean motion as a function of orbit angle, the modeled Titan 3C (1968-081E) fragments follow more nonlinear behavior.

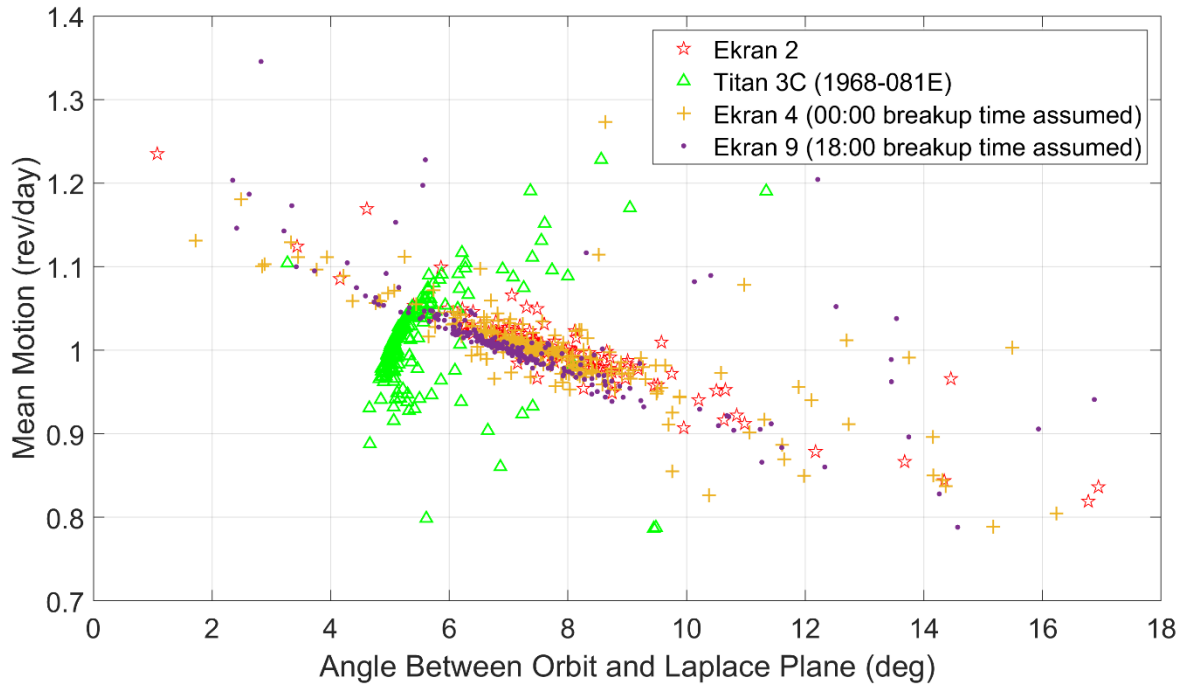


Figure 3-39. Mean motion as a function of the angle between the orbit plane and the stable Laplace plane for the modeled Ekran 2, 4, and 9 and Titan 3C (1968-081E) breakup clouds, propagated to the common epoch of 0h UT on 1 January 2007.

A MODEST target's orbit angle can be determined directly from the observed INC and RAAN, which are not significantly affected by the circular orbit assumption. Thus the orbit angle was used to first assign a non-circular mean motion for the MODEST UCTs based on fits to these curves. The best-fit curve for each modeled breakup cloud was assumed to represent the mean of a normal distribution from which to draw a random mean motion for a given value of orbit angle. The standard deviation for the normal distribution was calculated as twice the mean of the residuals of the curve fit. Table 3-12 shows the curve fits for mean motion as a function of orbit angle and the mean of the residuals from the curve fit for each modeled breakup cloud. Regions around each identified breakup in $[INC \cdot \cos(RAAN), INC \cdot \sin(RAAN)]$ space were used to identify which modeled curve fit to apply for a given MODEST UCT; for example, if a MODEST UCT was located in a region around the Ekran 2 modeled breakup cloud then the Ekran 2 curve fit was applied.

Table 3-12. Curve fits for mean motion (MM) as a function of orbit angle (β) for the modeled Ekran 2, 4, and 9 and Titan 3C (1968-081E) breakup clouds.

Satellite Name	Curve Fit	Mean of Residuals
Ekran 2	$MM = -0.02297\beta + 1.179$	0.022
Titan 3C (1968-081E)	$MM = -1630(\beta - 0.3)^{-6.1} + 1.131$	0.025
Ekran 4	$MM = -0.02355\beta + 1.178$	0.036
Ekran 9	$MM = -0.02681\beta + 1.189$	0.055

Similarly, the modeled breakup clouds show distinct relationships between mean motion and eccentricity of the modeled fragments for the GEO breakup clouds, as seen in Figure 3-40. All four breakups show

clear V-shape behavior, with a slightly greater spread seen for the Titan 3C (1968-081E) modeled breakup. Thus, once a UCT's non-circular mean motion was assigned based on its orbit angle, a non-zero eccentricity was assigned from the mean motion in the same manner, using curve fits for the modeled eccentricity as a function of mean motion.

Table 3-13 shows the curve fits for eccentricity as a function of mean motion and the mean of the residuals from the curve fit for each modeled breakup cloud. Similar to the MM vs. β curve fits, eccentricity was drawn from a normal distribution with mean value from the curve fit and standard deviation equal to twice the mean of the residuals, with the additional constraint that eccentricity must be non-negative.

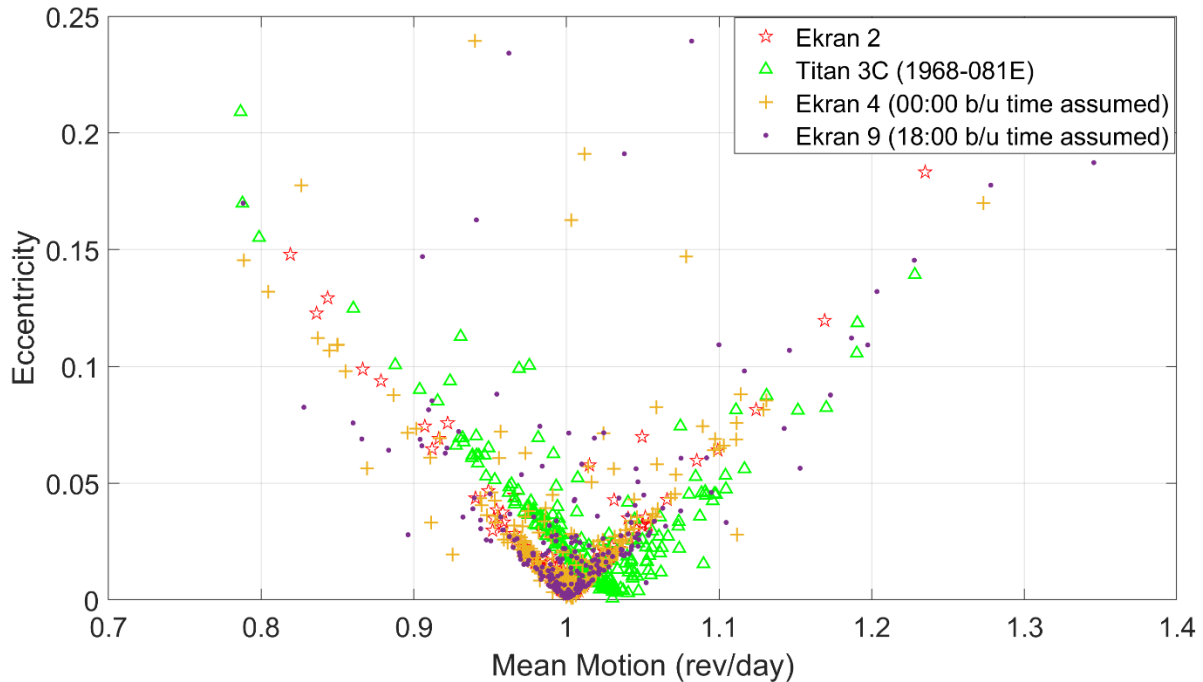


Figure 3-40. Eccentricity as a function of mean motion for the modeled Ekran 2, 4, and 9 and Titan 3C (1968-081E) breakup clouds, propagated to the common epoch of 0h UT on 1 January 2007.

Table 3-13. Curve fits for eccentricity (ECC) as a function of mean motion (MM) for the modeled Ekran 2, 4, and 9 and Titan 3C (1968-081E) breakup clouds.

Satellite Name	Curve Fit	Mean of Residuals
Ekran 2	$ECC = 0.7101 MM - 1.003 + 0.001046$	0.007
Titan 3C (1968-081E)	$ECC = 0.6711 MM - 1.029 + 0.002887$	0.01
Ekran 4	$ECC = 0.6533 MM - 1.003 + 0.003356$	0.025
Ekran 9	$ECC = 0.6347 MM - 1.009 + 0.003958$	0.029

For a UCT not in a region near any of the identified breakup clouds, non-circular mean motion and eccentricities were applied based on generic GEO breakups. A set of 100 breakups was modeled with a mean motion of 0.99 rev/day, corresponding to the peak in the mean motion distribution seen for catalogued GEO objects, to get a statistical sample of applicable mean motions and eccentricities for the

resulting fragments. A random, non-circular mean motion was drawn from the cumulative mean motion distribution of this statistical sample, and a non-zero eccentricity was then drawn based on the mean motion, similar to those assigned for the identified breakups. Figure 3-41 shows the eccentricity vs. mean motion curve for the statistical breakup sample, which exhibits a pseudo-absolute value behavior, asymmetric about $MM = 0.99$. Thus, two curve fits were used depending on the mean motion of the object. These are shown in Table 3-14.

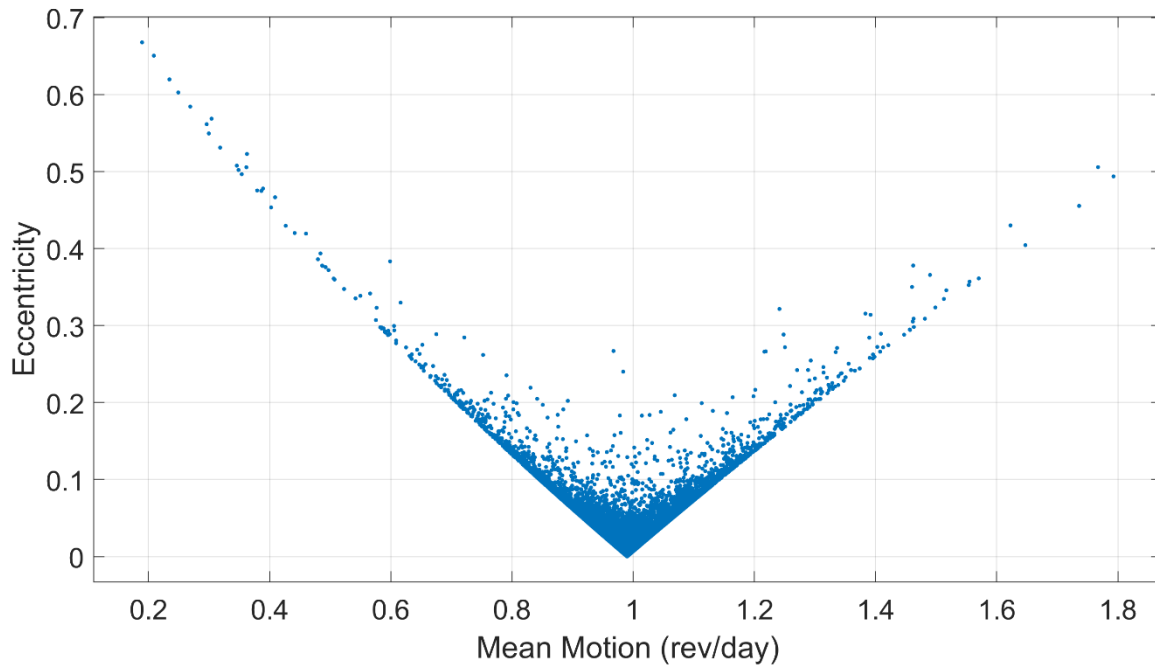


Figure 3-41. Eccentricity as a function of mean motion from 100 generic modeled breakups in GEO with an initial mean motion of 0.99 rev/day.

Table 3-14. Curve fits for eccentricity (ECC) as a function of mean motion (MM) from 100 generic modeled GEO breakups with an initial mean motion of 0.99 rev/day.

Satellite Name	Curve Fit	Mean of Residuals
Generic breakup, $MM < 0.99$	$ECC = 0.17MM^2 - 1.01MM + 0.83$	0.01
Generic breakup, $MM \geq 0.99$	$ECC = 0.66MM - 0.65$	0.01

3.3.5 Extending Population to 10 cm

The composite 2004–2009 MODEST dataset is considered complete down to 30 cm, and this composite dataset was used to extend the ORDEM 3.1 GEO population down to 10 cm. The slope of the cumulative size distribution curve of debris in the composite dataset was used to extrapolate the population down to smaller sizes. The cumulative number of fragmentation debris as a function of size (characteristic length) is expected to follow a power law (Johnson, *et al.*, 2001). A fit to a power law was determined for the cumulative size distribution of the MODEST composite dataset, yielding the following function:

$$N_C = 37.9L_C^{-1.6}$$

3.3-6

where N_C is the cumulative number of objects for a given size and larger, and L_C is the size (characteristic length) of the object. Note that the slope of this best-fit power law matches that of the NASA SSBM for explosions (Johnson, *et al.*, 2001). The comparison of the binned differential size distribution of the MODEST composite dataset and the power law curve fit is shown in Figure 3-42. Uncertainties shown for the MODEST datapoints are the one σ -confidence intervals from the standard Poisson counting error:

$$\sigma = \sqrt{\sum_{i=1}^M w_i^2} \quad 3.3-7$$

where M is the number of MODEST targets in the bin of interest, and w_i is the weight of an individual target.

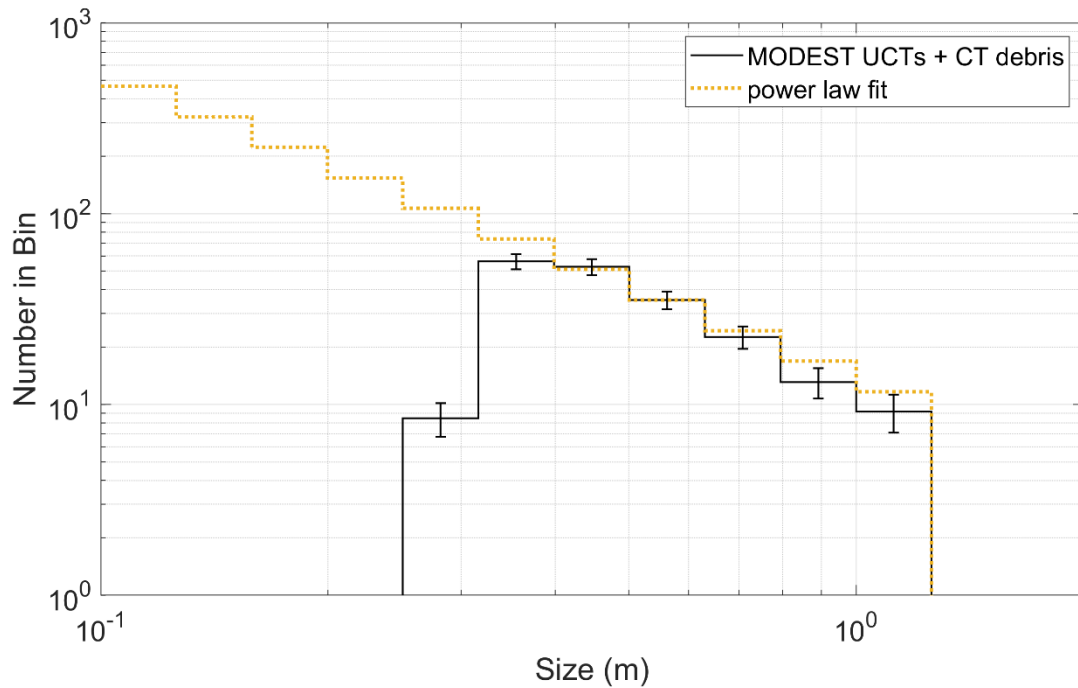


Figure 3-42. Binned differential size distribution for the UCTs and CT debris from the 2004–2009 composite MODEST dataset, propagated to the common epoch of 0h UT on 1 January 2007 and limited from 30 cm to 1.25 m in size. The distribution from the power law curve fit is shown extended down to 10 cm.

Objects smaller than 30 cm, down to 10 cm in size, were added to the modeled GEO population according to this size distribution. Following this power law, for each object expected in the 10 – 30 cm range, a size was assigned randomly from the cumulative power law curve in the same manner as is done for modeling breakups with the SSBM. An orbit was assigned based on the orbits in the 30 cm – 1.25 m composite dataset. Specifically, a MODEST target was randomly chosen from the cumulative normalized weight distribution of the composite dataset

$$W_j = \frac{\sum_{i=1}^j w_i}{\sum_{i=1}^N w_i}, \quad j = 1, \dots, N \quad 3.3-8$$

where N is the total number of MODEST targets in the composite dataset, and the orbit of that chosen target was assigned to the object smaller than 30 cm. In this way, those targets from the MODEST composite dataset with higher weights were more likely to be chosen. This approach intrinsically assumes that each MODEST target observed is representative of a set of objects with the same orbit, originating from the same parent object, and introduces those fragments with a size too small to be detected by MODEST into the GEO population.

The process to sample the non-circular orbits of UCTs and assign sizes and orbits to the population extrapolated down to 10 cm was implemented using a MC approach. The overall process for building the statistical GEO population for ORDEM 3.1 from the MODEST 2004–2009 datasets can be summarized as follows:

1. Assign non-circular mean motions and eccentricities to the “debris ring”-filtered UCTs using distributions from modeled breakups.
2. Extend the population to 10 cm using the weights, sizes, and orbital elements of the filtered MODEST dataset with sizes larger than 30 cm.
3. Combine with CT debris that have sizes greater than 1.25 m.
4. Repeat steps 1–3 for each MC sample (100 times).
5. Calculate distributions in each GEO orbital parameter bin based on the average of the 100 MCs.

4.0 CALCULATION OF FLUX UNCERTAINTIES

The ORDEM software keeps track of the population uncertainties from the derivation of the initial reference population all the way to the individual flux direction/velocity/material/size level. This allows risk assessment tools to best track the uncertainty in the final risk numbers, which includes correlations between directional fluxes. However, tracking and propagating multidimensional uncertainties is difficult, because many of the parameters of interest are often correlated or anti-correlated. An example is shown in Figure 4-1 where a particular orbit family contributes flux over a variety of yaw (local azimuth) angles and relative velocities on the spacecraft. The flux pattern from this population is correlated from one yaw/velocity bin to another, but not necessarily correlated to a similar yaw/velocity pattern from a different orbit family.

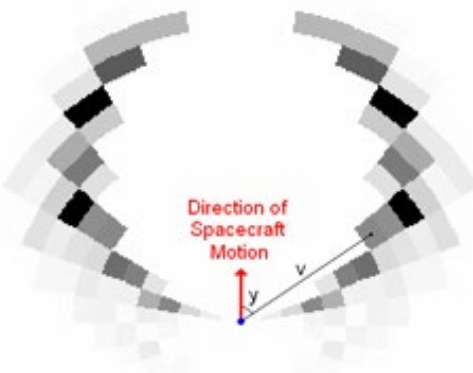


Figure 4-1. Example of correlated fluxes across yaw and velocity bins from a particular orbit family. The same orbit family of debris contributes to flux from different directions and velocities.

4.1 Errors and Propagation of Uncertainties

A key effort of ORDEM was to include accurate estimates of the uncertainties in the modeled populations and carefully track the propagation of these uncertainties to the final flux product. The first process that introduces uncertainties is that the orbit populations are binned by orbit parameters (perigee altitude, inclination, and eccentricity for non-GEO populations and mean motion, inclination, eccentricity, and ascending node for GEO populations). These orbit population densities are assembled using individual orbits that are output from different source model programs (e.g., LEGEND) and/or catalog data. The modeled objects placed into these orbit bins are weighted by different amounts to simulate the number of objects estimated to actually be in that particular orbit (sometimes one modeled object represents many actual objects). In addition, each of the source populations is scaled based on empirical data. This procedure uses the assumption that the relative orbit distributions from a source population are approximately correct, but the numbers of objects need to be adjusted to match the measurements. Note that this assumption was confirmed at multiple steps in the fitting process. This means that the entire source model sub-population is scaled up or down together to match the data and establish the final ORDEM populations.

The orbital density in a specific orbit bin is given by

$$n_{sdi} = c_{sd} \sum_k \frac{Y_{sdik} w_{sdik}}{V_i} \quad 4.1-1$$

where the index “*s*” refers to a size range, “*d*” refers to a material density type, “*i*” is the orbit bin, and “*k*” is the individual object from the source model. The coefficient c_{sd} is the empirical scaling factor, which is only a function of the size *s* and density *d* and is applied across each orbit bin *i*. The term V_i is the “volume” of the orbit bin *i* (to compute density), w_{sdik} is the individual weighting from the source model for object *k* with size *s* and density *d* that contributes to orbit bin *i*, and Y is a proportionality constant that represents the actual number of objects in the population to which that sample corresponds. The properties of Y are discussed below and in Section 4.1.2. The resulting quantity n_{sdi} is the population density in bin *i* of size range *s* and density *d*.

The flux in “igloo” element “*j*” is a linear combination of the individual orbit densities using the mapping matrix “ h_{ji} ”

$$f_{jsd} = \sum_i h_{ji} n_{sdi} = c_{sd} \sum_i h_{ji} \sum_k \frac{Y_{sdik} w_{sdik}}{V_i}. \quad 4.1-2$$

Temporarily neglecting the size and density “*sd*” terms, and concentrating on a single size and density contribution to the flux gives:

$$f_j = \sum_i h_{ji} n_i = c \sum_i h_{ji} \sum_k \frac{Y_{ik} w_{ik}}{V_i}. \quad 4.1-3$$

A first-order estimate of the uncertainty in the flux element is obtained by the linear expansion of the uncertainty

$$\sigma_{f_j}^2 \approx \left(\frac{\partial f_j}{\partial c} \right)^2 \sigma_c^2 + \sum_i \left(\frac{\partial f_j}{\partial h_{ji}} \right)^2 \sigma_{h_{ji}}^2 + \sum_i \sum_k \left(\frac{\partial f_j}{\partial Y_{ik}} \right)^2 \sigma_{Y_{ik}}^2. \quad 4.1-4$$

Note that there is assumed to be no uncertainty for the error in V_i or the weighting terms w_{ik} . Also, the covariant terms (the “cross-terms”) are assumed to be unimportant. The first term indicates that the whole flux varies proportional to the error in the total empirical scaling factor. The second term is the numerical

error in the mapping matrix. The last term is due to the finite nature of the model population used to estimate the orbit distributions.

This equation reduces to

$$\sigma_{f_j}^2 \approx \left(\sum_i h_{ji} \sum_k \frac{Y_{ik} w_{ik}}{V_i} \right)^2 \sigma_c^2 + \sum_i \left(c \sum_k \frac{Y_{ik} w_{ik}}{V_i} \right)^2 \sigma_{h_{ji}}^2 + \sum_i \sum_k \left(\frac{c h_{ji} w_{ik}}{V_i} \right)^2 \sigma_{Y_{ik}}^2 \quad 4.1-5$$

$$\approx \left(\frac{\sigma_c}{c} \right)^2 \left(c \sum_i h_{ji} \sum_k \frac{Y_{ik} w_{ik}}{V_i} \right)^2 + \sum_i \sigma_{h_{ji}}^2 \left(c \sum_k \frac{Y_{ik} w_{ik}}{V_i} \right)^2 + \sum_i \sum_k \left(\frac{c h_{ji} w_{ik}}{V_i} \right)^2 \sigma_{Y_{ik}}^2 \quad 4.1-6$$

$$\approx \left(\frac{\sigma_c}{c} \right)^2 (f_j)^2 + \sum_i \sigma_{h_{ji}}^2 \left(c \sum_k \frac{Y_{ik} w_{ik}}{V_i} \right)^2 + \sum_i \left(\frac{c h_{ji}}{V_i} \right)^2 \sum_k w_{ik}^2 \sigma_{Y_{ik}}^2 \quad 4.1-7$$

Note that the first term indicates that the total flux is proportionally related to the uncertainty in the empirical adjustment term. The last term is the uncertainty due to the finite sampling nature of the source model, *i.e.*, the source model is composed of sample orbits with a finite number of members. This means that the actual sample orbits chosen that fit into orbit bin i are determined by random Poisson/binomial sampling. In such cases, the mean value and uncertainty due to each sample can be approximated by (see Section 4.1.2):

$$\langle Y_{ik} \rangle \approx 1 \quad 4.1-8$$

and

$$\sigma_{Y_{ik}} \approx 1. \quad 4.1-9$$

Inserting these values into the estimated flux uncertainty, the Y_{ik} terms disappear, leaving

$$\sigma_{f_j}^2 \approx \left(\frac{\sigma_c}{c} \right)^2 (f_j)^2 + \sum_i \sigma_{h_{ji}}^2 n_i^2 + \sum_i h_{ji}^2 \sum_k \left(\frac{c}{V_i} \right)^2 w_{ik}^2. \quad 4.1-10$$

For the last term, the random, uncorrelated error for the computation of orbit population element n_i (the “ran sigma”) is defined as

$$(\sigma_{n_i}^{ran})^2 \approx \sum_k \left(\frac{c}{V_i} \right)^2 w_{ik}^2 \quad 4.1-11$$

giving

$$\sigma_{f_j}^2 \approx \left(\frac{\sigma_c}{c} \right)^2 f_j^2 + \sum_i \sigma_{h_{ji}}^2 n_i^2 + \sum_i h_{ji}^2 (\sigma_{n_i}^{ran})^2. \quad 4.1-12$$

The first term is named the “correlated error” and applies across the entire sub-population in size and material density. The second and third terms are “uncorrelated errors” – random errors that sum as the square root of the sum of the squares.

Each population is stored in the ORDEM software with two “sigma” values, the “pop sigma,” representing the correlated errors, and the “ran sigma,” representing the uncorrelated errors. In actual implementation in the ORDEM code, the construction of the populations introduces other errors. However, these errors are folded in by assigning them to either of the two error categories for propagation.

The process that fits the source populations to the data not only gives the proportionality constant c , but the uncertainty in that value, σ_c . The “pop sigma” values are computed and stored as

$$\sigma_{n_i}^{pop} \approx \sum_k \frac{\sigma_c Y_{ik} w_{ik}}{V_i} = \frac{\sigma_c}{c} n_i. \quad 4.1-13$$

The flux uncertainty can be computed using

$$\sigma_{f_j}^2 \approx \left(\sum_i h_{ji} \sigma_{n_i}^{pop} \right)^2 + \sum_i \sigma_{h_{ji}}^2 n_i^2 + \sum_i h_{ji}^2 (\sigma_{n_i}^{ran})^2. \quad 4.1-14$$

Combining the fluxes from each igloo element is accomplished by bookkeeping the “correlated” and “uncorrelated” errors separately:

$$\sigma_{f_j}^2 \approx \left(\sigma_{f_j}^{corr} \right)^2 + \left(\sigma_{f_j}^{uncorr} \right)^2 \quad 4.1-15$$

where

$$\sigma_{f_j}^{corr} = \sum_i h_{ji} \sigma_{n_i}^{pop} \quad 4.1-16$$

and

$$\sigma_{f_j}^{uncorr} = \sqrt{\sum_i \sigma_{h_{ji}}^2 n_i^2 + \sum_i h_{ji}^2 (\sigma_{n_i}^{ran})^2}. \quad 4.1-17$$

4.1.1 Composite Fluxes

Consider the flux on a surface α determined by a mapping matrix $g_{\alpha j}$ (the total flux is just a special case of this formulation):

$$f_\alpha = \sum_j g_{\alpha j} f_j = \sum_j g_{\alpha j} \sum_i h_{ji} n_i = \sum_j g_{\alpha j} \sum_i h_{ji} \sum_k \frac{c Y_{ik} w_{ik}}{V_i}. \quad 4.1-18$$

The estimated uncertainty in this composite flux would be

$$\sigma_{f_\alpha}^2 \approx \left(\frac{\partial f_\alpha}{\partial c} \right)^2 \sigma_c^2 + \sum_j \sum_i \left(\frac{\partial f_\alpha}{\partial h_{ji}} \right)^2 \sigma_{h_{ji}}^2 + \sum_i \sum_k \left(\frac{\partial f_\alpha}{\partial Y_{ik}} \right)^2 \sigma_{Y_{ik}}^2 \quad 4.1-19$$

$$\approx \left(\frac{f_\alpha}{c} \right)^2 \sigma_c^2 + \sum_j \sum_i \left(g_{\alpha j} \sum_k \frac{c Y_{ik} w_{ik}}{V_i} \right)^2 \sigma_{h_{ji}}^2 + \sum_i \sum_k \left(\sum_j g_{\alpha j} h_{ji} \frac{c w_{ik}}{V_i} \right)^2 \sigma_{Y_{ik}}^2 \quad 4.1-20$$

$$\approx \left(\frac{f_\alpha}{c} \right)^2 \sigma_c^2 + \sum_j g_{\alpha j}^2 \sum_i \left(\sigma_{h_{ji}} n_i \right)^2 + \sum_i \sum_k \left(\sum_j g_{\alpha j} h_{ji} \frac{c w_{ik}}{V_i} \right)^2 \quad 4.1-21$$

Unfortunately, the last term, which represents how random errors in each population bin are correlated across different igloo bins, is not trivial to propagate using ORDEM because of the large number of population bins. Fortunately, in ORDEM this term is quite small (relative to the first term), due to the large number of source populations used. Instead, the following approximation is used:

$$\sum_i \sum_k \left(\sum_j g_{\alpha j} h_{ji} \frac{c Y_{ik} w_{ik}}{V_i} \right)^2 \approx \sum_j g_{\alpha j}^2 \sum_i (h_{ji} \sigma_{n_i}^{ran})^2. \quad 4.1-22$$

This reduces the composite uncertainty to

$$\sigma_{f_\alpha}^2 \approx \left(\frac{f_\alpha}{c} \right)^2 \sigma_c^2 + \sum_j g_{\alpha j}^2 \sum_i (\sigma_{h_{ji}} n_i)^2 + \sum_j g_{\alpha j}^2 \sum_i (h_{ji} \sigma_{n_i}^{ran})^2. \quad 4.1-23$$

For the first term

$$\left(\frac{f_\alpha}{c} \right)^2 \sigma_c^2 = \left(\sum_j g_{\alpha j} f_j \frac{\sigma_c}{c} \right)^2 = \left(\sum_j g_{\alpha j} \sum_i h_{ji} n_i \frac{\sigma_c}{c} \right)^2 \quad 4.1-24$$

$$= \left(\sum_j g_{\alpha j} \sum_i h_{ji} \sigma_{n_i}^{pop} \right)^2 = \left(\sum_j g_{\alpha j} \sigma_{f_j}^{corr} \right)^2. \quad 4.1-25$$

This gives

$$\sigma_{f_\alpha}^2 \approx \left(\sum_j g_{\alpha j} \sigma_{f_j}^{corr} \right)^2 + \sum_j g_{\alpha j}^2 (\sigma_{f_j}^{uncorr})^2. \quad 4.1-26$$

This is the method by which the output “correlated” and “uncorrelated” fluxes are combined, at least for a given size and density class.

When combining fluxes from different density classes, they are treated as uncorrelated. This is an approximation that yields good results. Therefore, for a total flux at a given size, summed over all igloo bins and density families,

$$f_{tot} = \sum_d f_d = \sum_d \left(\sum_j f_{jd} \right) \quad 4.1-27$$

the uncertainty can be approximated as

$$\sigma_{f_{tot}}^2 \approx \sum_d \sigma_{f_d}^2 = \sum_d \left(\left(\sum_j \sigma_{f_{jd}}^{corr} \right)^2 + \sum_j (\sigma_{f_{jd}}^{uncorr})^2 \right). \quad 4.1-28$$

Note again that the “correlated” uncertainties are summed, then squared. The “uncorrelated” uncertainties are squared, then summed.

4.1.2 Uncertainty, Proportionality Constant

To compute the values associated with the Y terms, consider a count composed of the sum of various Poisson samples with weightings w_p , such that the sum s is

$$s = \sum_p w_p. \quad 4.1-29$$

Each Poisson sample w_p represents some unknown number of actual objects that can be represented as $Y_p w_p$, where the mean value is

$$\langle Y_p w_p \rangle = w_p \quad 4.1-30$$

and the mean value of the proportionality term Y_p is

$$\langle Y_p \rangle = 1. \quad 4.1-31$$

Consider an estimate of the true population represented by the weighted Poisson samples

$$s = \sum_p Y_p w_p. \quad 4.1-32$$

The mean value of the estimated population the Poisson samples were taken from will be

$$\langle s \rangle = \sum_p \langle Y_p \rangle w_p = \sum_p w_p. \quad 4.1-33$$

For the uncertainty calculation, the value of w_p is a model parameter and has no uncertainty. The uncertainty of the population from which these Poisson samples were taken is then

$$\sigma_s^2 \approx \sum_p \left(\frac{\partial s}{\partial Y_p} \right)^2 \sigma_{Y_p}^2 \approx \sum_p w_p^2 \sigma_{Y_p}^2. \quad 4.1-34$$

To find the value of the standard deviation of the Y_p terms, consider the case with a set of N_α identical w_a values. Because each sample is identical, the σ_{Y_α} values will also be identical:

$$\sigma_{s_\alpha}^2 \approx N_\alpha w_a^2 \sigma_{Y_\alpha}^2. \quad 4.1-35$$

However, this is a straightforward, scaled Poisson problem, where the value of the standard deviation is known

$$\sigma_{s_\alpha} \approx \sqrt{N_\alpha} w_a. \quad 4.1-36$$

So, the correct value of the standard deviation of Y_a is

$$\sigma_{Y_\alpha} \approx 1 \quad 4.1-37$$

Next, consider the case of the sum of two weighted populations, α and β , such that

$$\sigma_s^2 \approx N_\alpha w_\alpha^2 \sigma_{Y_\alpha}^2 + N_\beta w_\beta^2 \sigma_{Y_\beta}^2 \approx \sigma_{s_\alpha}^2 + \sigma_{s_\beta}^2 \quad 4.1-38$$

This is simply the combination (the sum of the squares) of two scaled, Poisson problems

$$\sigma_{s_\alpha}^2 + \sigma_{s_\beta}^2 \approx N_\alpha w_\alpha^2 + N_\beta w_\beta^2 \quad 4.1-39$$

Consequently, the values of the σ_Y terms can be determined for the general case

$$\sigma_{Y_\alpha} \approx \sigma_{Y_\beta} \approx \sigma_{Y_p} \approx \sigma_Y \approx 1 \quad 4.1-40$$

and for the mean terms:

$$\langle Y_\alpha \rangle \approx \langle Y_\beta \rangle \approx \langle Y_j \rangle \approx \langle Y \rangle \approx 1. \quad 4.1-41$$

This means that, in general, the uncertainty in the population estimate from which a series of Poisson samples with different weights are sampled will be

$$\sigma_s^2 \approx \sum_p \left(\frac{\partial s}{\partial Y_p} \right)^2 \sigma_{Y_p}^2 \approx \sum_p w_p^2 \sigma_{Y_p}^2 \approx \sum_p w_p^2. \quad 4.1-42$$

Another way to understand this is the contribution from a single, Poisson weighted sample will be proportional to N and the standard deviation will be proportional to $N^{1/2}$, where N in both cases equals 1.

4.2 Radar-Scaled LEGEND Population

The range of possible future OD environments is sampled from the LEGEND MC simulations based on a set of assumptions, such as solar flux and launch behaviors. Most MC runs show a modest steady growth rate in the number of debris, while a few will predict one or more large breakups, with sudden sharp increases in number of objects and flux for a given year. It is prudent to construct the models to accurately reflect the range of possible future outcomes. For example, it is widely recognized that future solar activity has a strong effect on the future evolution of debris. However, only the gross behavior of the 11-year cycle of solar activity can be predicted. It is not known if any particular future cycle will be high or low (Matney, 2005). The range or spread of possible future flux values is folded into the model's "correlated" (population) uncertainties.

For a given year, the number of objects in the reference populations are grouped according to the orbit-parameter binning scheme (non-GEO: perigee, eccentricity, inclination; GEO: mean motion, inclination, eccentricity, and RAAN), and then broken out into density classes (low, medium, high, and intact) and evenly distributed size bins. This results in a weighting (*i.e.*, number of objects) per perigee/eccentricity/inclination/density/size group for each MC run. Computing the standard deviation, or "spread," of the future environment is straightforward:

$$s = \sqrt{\frac{1}{N-1} \sum_{i=1}^N (x_i - \bar{x})^2} \quad 4.2-1$$

where s is the standard deviation, N is the total number of MCs, x_i is the weighting for a given MC run, and \bar{x} is the average of all MCs per perigee/eccentricity/inclination/density/size group. Uncertainties in the number of objects in the model populations also take into account the model parameter estimations (weighted averages) described in Section 3.1.4.2.

4.3 Degradation Population

For the degradation model, the “pop sigma” component of the sigma was estimated via MC methods using four primary steps:

1. The observational data counts were altered by randomly reassigning unknown impacts, proportionate to known impacts of MD, HD, and MMs for the windows (Section 3.2.2). For the radiator perforations, all unknowns were assigned to the MD category.
2. The resampled observational data from step 1 was fitted using a Maximum Likelihood Estimation procedure (Section 3.2.5) by adjusting the size-dependent scale factors for the debris population (equivalent to adjusting the production rates) using a cubic polynomial to describe the log-log distribution in size (Section 3.2.5).
3. A parametric bootstrap procedure (Efron & Tibshirani, 1993) was applied to these fitted functions. The re-estimated scale factors and basis populations from step 2 were used to compute the predicted number of features in each feature size bin. New “data” were sampled by using these predictions as the expectation value for a Poisson sampler. These Poisson draws model a random sample from such a distribution.
4. Like step 2, new scale factors were again re-estimated using Maximum Likelihood Estimation, with the newly simulated observational data counts from step 3 used as the observational data.

The four steps were repeated N times to create N estimates of population scale factor vs. particle size based on simulated measurement counts (from step 4). These constitute a large sample from which a sample mean and variance can be computed to provide a measure of uncertainty in the estimated model parameters. The advantage of this process is that it accounts for uncertainty due to the random assignment of unknown impacts (step 1) and estimation uncertainty from the choice of model. The square root of the sample variance models the “pop sigma” component as a function of sample size according to

$$s = \sqrt{\frac{1}{N-1} \sum_{i=1}^N (x_i - \bar{x})^2} \quad 4.3-1$$

where x_i is a scaling estimate for the i -th estimate based on simulated data, and N is 10,000 for ORDEM 3.1.

4.4 GEO Population

A population uncertainty was applied for both historical and future GEO populations as a measure of the inherent uncertainty in the observed number of GEO objects. The GEO component built from the MODEST composite dataset includes uncertainties from optical measurements. Specifically, these uncertainties result from variations in the instrumental magnitude used to calculate one absolute magnitude for an individual target as well as an assumed albedo, phase function, and range required to convert absolute magnitude to size. The instrumental magnitude for a given UCT can vary by approximately 0.5, which provides one set of lower and upper size bounds for a given target. For the assumed albedo in the conversion of absolute magnitude to size, a lower bound of 0.13 (Mulrooney and Matney, 2007) was used to provide a second upper size estimate for OD given the magnitude-to-size conversion. An additional, lower size estimate was determined assuming an albedo of 0.2, which is often

used for payloads and rocket bodies (Shell, 2010). Using these uncertainties, a range in the resulting cumulative size distribution of MODEST detections was determined, shown in Figure 4-2. The instrumental magnitude variations yield a wider range of possible objects than the albedo variations.

Based on these results, a size-dependent, population uncertainty was applied to the GEO populations. A general 10% population uncertainty was assumed as part of the population uncertainties for all sizes. For objects smaller than approximately 1 m (contributed by the MODEST dataset), an additional uncertainty was added to bound the spread in the expected number of objects for a given size and larger, based on variations in the instrumental magnitudes, σ_{mag} . The total resulting uncertainty in the cumulative number of objects for the GEO population (dashed black curves in Figure 4-2) is $\sqrt{(0.1)^2 + (\sigma_{mag})^2} \cdot \bar{x}$, where \bar{x} is the mean number of objects for a given size and larger, taking into account the object weights as discussed in Section 3.3.

In addition to the optical measurement uncertainties, the spread of possible future flux values based on the standard deviation, s , from the MC simulations is also folded into the model's population uncertainties for future populations, similar to the radar-scaled LEGEND population (Section 4.2). The overall GEO population error, $\sigma_{pop_{GEO}}$, is then given by

$$\sigma_{pop_{GEO}} = \sqrt{s^2 + (0.1\bar{x})^2 + (\sigma_{mag}\bar{x})^2}. \quad 4.4-1$$

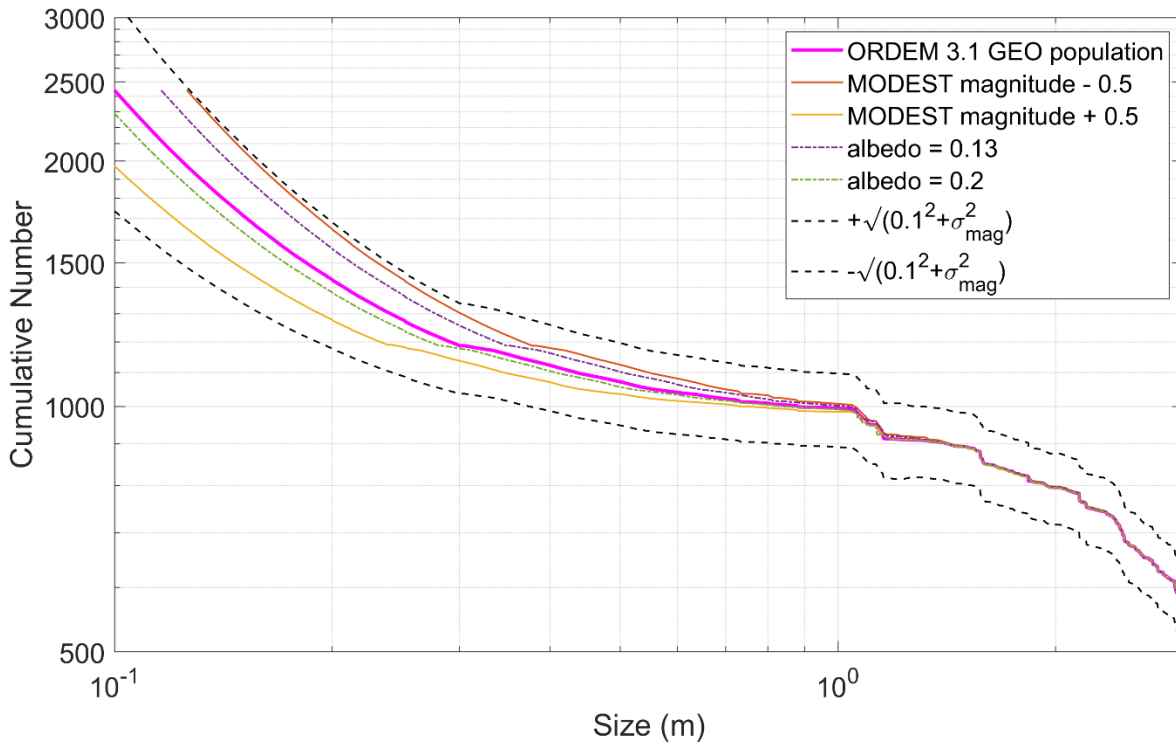


Figure 4-2. Uncertainties for the ORDEM 3.1 GEO populations based on variations in instrumental magnitude and assumed albedo for converting magnitude to size. The total population uncertainty assumed for the GEO populations is given by the dashed black curves.

4.5 Upper and Lower Sigma Bounds for Flux vs. Size

In the ORDEM 3.1 software graphical user interface (GUI), the plot “Average Flux vs. Size” in spacecraft mode represents the average cumulative flux as a function of particle size (see Vavrin, *et al.*, 2019). Because of the dynamic range of the uncertainties as a function of size (from a few percentages to a factor of two or more), the upper and lower sigma bounds (*i.e.*, “+SIGMA” and “-SIGMA” columns, respectively, in the “SIZEFLUX_SC.OUT” output file) are computed based on a log-normal distribution. The log-normal distribution ensures that the lower limits remain non-zero and that the extent of the upper and lower errorbars are proportionally more accurate, especially for large sigma values. In addition, the log-normal distributions better capture the nature of the uncertainties estimated by the fitting processes.

Let μ' and σ' represent the average (linear) flux and the (linear) standard deviation, respectively, from a given spacecraft mode run. The log-normal median m and standard deviation s can be calculated as:

$$m = \ln\left(\frac{\mu'^2}{\sqrt{\mu'^2 + \sigma'^2}}\right), \quad s = \sqrt{\ln\left(\frac{\mu'^2 + \sigma'^2}{\mu'^2}\right)}. \quad 4.5-1$$

The above expressions for m and s are then used to calculate σ_{Δ}^{\pm} , the log-normal upper- and lower-sigma bounds:

$$\sigma_{\Delta}^{\pm} = \pm e^{(m \pm s)} \mp \mu'. \quad 4.5-2$$

Additionally, the flux calculator in the ORDEM GUI calculates interpolated upper- and lower-sigma bounds for a given j multiple of sigmas (where j is a user-defined parameter on a $-3 \cdot \sigma < j \cdot \sigma < 3 \cdot \sigma$ scale). Using μ' , σ_{Δ}^{\pm} , and j , the resulting upper/lower bounds are defined as $\sigma_{j\Delta}^{+}$, $\sigma_{j\Delta}^{-}$, respectively:

$$\sigma_{j\Delta}^{+} = (\sigma_{\Delta}^{+} - \mu') \cdot \left(\frac{\mu' + \sigma_{\Delta}^{+}}{\mu' - \sigma_{\Delta}^{-}}\right)^{\frac{j-1}{2}} - \mu' \quad 4.5-3$$

$$\sigma_{j\Delta}^{-} = \mu' - (\mu' - \sigma_{\Delta}^{-}) \cdot \left(\frac{\mu' - \sigma_{\Delta}^{-}}{\mu' + \sigma_{\Delta}^{+}}\right)^{\frac{j-1}{2}}. \quad 4.5-4$$

5.0 ORDEM INTERPOLATION APPROACH

5.1 Background

When publicly released, ORDEM 3.0 introduced many new capabilities and features as it supplanted its predecessor model, ORDEM2000; however, a subtle feature is the method of interpolating between the 11 reference points distributed in half-decade intervals in $\log_{10}(\text{size})$ space between the ORDEM minimum debris size (10 μm) and its maximum size (1 m) – a total of five orders of magnitude in debris characteristic size. Orbital debris flux varies by many orders of magnitude as a function of size, and the standard way to handle this dynamic distribution is to interpolate the log-log distribution, *i.e.*, $\log_{10}(\text{flux})$ as a function of $\log_{10}(\text{size})$.

A fundamental representation of the debris number or flux is to give the value for a given size or larger. This cumulative distribution dates to the earliest days of MM and OD studies, under the assumption that if an object of a certain size poses a penetration risk to a target spacecraft, *i.e.*, the critical diameter, then all larger sizes pose that same penetration risk. While interpolation may seem cosmetic in nature when applied to the entire cumulative flux vs. size curve, in which all half-decades are filled to some degree, it

is crucially important when determining the flux corresponding to the estimated critical diameter for a given ORDEM subpopulation at a given orientation and relative velocity with respect to a target. This is a requirement for using ORDEM outputs in risk estimation codes such as NASA's Bumper series of codes for MMOD risk assessment, managed by the HVIT team (Lear, *et al.*, 2019).

Thus, a robust interpolator that preserves the cumulative nature of the function is an absolute requirement. Other considerations are the ability to handle discontinuities and the representation of zero in $\log_{10}(\text{flux})$ space. An example of the former is the ORDEM LD population transition at 1 mm size. For a given bin in azimuth, elevation, and relative velocity, there may be a nonzero LD flux for sizes larger than 1 mm, but the model does not include any additional flux for smaller sizes, based on the paucity of evidence found for LD debris in examinations of the Shuttle window and radiator cratering record. This feature manifests itself as a flat line in cumulative distributions for sizes less than 1 mm for LD debris. Similarly, the azimuth-elevation-relative velocity bins for many populations have sizes where the flux drops to zero. In the half-decade between the last non-zero flux and the first zero flux, a very steep slope may be encountered, even allowing for an approximation of zero flux by a very small number in $\log_{10}(\text{flux})$ space.

Prior to ORDEM 3.0 development, interpolation schemes were developed in-house by the ODPO. During the development of ORDEM 3.0, however, the government off-the-shelf software embodied in the Piecewise Cubic Hermite Interpolating Polynomial (PCHIP) package, developed by the U.S. Department of Energy (DOE) Energy Science & Technology Software Center (ESTSC), was chosen for implementation in ORDEM 3.0 (Fritsch, 1982). Among the reasons motivating this choice was that PCHIP was a robust, validated code, met all numerical requirements in handling cumulative data sets and error case handling, and could be distributed bundled with the ORDEM 3.0 executable package. For both ORDEM 3.0 and 3.1, the PCHIP Fortran-language software has been implemented as ORDEM subroutine interface-compatible code, licensed, and bundled with the ORDEM installer package. Note that while other publicly-available PCHIP implementations exist, they have not been compared to the DOE-ESTSC software distribution and no endorsement is implied.

The PCHIP code and its component subroutines are predicated upon evaluating a piecewise cubic Hermite function at an array of points; the cubic polynomial is determined by n function values (F_1, F_2, \dots, F_n) and internally-computed numerical derivatives (D_1, D_2, \dots, D_n) over the interval (X_1, X_n) at m user-defined points contained in the array XE . The interpolated functional points are output in the array FE . Fritsch and Butland, 1984 and Fritsch and Carlson, 1980 provide details of the code's fundamental mathematical formalisms and general design and error handling.

PCHIP performance for a challenging data set is portrayed in Figure 5-1, where the interpolator handles the transitions between flat sections (size ranges with no modeled populations) and size ranges with rapidly-varying flux. Following PCHIP implementation in the ORDEM 3.0 release package, the NASA Bumper code was modified to use an equivalent, publicly-available version of the PCHIP interpolator and its implementation was verified.

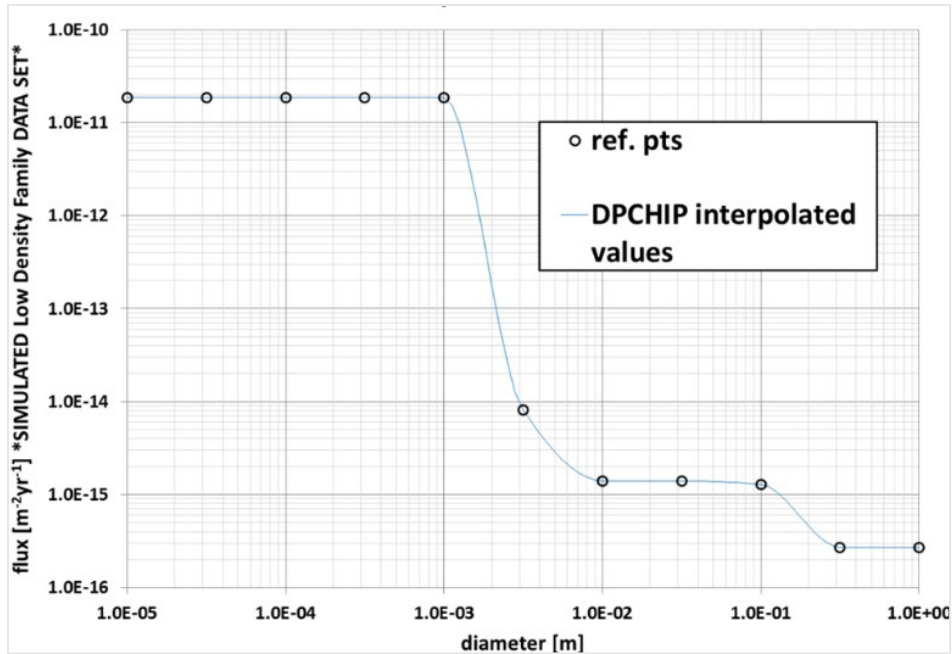


Figure 5-1. PCHIP implementation for a challenging, simulated LD data set, indicated by 11 half-decadal reference points in $\log_{10}(\text{size})$ space. Five hundred interpolated points provide a smoothly interpolated curve over this data set.

Figure 5-2 illustrates the critical function of PCHIP – interpolating a flux associated with a critical diameter – for ORDEM subpopulations. In this example, the 2019 flux on a spacecraft in an 841 x 856 km altitude, 98.8° inclination orbit is portrayed by solid or open markers (11 reference points per subpopulation) and 101 points over 5 size decades were interpolated and represented in Figure 5-2 by solid or dotted lines. Critical diameters for penetration of an aluminum Whipple shield (Christiansen, 1991) are indicated by heavy open circles for the LD, MD, HD, NaK, and Intact populations (note that this latter population is only modeled down to 10 cm characteristic lengths and represents the cataloged, on-orbit intact population). This set of five subpopulations is drawn from the ORDEM output for a single case of azimuth, elevation, and relative velocity with respect to the target spacecraft. Note that critical diameters vary by the mass density attributed to each of the five subpopulations, but all critical diameters are located between two reference points, such that interpolation between these points is required to assess the subpopulation flux. For this evaluation, nominal mass densities of 0.9, 1.4, 2.8, 7.9, and 2.8 g/cm³ were used for the NaK, LD, MD, HD, and Intact families, respectively. Note also that in the half decade between the last non-zero flux value and the first significant zero, the ORDEM 3.0 implementation of the PCHIP tool added 8 additional reference points, in addition to the 11 reference points produced by ORDEM, to steer the distribution; these may be seen for the HD and NaK subpopulations in the half-decade between 3.16 and 10.0 cm.

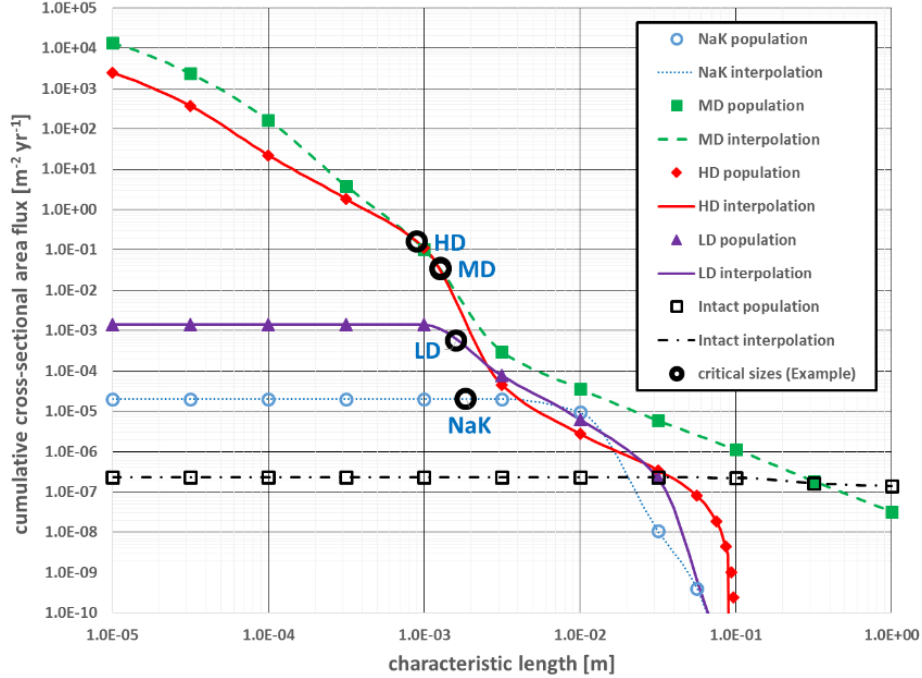


Figure 5-2. PCHIP interpolation of ORDEM subpopulations, with critical diameters required to penetrate an aluminum Whipple bumper indicated. Interpolation is required to assess the subpopulation flux at the computed critical diameters. Critical diameters vary according to mass density of the debris projectile. The intact population, used to represent the satellite catalog, terminates at 10 cm while the LD population (as in Figure 5-1) terminates at 1 mm. See text for specifics of the target orbit for this example.

After the release of ORDEM 3.0, concerns arose over risk estimates that used interpolators other than PCHIP to estimate critical diameters in ORDEM subpopulations. This outcome is most common when comparing Bumper results to results generated by other risk estimators, for example ESABASE (Miller, 2017). This is not a surprising outcome, particularly when critical diameters reside in portions of the flux curve with large gradients. Two different interpolation schemes are likely to produce dissimilar results, particularly in dynamic regions.

A difference also had been noted in comparisons between the output of the released version of ORDEM 3.0 and Bumper 3. While ORDEM 3.0 summed the 5 ORDEM subpopulations at the 11 reference points, then interpolated, Bumper 3 interpolates the fluxes for each subpopulation for a given azimuth, elevation, and relative velocity separately, then sums. In certain size regimes, differences can be significant. The Bumper 3 procedure is considered the correct one, and ORDEM 3.1 rectifies this difference by interpolating the subpopulations and then summing the results in the manner of Bumper 3. In addition, the legacy steering function was removed for ORDEM 3.1 due to the robust nature of the PCHIP interpolator. This general function was a legacy of prior interpolation functions used by ORDEM2000 and introduced, albeit in a different form, in ORDEM 3.0, but is not considered necessary.

5.2 Scope of the ORDEM 3.1 Interpolation

The ORDEM 3.1 interpolation code, as outlined, is applied to ORDEM 3.1 subpopulations resident in ORDEM 3.1 and data files produced as output by ORDEM, specifically the “IGLOOFLUX_SC.OUT” output file. This file gives the cumulative fluxes at the 11 reference points for all 5 density families and each azimuth, elevation, and relative velocity bin in the target spacecraft frame. The interpolated-then-summed fluxes, summed over all density families and azimuth, elevation, and relative velocity bins, are given in the “SIZEFLUX_SC.OUT” output file.

5.3 ORDEM Interpolation General Conditions

The ORDEM 3.X output consists of cumulative cross-sectional area flux values spanning up to five decades in debris characteristic length (size). Therefore, all interpolations are conducted in $[\log_{10}(\text{size}), \log_{10}(\text{flux})]$ space. The presence of one or more zero values for flux is handled by abstracting zero as a number on the order of machine single-precision real values; in ORDEM, a value of 1×10^{-30} , or -30.0 in \log_{10} space, represents a zero-equivalent flux. Once interpolated values are returned by the PCHIP subroutine, the *XE* and *FE* arrays are converted from \log_{10} space to linear space.

For IGLOOFLUX_SC elements with non-zero cumulative flux F_i , one or more F_i may be zero. In this case, the last significant half-decade is defined as the last half-decade in size containing a non-zero flux. This definition is equivalent to noting that the i -th half-decade in size with $F_i \neq 0.0$ and $F_{i+1} = 0.0$ (in linear space) is the last significant half-decade in size. In this case, F_{i+1} represents a significant zero and all F_j for $j > i + 1$ are considered non-significant. With the removal of the steering function for ORDEM 3.1, non-significant zero fluxes are ignored for the purpose of interpolation. That is, interpolation is performed using the fluxes only up to and including the first significant zero.

5.4 PCHIP Implementation in ORDEM 3.1

As noted in Section 5.1, there exist significant differences between the ORDEM 3.0 and ORDEM 3.1 implementations, particularly related to input data handling. These differences are summarized in Table 5-1.

Table 5-1. Differentiating features of the PCHIP interpolation routine in ORDEM 3.1 as compared to ORDEM 3.0

ORDEM 3.0	ORDEM 3.1
Employed quadratic “steering function,” a function of slope in penultimate half-decade	“Steering function” deleted. Result: No pre-processing necessary for risk estimation codes
Additional eight (8) points in (size, flux) space, for a total of 19 points, defined by the steering function in the last significant half-decade	No additional points; PCHIP operates on ORDEM’s 11 (size, flux) reference points only, up to and including the last significant zero (when applicable). Result: No pre-processing necessary for risk estimation codes
Flux from the five density families added, then interpolated to produce ORDEM’s SIZEFLUX_SC.OUT output flux	Flux for each of the five density families interpolated, then added to produce ORDEM’s SIZEFLUX_SC.OUT flux. Result: ORDEM 3.1 is consistent with Bumper methodology and order of operations

The consequences of removing the so-called “steering function” are illustrated in Figure 5-3. In this example, ORDEM 3.0 and ORDEM 3.1 results for a typical ISS orbit (400 x 400 km altitude, 51.6° inclination, random RAAN and argument of perigee) in 2015 are compared for an HD flux component of the IGLOOFLUX_SC.OUT output file. In this test case, the 0.0316 m to 0.1 m size interval constitutes the last significant half-decade; zero-flux reference points at 0.316 m and 1.0 m sizes are ignored for interpolation. As is evident, a potentially dramatic difference in outcomes can occur for the identical test case in the last significant half-decade, and the ORDEM 3.1 implementation (steering function omitted) can robustly interpolate between the last non-zero flux and the significant zero in flux.

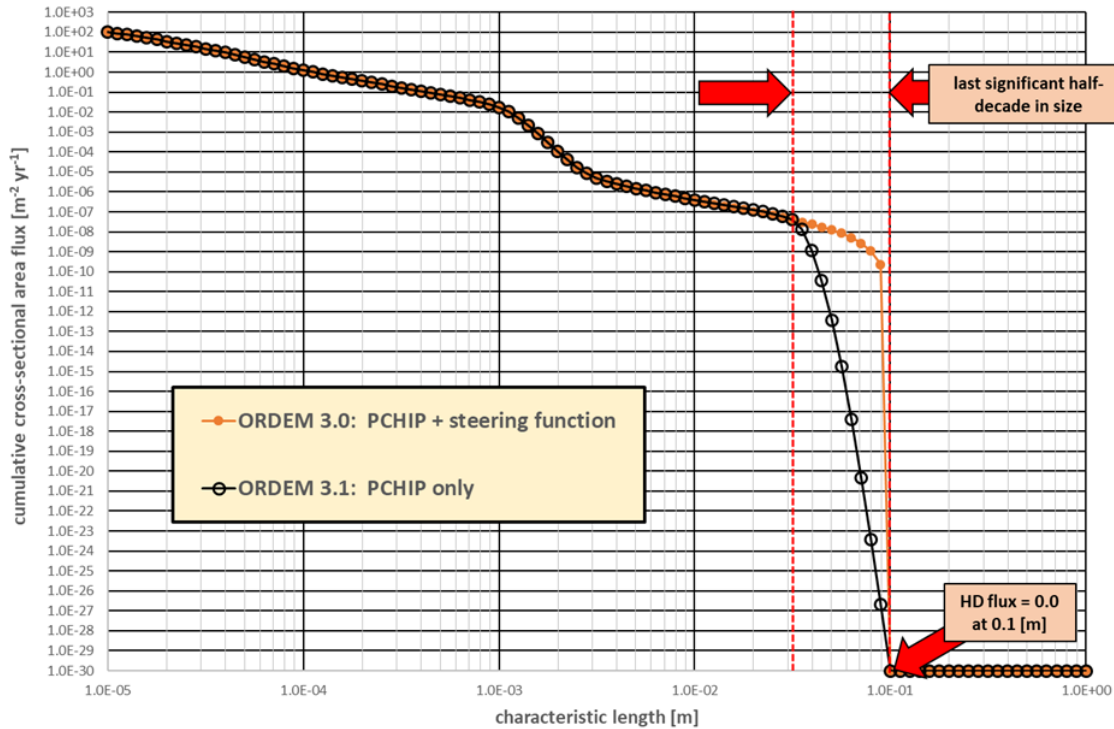


Figure 5-3. An example of interpolation with (ORDEM 3.0) and without (ORDEM 3.1) the steering function imposed on the last significant half-decade in size for the HD component of a typical ISS orbit in 2015.

Removing the steering function considerably simplifies the pre-processing of ORDEM 3.1 IGLOOFUX_SC.OUT files for applications such as Bumper 3. However, several caveats remain associated with the interpolator's implementation and use; these may be summarized as:

1. ORDEM 3.1 populations retain the half-decade resolution of ORDEM 3.0, and only these 11 points over the 5 decades of characteristic length (size) are actual point estimates of the flux for a given test configuration. In other words, only the end points (half-decade bin boundaries) are truly "known" over that half-decade's interpolation.
2. The choice of the representation of zero flux in \log_{10} space will influence outcomes in the last significant half-decade, as can be gauged from Figure 5-3.
3. Interpolating using only the first significant zero rather than all zero flux values will influence outcomes in the last significant half-decade.
4. Use of a non-PCHIP tool will yield different interpolations, causing an apparent variation in outcomes.
5. A PCHIP tool implementation with different order of operations, e.g., adding first or interpolating families first, will yield different interpolations causing an apparent variation in outcomes.

Example ORDEM 3.1 results for a typical ISS orbit in 2020, broken down by density family, are shown in Figure 5-4.

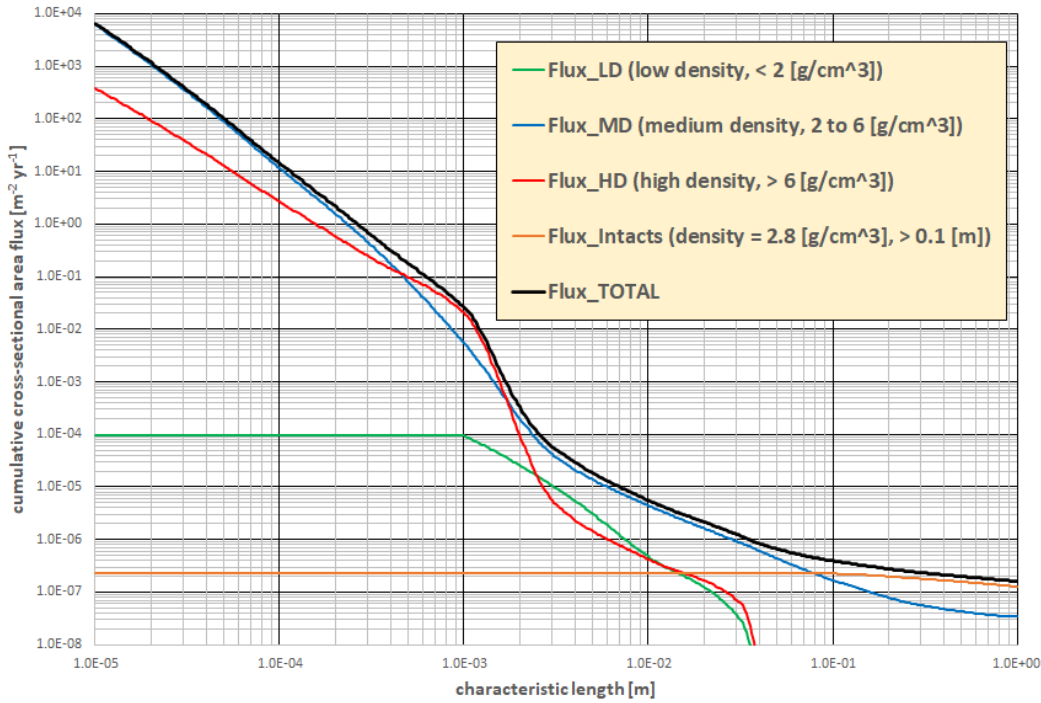


Figure 5-4. An example ORDEM 3.1 interpolation of the fluxes from the five density families for a typical ISS orbit in 2020 (the NAK family omitted due to zero flux at ISS altitudes).

In summary, the ORDEM 3.1 implementation of the DOE PCHIP interpolation package simplifies implementation and obviates the necessity of significant pre-processing for post-ORDEM application programs such as the Bumper 3 risk assessment code. Further, the order of operations in ORDEM 3.1 is now consistent with Bumper 3 as the latter's order of operations is accepted as being correct.

The implementation of a PCHIP interpolator package for ORDEM data processing is illustrated by the flow chart in Figure 5-5. Further documentation or an interface control statement is beyond the scope of this document, as various users may have unique interfaces with non-DOE PCHIP implementations.

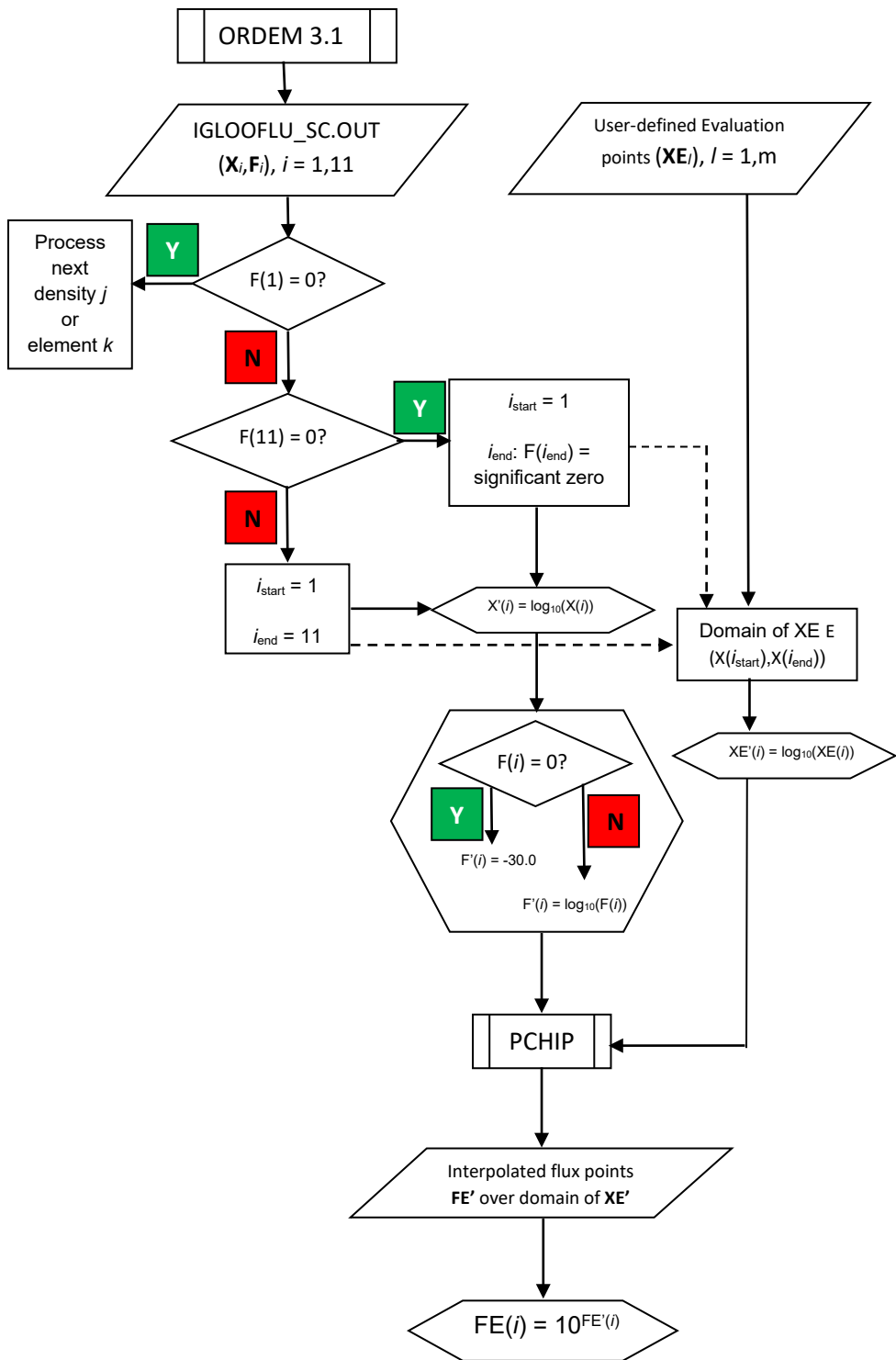


Figure 5-5. Interpolator package flow chart.

5.5 PCHIP Implementation Verification

To allow for verification of the correct implementation of the PCHIP package, example interpolation results are provided here for a typical ISS orbit (400×400 km altitude, 51.6° inclination, random RAAN and argument of perigee) for the year 2020. This orbit was processed by ORDEM 3.1.0 and the IGLOOFLUX_SC.OUT flux file was examined for cases that could present challenges to an interpolator package. Later releases of ORDEM 3.1.X (through version 3.1.2) do not affect the values presented for the low Earth orbit ISS flux. Should later revisions alter these numbers, the reference points presented herein may still be used to verify correct implementation of the PCHIP interpolator.

Specific implementation tests examined for this case's IGLOOFLUX_SC.OUT file are described in Table 5-2. The reader is encouraged to familiarize themselves with the IGLOOFLUX_SC.OUT format, as explained in the file's header. For conciseness, interpolated data covering one size decade for element 3706 is presented in Table 5-3 for the LD, MD, HD, and Intact (IN) density families. Note that the NaK family (NK as designated in the IGLOOFLUX_SC.OUT file) has been omitted since there was no flux at the ISS altitude. The remaining reference points and interpolated points, as well as the remaining test cases of Table 5-2, are presented in Appendix A. The "All" case is not a test of the PCHIP interpolator itself, but rather a "checksum"-equivalent test for the ORDEM 3.1 install and run. The test result is generated by summing the first flux values for all density families (*i.e.*, the F_1 for all density families, as these are cumulative and thereby represent the total flux for each density family for each element), then summing these to compute the total flux per square meter per year for 10 μm and larger sizes.

Table 5-2. ORDEM 3.1 PCHIP interpolation test case examples. Herein, "element" refers to the IGLOOFLUX_SC.OUT file's element number (corresponding to a specific azimuth-elevation-relative velocity bin) while "density family" refers to the specific ensemble of 11 flux values chosen for the test for the densities LD, MD, HD, and IN (Intact/cataloged objects > 10 cm size).

Element	Density Family	Behavior of Interest	Verifies
3706	HD	family with significant zero	implementation handling in last significant half-decade (101 points total, 10 μm to 1 m)
3706	LD, MD, HD, IN	all families with non-zero flux	implementation handling of interpolate-then-sum for each density family in this element (101 points total, 10 μm to 1 m)
6871	LD	LD component to 3.16 mm (last non-zero flux)	implementation handling of 1 mm discontinuity for LD component (41 points total, 316 μm to 3.16 cm)
6481	HD	HD component to 31.6 μm (last non-zero flux)	implementation handling of any two non-zero flux points (31 points total, 10 μm to 316 μm)
970	HD	HD component at 10 μm (last/only non-zero flux)	implementation handling of any one non-zero flux point (21 points total, 10 μm to 100 μm)
ALL	ALL	TOTAL 10 μm cumulative flux	ORDEM 3.1 installation and test case run yields total cumulative flux at 10 μm of 6582.543 $\text{m}^{-2} \text{yr}^{-1}$

Table 5-3. The interpolated flux for all density families, element 3706. The NK (NaK) family has been omitted since there was no flux at the ISS altitude. Both the LD and IN flux are constant within this decade (and for this case, with a non-zero modeled LD flux). Bold text indicates the three reference points in this decade: the decade boundaries and the half-decade point.

Size (m)	Low density (LD)	Medium density (MD)	High density (HD)	Intacts (IN)
1.00E-05	3.1799011E-11	1.0646572E-03	4.0246555E-05	1.9682196E-12
1.12E-05	3.1799011E-11	7.2898877E-04	3.3110197E-05	1.9682196E-12
1.26E-05	3.1799011E-11	5.0229989E-04	2.7267340E-05	1.9682196E-12
1.41E-05	3.1799011E-11	3.4836353E-04	2.2478930E-05	1.9682196E-12
1.58E-05	3.1799011E-11	2.4323485E-04	1.8550868E-05	1.9682196E-12
1.78E-05	3.1799011E-11	1.7101672E-04	1.5325424E-05	1.9682196E-12
2.00E-05	3.1799011E-11	1.2110643E-04	1.2674309E-05	1.9682196E-12
2.24E-05	3.1799011E-11	8.6398820E-05	1.0493093E-05	1.9682196E-12
2.51E-05	3.1799011E-11	6.2109290E-05	8.6966913E-06	1.9682196E-12
2.82E-05	3.1799011E-11	4.4999700E-05	7.2157227E-06	1.9682196E-12
3.16E-05	3.1799011E-11	3.2867232E-05	5.9935584E-06	1.9682196E-12
3.55E-05	3.1799011E-11	2.4224837E-05	4.9965739E-06	1.9682196E-12
3.98E-05	3.1799011E-11	1.8018025E-05	4.1864493E-06	1.9682196E-12
4.47E-05	3.1799011E-11	1.3506386E-05	3.5193201E-06	1.9682196E-12
5.01E-05	3.1799011E-11	1.0190460E-05	2.9632249E-06	1.9682196E-12
5.62E-05	3.1799011E-11	7.7287311E-06	2.4946913E-06	1.9682196E-12
6.31E-05	3.1799011E-11	5.8846332E-06	2.0963746E-06	1.9682196E-12
7.08E-05	3.1799011E-11	4.4922555E-06	1.7553927E-06	1.9682196E-12
7.94E-05	3.1799011E-11	3.4338427E-06	1.4621317E-06	1.9682196E-12
8.91E-05	3.1799011E-11	2.6248490E-06	1.2093694E-06	1.9682196E-12
1.00E-04	3.1799011E-11	2.0038871E-06	9.9161995E-07	1.9682196E-12

6.0 REFERENCES

Abercromby, K.J., Seitzer, P. E., *et al.*, Michigan Orbital DEbris Survey Telescope Observations of the Geosynchronous Orbital Debris Environment, Observing Years: 2004 – 2006, NASA/TP-2010-216129, NASA Johnson Space Center, Houston, TX, USA, 2010.

Abercromby, K.J., Seitzer, P. E., *et al.*, Michigan Orbital DEbris Survey Telescope Observations of the Geosynchronous Orbital Debris Environment, Observing Years: 2007 – 2009, NASA/TP-2011-217350, NASA Johnson Space Center, Houston, TX, USA, 2011.

Anz-Meador, P.D., Opiela, J.N., *et al.*, "History of On-orbit Satellite Fragmentations (15th Edition)," NASA/TM-2018-220037, NASA Johnson Space Center, Houston, TX, USA, 2018.

Barker, E.S., Africano, J. L., *et al.*, "Analysis of Working Assumptions in the Determination of Populations and Size Distributions of Orbital Debris from Optical Measurements," *Proceedings of the 2004 AMOS Technical Conference*, Wailea, Maui, HI, pp. 225-235, 2004.

Burt, R. and Christiansen, E., "Hypervelocity impact testing of transparent spacecraft materials," *Int. J. Impact Eng.* 29, pp. 153-166, 2003

Christiansen, E.L., Shield Sizing and Response Equations, NASA/TM-105527, NASA Johnson Space Center, Houston, TX, USA, 1991.

Efron, B. and Tibshirani, R. J., An Introduction to the Bootstrap, ISBN 0-412-04231-2, Chapman & Hall, New York, NY, 1993. Accessed online at https://cindy.informatik.uni-bremen.de/cosy/teaching/CM_2011/Eval3/pe_efron_93.pdf on 18 June 2020.

Flegel, S., Gelhaus, J., *et al.*, "Maintenance of the ESA MASTER Model," ESOC Contract No. 21705/D/HK, 2011.

Foster, J.L., Krisko, P., *et al.*, "NaK droplet source modeling," IAC-03-IAA.5.2.02, 54th International Astronautical Congress, Bremen, Germany, 2003.

Fritsch, F. N., "PCHIP Final Specifications," UCID-30194, Lawrence Livermore Laboratory under U.S. Department of Energy contract, August 1982.

Fritsch, F. N., and Butland, J., "A method for constructing local monotone piecewise cubic interpolants," *SIAM J Sci Stat Comp*, 5(2), pp. 300-304, 1984.

Fritsch, F. N., and Carlson, R. E., "Monotone piecewise cubic interpolation," *SIAM J Numer Anal*, 17(2), pp. 238-246, 1980.

Gates, D. and Matney, M., "Short-Term Satellite Breakup Risk Assessment Model Process," *Orbital Debris Quarterly News*, 24(3), pp. 7-11, August 2020.

Hill, N., Measurement Techniques for Hypervelocity Impact Test Fragments, 59th International Astronautical Congress, Glasgow, Scotland, September-October 2008.

Horstmann, A., Hesselbach, S., *et al.*, "Enhancement of S/C Fragmentation and Environment Evolution Models," ESA contract No. 4000115973/15/D/SR, 2020.

Hyde, J., Christiansen, E., and Lear, D., "Shuttle MMOD Impact Database," *Procedia Engineer.* 103, pp. 246-253, 2015.

IADC Working Group 3, "Characterization of Ejecta from HVI on Spacecraft Outer Surfaces," IADC-11-05 (April 2013). Accessed online at https://www.iadc-home.org/documents_public/view/page/3/id/107#u in February 2022.

IADC Working Group 3, "Spacecraft Component Vulnerability for Space Debris Impact," IADC-13-11 (September 2018). Accessed online at https://www.iadc-home.org/documents_public/view/page/1/id/157#u in February 2022.

Johnson, N.L., Krisko, P.H., *et al.*, "NASA's New Breakup Model of EVOLVE 4.0," *Adv. Space Res.*, 28 (9), pp. 1377-1384, 2001

Johnson, N.L. and McKnight, D.S., *Artificial Space Debris*, Orbit Book Co., Malabar, FL, 1987.

Kennedy, T., Matney, M., *et al.*, NASA Orbital Debris Engineering Model (ORDEM) 3.1: Model Verification and Validation, NASA/TP-2022-0002309, NASA Johnson Space Center, Houston, TX, USA, 2022.

Kessler, D.J. and Cour-Palais, B.G., "Collision Frequency of Artificial Satellites: The Creation of a Debris Belt", *JGR*, 83, A6, pp. 2637-2646, 1 June 1978.

Kessler, D.J., Reynolds, R.C., and Anz-Meador, P.D., Orbital Debris Environment for Spacecraft Designed to Operate in Low Earth Orbit, NASA/TM-100471, NASA Johnson Space Center, Houston, TX, USA, 1989.

Kessler, D.J., *et al.*, *Meteoroids and Orbital Debris*, in Space Station Program Natural Environment Definition for Design, NASA SSP-30425/Rev. B, NASA Johnson Space Center, Houston, TX, USA, 1994.

Kessler, D.J., Zhang, J., *et al.*, A Computer-Based Orbital Debris Environment Model for Spacecraft Design and Observation in Low Earth Orbit, NASA/TM-104825, NASA Johnson Space Center, Houston, TX, USA, 1996.

Krisko, P.H., Xu, Y.-L., *et al.*, Material Density Distribution of Small Debris in Earth Orbit, IAC-08.A6.2.1, 59th International Astronautical Congress, 2008.

Krisko, P.H., The new NASA orbital debris engineering model ORDEM 3.0, AIAA 2014-4227, 2014.

Lear, D. M., Christiansen, E. L., and Hyde, J. L., "Bumper: A Tool for Analyzing Spacecraft Micrometeoroid and Orbital Debris Risk," *Proceedings of the 15th Hypervelocity Impact Symposium*, Destin, Florida, 14-19 April 2019.

Liou, J.-C., Matney, M., *et al.*, The New NASA Orbital Debris Engineering Model ORDEM2000, NASA/TP-2002-210780, 2002.

Liou, J.-C., Hall, D.T., *et al.*, "LEGEND - a three-dimensional LEO-to-GEO debris evolutionary model," *Adv. Space Res.*, 34 (5), pp. 981-986, 2004.

Liou, J.-C., "Collision activities in the future orbital debris environment," *Adv. Space Res.*, 38, pp. 2102-2106, 2006.

Liou, J.-C., "A statistical analysis of the future debris environment," *Acta Astronaut.*, 62, pp. 264-271, 2008.

Liou, J.-C., Clark. S, *et al.*, "DEBRISAT – a planned laboratory-based satellite impact experiment for breakup fragment characterization," *Proceedings of the 6th European Conference on Space Debris*, ESA SP-723, ESA/ESOC, Darmstadt, Germany, 22-25 April 2013.

Matney, M.J., "Uncertainty in Orbital Debris Measurements and Models," *Proceedings of the 4th European Conference on Space Debris*, ESA SP-587, ESA/ESOC, Darmstadt, Germany, 18-20 April 2005.

McKnight D.S., Johnson N.L., *et al.*, Satellite orbital debris characterization impact test (SOCIT) series data collection report, NAS 9-19215, Kaman Sciences Corporation, Colorado Springs, CO, USA, 1995.

Miller, A., "ESABASE2/Debris Release 10.0 Technical Description," 2017. Accessed online at <https://esabase2.net/wp-content/uploads/2019/01/ESABASE2-Debris-Technical-Description.pdf> on 22 December 2020.

Mulrooney, M. and Matney, M., "Derivation and application of a global albedo yielding an optical brightness to physical size transformation free of systematic errors," *Proceedings of 2007 AMOS Technical Conference*, Kihei, HI, pp. 719–728, 2007.

Mulrooney, M., Matney, M., and Barker, E., A New Bond Albedo for Performing Orbital Debris Brightness to Size Transformations, IAC-08.A6.2.7, 59th International Astronautical Congress, 2008.

Murray, J., Blackwell, C., *et al.*, Haystack Ultra-Wideband Satellite Imaging Radar Measurements of the Orbital Debris Environment: 2014 – 2017, NASA/TP-2019-220302, NASA Johnson Space Center, Houston, TX, USA, 2019.

Opiela, J., "A study of the material density distribution of space debris," *Adv. Space Res.*, 43, pp. 1058-1064, 2009.

Oswald, M., Stabroth, S., *et al.*, Upgrade of the MASTER Model, included in the MASTER-2005 package, 2006.

Press, W.H., Teukolsky, S.A., *et al.*, *Numerical Recipes in Fortran 77, The Art of Scientific Computing*, 2nd ed. (Vol. 1), Cambridge University Press, 1992.

Rosengren, A.J., Scheeres, and D.J., McMahon, J.W., "The classical Laplace plane as a stable disposal orbit for geostationary satellites," *Adv. Space Res.*, 53, pp. 1219-1228, 2014.

Sdunnus, H., Bendisch, J., and Klinkrad, H. "The ESA MASTER'99 Space Debris and Meteoroid Reference Model," *Proceedings of the 3rd European Space Debris Conference*, ESA SP-473, 2001.

J.R. Shell, "Optimizing orbital debris monitoring with optical telescopes," *Proceedings of the Advanced Maui Optical and Space Surveillance Technologies Conference*, ed: S. Ryan, Wailea, Maui, Hawaii, pg. E42, 14-17 September 2010.

Stansbery, E.G., Matney, M.J., *et al.*, "A Comparison of Catastrophic On-Orbit Collisions," *Proceedings of the Advanced Maui Optical and Space Surveillance Technologies Conference*, Wailea, Maui, Hawaii, 17-19 September 2008.

Stansbery, E.G., Matney, M.J., *et al.*, NASA Orbital Debris Engineering Model ORDEM 3.0 – User's Guide, NASA/TP-2014-217370, NASA Johnson Space Center, Houston, TX, USA, 2014.

Stansbery, E.G., Matney, *et al.*, NASA Orbital Debris Engineering Model ORDEM 3.0 – Verification and Validation, NASA/TP-2015-218592, NASA Johnson Space Center, Houston, TX, USA, 2015.

Usovik, I., Stepanov, D., *et al.*, "Improvement of Space Debris Model in MEO and GEO Regions According to the Catalog of Keldysh Institute of Applied Mathematics (Russian Academy of Sciences)," *Proceedings of the 7th European Conference on Space Debris*, Darmstadt, Germany, pp. 18-21, April 2017.

Vavrin, A., Manis, A., *et al.*, NASA Orbital Debris Engineering Model ORDEM 3.1 – Software User Guide, NASA/TP-2019-220448, NASA Johnson Space Center, Houston, TX, USA, 2019.

Xu, Y.-L., Stokely, C.L., *et al.*, A statistical size estimation model for Haystack and HAX radar detections, IAC-05-B6.1.02, 56th International Astronautical Congress, 2005.

Xu, Y.-L., Statistical inference in modeling the orbital debris environment, IAC-06-B6.2.03, 57th International Astronautical Congress, 2006.

Xu, Y.-L., Horstman, M., *et al.*, "Modeling of LEO orbital debris populations for ORDEM2008," *Adv. in Space Res.*, 43, pp. 769-782, 2009.

Xu, Y.-L., Krisko, P.H., *et al.*, Modeling of the Orbital Debris Population of RORSAT Sodium-Potassium Droplets, 38th COSPAR Scientific Assembly, Bremen, Germany, pp. 18-25, July 2010(a).

Xu, Y.-L., Krisko, P.H., *et al.*, Simulation of Micron-Sized Debris Populations in Low Earth Orbit, 38th COSPAR Scientific Assembly, Bremen, Germany, pp. 18-25, July 2010(b).

A PCHIP IMPLEMENTATION VERIFICATION TEST CASES

This Appendix contains verification test case results for the cases enumerated in Section 5.5, Table 5-2.

Table A-1. The interpolated flux for element 3706. For this test case, the complete set of interpolated fluxes, 101 points covering sizes from 10 μm to 1 m, are shown for each density family (LD, MD, HD, and IN) to provide a complete reference test case. Note that the NK (NaK) density family is not shown since there is no flux at the ISS altitude. Bold text indicates the 11 reference points in this size range.

Size (m)	LD Flux	MD Flux	HD Flux	IN Flux
1.00E-05	3.1799011E-11	1.0646572E-03	4.0246555E-05	1.9682196E-12
1.12E-05	3.1799011E-11	7.2898877E-04	3.3110197E-05	1.9682196E-12
1.26E-05	3.1799011E-11	5.0229989E-04	2.7267340E-05	1.9682196E-12
1.41E-05	3.1799011E-11	3.4836353E-04	2.2478930E-05	1.9682196E-12
1.58E-05	3.1799011E-11	2.4323485E-04	1.8550868E-05	1.9682196E-12
1.78E-05	3.1799011E-11	1.7101672E-04	1.5325424E-05	1.9682196E-12
2.00E-05	3.1799011E-11	1.2110643E-04	1.2674309E-05	1.9682196E-12
2.24E-05	3.1799011E-11	8.6398820E-05	1.0493093E-05	1.9682196E-12
2.51E-05	3.1799011E-11	6.2109290E-05	8.6966913E-06	1.9682196E-12
2.82E-05	3.1799011E-11	4.4999700E-05	7.2157227E-06	1.9682196E-12
3.16E-05	3.1799011E-11	3.2867232E-05	5.9935584E-06	1.9682196E-12
3.55E-05	3.1799011E-11	2.4224837E-05	4.9965739E-06	1.9682196E-12
3.98E-05	3.1799011E-11	1.8018025E-05	4.1864493E-06	1.9682196E-12
4.47E-05	3.1799011E-11	1.3506386E-05	3.5193201E-06	1.9682196E-12
5.01E-05	3.1799011E-11	1.0190460E-05	2.9632249E-06	1.9682196E-12
5.62E-05	3.1799011E-11	7.7287311E-06	2.4946913E-06	1.9682196E-12
6.31E-05	3.1799011E-11	5.8846332E-06	2.0963746E-06	1.9682196E-12
7.08E-05	3.1799011E-11	4.4922555E-06	1.7553927E-06	1.9682196E-12
7.94E-05	3.1799011E-11	3.4338427E-06	1.4621317E-06	1.9682196E-12
8.91E-05	3.1799011E-11	2.6248490E-06	1.2093694E-06	1.9682196E-12
1.00E-04	3.1799011E-11	2.0038871E-06	9.9161995E-07	1.9682196E-12
1.12E-04	3.1799011E-11	1.5388310E-06	8.0342785E-07	1.9682196E-12
1.26E-04	3.1799011E-11	1.1949652E-06	6.4301986E-07	1.9682196E-12
1.41E-04	3.1799011E-11	9.3453273E-07	5.0970589E-07	1.9682196E-12
1.58E-04	3.1799011E-11	7.3305569E-07	4.0121257E-07	1.9682196E-12
1.78E-04	3.1799011E-11	5.7439533E-07	3.1443502E-07	1.9682196E-12
2.00E-04	3.1799011E-11	4.4775928E-07	2.4599747E-07	1.9682196E-12
2.24E-04	3.1799011E-11	3.4583291E-07	1.9262631E-07	1.9682196E-12
2.51E-04	3.1799011E-11	2.6357508E-07	1.5136576E-07	1.9682196E-12
2.82E-04	3.1799011E-11	1.9741811E-07	1.1967645E-07	1.9682196E-12
3.16E-04	3.1799011E-11	1.4472464E-07	9.5455410E-08	1.9682196E-12
3.55E-04	3.1799011E-11	1.0328583E-07	7.7629730E-08	1.9682196E-12
3.98E-04	3.1799011E-11	7.1737272E-08	6.4572747E-08	1.9682196E-12
4.47E-04	3.1799011E-11	4.8660095E-08	5.4463520E-08	1.9682196E-12
5.01E-04	3.1799011E-11	3.2347679E-08	4.6178416E-08	1.9682196E-12
5.62E-04	3.1799011E-11	2.1148204E-08	3.9020321E-08	1.9682196E-12
6.31E-04	3.1799011E-11	1.3645270E-08	3.2576373E-08	1.9682196E-12
7.08E-04	3.1799011E-11	8.7194122E-09	2.6638902E-08	1.9682196E-12
7.94E-04	3.1799011E-11	5.5374112E-09	2.1153061E-08	1.9682196E-12
8.91E-04	3.1799011E-11	3.5071873E-09	1.6170187E-08	1.9682196E-12
1.00E-03	3.1799011E-11	2.2231147E-09	1.1797321E-08	1.9682196E-12
1.12E-03	2.6265660E-11	1.3666541E-09	7.0744506E-09	1.9682196E-12

Size (m)	LD Flux	MD Flux	HD Flux	IN Flux
1.26E-03	2.1581584E-11	7.9753699E-10	3.1729036E-09	1.9682196E-12
1.41E-03	1.7642672E-11	4.5008492E-10	1.1459526E-09	1.9682196E-12
1.58E-03	1.4351497E-11	2.5023349E-10	3.5884989E-10	1.9682196E-12
1.78E-03	1.1618434E-11	1.3962387E-10	1.0490256E-10	1.9682196E-12
2.00E-03	9.3622739E-12	7.9651339E-11	3.0823169E-11	1.9682196E-12
2.24E-03	7.5104190E-12	4.7326197E-11	9.8011524E-12	1.9682196E-12
2.51E-03	5.9987648E-12	2.9836040E-11	3.6314194E-12	1.9682196E-12
2.82E-03	4.7713371E-12	2.0331420E-11	1.6879745E-12	1.9682196E-12
3.16E-03	3.7797645E-12	1.5255876E-11	1.0598302E-12	1.9682196E-12
3.55E-03	2.9899289E-12	1.2285352E-11	8.1110965E-13	1.9682196E-12
3.98E-03	2.3642201E-12	1.0183669E-11	6.4675736E-13	1.9682196E-12
4.47E-03	1.8647179E-12	8.6419915E-12	5.3332642E-13	1.9682196E-12
5.01E-03	1.4638744E-12	7.4669438E-12	4.5144632E-13	1.9682196E-12
5.62E-03	1.1413719E-12	6.5330809E-12	3.8936043E-13	1.9682196E-12
6.31E-03	8.8196331E-13	5.7565982E-12	3.3962650E-13	1.9682196E-12
7.08E-03	6.7397076E-13	5.0805783E-12	2.9739028E-13	1.9682196E-12
7.94E-03	5.0823674E-13	4.4666955E-12	2.5947695E-13	1.9682196E-12
8.91E-03	3.7739207E-13	3.8905601E-12	2.2391801E-13	1.9682196E-12
1.00E-02	2.7535215E-13	3.3390053E-12	1.8970066E-13	1.9682196E-12
1.12E-02	2.0116450E-13	2.8425846E-12	1.6106136E-13	1.9682196E-12
1.26E-02	1.4877800E-13	2.4229920E-12	1.3969207E-13	1.9682196E-12
1.41E-02	1.0983900E-13	2.0647514E-12	1.2258137E-13	1.9682196E-12
1.58E-02	7.9819844E-14	1.7562880E-12	1.0778640E-13	1.9682196E-12
1.78E-02	5.6299902E-14	1.4889181E-12	9.4059927E-14	1.9682196E-12
2.00E-02	3.8006058E-14	1.2561108E-12	8.0679089E-14	1.9682196E-12
2.24E-02	2.4213212E-14	1.0529362E-12	6.7367036E-14	1.9682196E-12
2.51E-02	1.4355304E-14	8.7564501E-13	5.4234851E-14	1.9682196E-12
2.82E-02	7.8097785E-15	7.2134159E-13	4.1693510E-14	1.9682196E-12
3.16E-02	3.8444781E-15	5.8772704E-13	3.0313210E-14	1.9682196E-12
3.55E-02	1.2076939E-15	4.7211297E-13	1.3061374E-14	1.9152759E-12
3.98E-02	1.8114492E-16	3.7349200E-13	2.2460942E-15	1.7761047E-12
4.47E-02	1.3978874E-17	2.9146768E-13	1.7008529E-16	1.5846414E-12
5.01E-02	5.9802840E-19	2.2474077E-13	6.2578151E-18	1.3732970E-12
5.62E-02	1.5282764E-20	1.7150007E-13	1.2342792E-19	1.1671180E-12
6.31E-02	2.5138498E-22	1.2973177E-13	1.4399794E-21	9.8203653E-13
7.08E-02	2.8678800E-24	9.7439852E-14	1.0963996E-23	8.2594080E-13
7.94E-02	2.4450836E-26	7.2785310E-14	6.0113040E-26	7.0101028E-13
8.91E-02	1.6786666E-28	5.4159710E-14	2.6186245E-28	6.0617753E-13
1.00E-01	0.0000000E+00	4.0210828E-14	0.0000000E+00	5.3916420E-13
1.12E-01	0.0000000E+00	3.0371977E-14	0.0000000E+00	4.8607578E-13
1.26E-01	0.0000000E+00	2.3543284E-14	0.0000000E+00	4.3600331E-13
1.41E-01	0.0000000E+00	1.8462503E-14	0.0000000E+00	3.9058190E-13
1.58E-01	0.0000000E+00	1.4438073E-14	0.0000000E+00	3.5075557E-13
1.78E-01	0.0000000E+00	1.1099123E-14	0.0000000E+00	3.1695734E-13
2.00E-01	0.0000000E+00	8.2678851E-15	0.0000000E+00	2.8929068E-13
2.24E-01	0.0000000E+00	5.8829093E-15	0.0000000E+00	2.6769428E-13
2.51E-01	0.0000000E+00	3.9413721E-15	0.0000000E+00	2.5208581E-13
2.82E-01	0.0000000E+00	2.4509017E-15	0.0000000E+00	2.4249120E-13
3.16E-01	0.0000000E+00	1.3944184E-15	0.0000000E+00	2.3917484E-13
3.55E-01	0.0000000E+00	5.0409598E-16	0.0000000E+00	2.3917484E-13

Size (m)	LD Flux	MD Flux	HD Flux	IN Flux
3.98E-01	0.0000000E+00	8.5519023E-17	0.0000000E+00	2.3917484E-13
4.47E-01	0.0000000E+00	7.3599627E-18	0.0000000E+00	2.3917484E-13
5.01E-01	0.0000000E+00	3.4736490E-19	0.0000000E+00	2.3917484E-13
5.62E-01	0.0000000E+00	9.7191374E-21	0.0000000E+00	2.3917484E-13
6.31E-01	0.0000000E+00	1.7427497E-22	0.0000000E+00	2.3917484E-13
7.08E-01	0.0000000E+00	2.1649200E-24	0.0000000E+00	2.3917484E-13
7.94E-01	0.0000000E+00	2.0141058E-26	0.0000000E+00	2.3917484E-13
8.91E-01	0.0000000E+00	1.5170165E-28	0.0000000E+00	2.3917484E-13
1.00E+00	0.0000000E+00	0.0000000E+00	0.0000000E+00	2.3917484E-13

Table A-2. The interpolated flux for element 6871. For this test case, a subset of interpolated fluxes is shown, covering sizes from 316 μ m to 3.16 cm for the LD family.

Bold text indicates the five reference points in this size range.

Size (m)	LD Flux
3.16E-04	2.3613899E-12
3.55E-04	2.3613899E-12
3.98E-04	2.3613899E-12
4.47E-04	2.3613899E-12
5.01E-04	2.3613899E-12
5.62E-04	2.3613899E-12
6.31E-04	2.3613899E-12
7.08E-04	2.3613899E-12
7.94E-04	2.3613899E-12
8.91E-04	2.3613899E-12
1.00E-03	2.3613899E-12
1.12E-03	2.1440467E-12
1.26E-03	1.6213458E-12
1.41E-03	1.0369424E-12
1.58E-03	5.6955270E-13
1.78E-03	2.7281999E-13
2.00E-03	1.1572953E-13
2.24E-03	4.4146937E-14
2.51E-03	1.5378292E-14
2.82E-03	4.9674037E-15
3.16E-03	1.5108709E-15
3.55E-03	3.2906679E-16
3.98E-03	4.0047613E-17
4.47E-03	2.8744847E-18
5.01E-03	1.2843669E-19
5.62E-03	3.7706730E-21
6.31E-03	7.6772242E-23
7.08E-03	1.1441951E-24
7.94E-03	1.3175326E-26
8.91E-03	1.2372089E-28
1.00E-02	0.0000000E+00
1.12E-02	0.0000000E+00
1.26E-02	0.0000000E+00
1.41E-02	0.0000000E+00
1.58E-02	0.0000000E+00
1.78E-02	0.0000000E+00

Size (m)	LD Flux
2.00E-02	0.0000000E+00
2.24E-02	0.0000000E+00
2.51E-02	0.0000000E+00
2.82E-02	0.0000000E+00
3.16E-02	0.0000000E+00

Table A-3. The interpolated flux for element 6481. For this test case, a subset of interpolated fluxes is shown, covering sizes from 10 μm to 316 μm for the HD family. Bold text indicates the four reference points in this size range.

Size (m)	HD Flux
1.00E-05	1.1659690E-05
1.12E-05	1.1321942E-05
1.26E-05	1.0376834E-05
1.41E-05	8.9904648E-06
1.58E-05	7.3745597E-06
1.78E-05	5.7357475E-06
2.00E-05	4.2365003E-06
2.24E-05	2.9761243E-06
2.51E-05	1.9915206E-06
2.82E-05	1.2713695E-06
3.16E-05	7.7548842E-07
3.55E-05	2.2706078E-07
3.98E-05	1.7609030E-08
4.47E-05	4.1695892E-10
5.01E-05	3.4749910E-12
5.62E-05	1.1750455E-14
6.31E-05	1.8583792E-17
7.08E-05	1.5846401E-20
7.94E-05	8.3981123E-24
8.91E-05	3.1887865E-27
1.00E-04	0.0000000E+00
1.12E-04	0.0000000E+00
1.26E-04	0.0000000E+00
1.41E-04	0.0000000E+00
1.58E-04	0.0000000E+00
1.78E-04	0.0000000E+00
2.00E-04	0.0000000E+00
2.24E-04	0.0000000E+00
2.51E-04	0.0000000E+00
2.82E-04	0.0000000E+00
3.16E-04	0.0000000E+00

Table A-4. The interpolated flux for element 970. For this test case, a subset of interpolated fluxes is shown, covering sizes from 10 μm to 100 μm for the HD family. Bold text indicates the three reference points in this size range.

Size (m)	HD Flux
1.00E-05	2.8502824E-06
1.12E-05	1.0218781E-08
1.26E-05	3.6636191E-11
1.41E-05	1.3134741E-13
1.58E-05	4.7090439E-16
1.78E-05	1.6882779E-18
2.00E-05	6.0527837E-21
2.24E-05	2.1700331E-23
2.51E-05	7.7799638E-26
2.82E-05	2.7892587E-28
3.16E-05	0.0000000E+00
3.55E-05	0.0000000E+00
3.98E-05	0.0000000E+00
4.47E-05	0.0000000E+00
5.01E-05	0.0000000E+00
5.62E-05	0.0000000E+00
6.31E-05	0.0000000E+00
7.08E-05	0.0000000E+00
7.94E-05	0.0000000E+00
8.91E-05	0.0000000E+00
1.00E-04	0.0000000E+00